ON DETERMINING CONTINUUM QUANTITIES OF NON-EQUILIBRIUM PROCESSES VIA MOLECULAR DYNAMICS SIMULATIONS

by

Yao Fu

B.S., Hefei University of Technology, 2006

M.S., Institute of Metal Research, Chinese Academy of Sciences, 2009

Submitted to the Graduate Faculty of

Swanson School of Engineering in partial fulfillment

of the requirements for the degree of

Doctor of Philosophy

University of Pittsburgh

2013

UNIVERSITY OF PITTSBURGH

SWANSON SCHOOL OF ENGINEERING

This dissertation was presented

by

Yao Fu

It was defended on

February 19, 2013

and approved by

Scott X. Mao, Ph.D., Professor, Department of Mechanical Engineering and Materials Science

Lisa M. Weiland, Ph.D., Associate Professor, Department of Mechanical Engineering and Materials Science

William S. Slaughter, Ph.D., Associate Professor, Department of Mechanical Engineering and Materials Science

Kenneth D. Jordan, Ph.D., Professor, Department of Chemistry

Dissertation Director: Albert C. To, Ph.D., Assistant Professor, Department of Mechanical Engineering and Materials Science

ON DETERMINING CONTINUUM QUANTITIES OF NON-EQUILIBRIUM PROCESSES VIA MOLECULAR DYNAMICS SIMULATIONS

Yao Fu, PhD

University of Pittsburgh, 2013

In this dissertation, a high-fidelity atomistic-to-continuum link for highly non-equilibrium processes has been established by making several modifications to Hardy's theory. Although Hardy's thermomechanical quantities were derived analytically to conserve mass, momentum and energy, they have not been rigorously tested and validated numerically in the past.

Hence the first task was to investigate the effectiveness of ensemble averaging in removing thermal fluctuations and compare with conventional time averaging for fcc crystals simulated using both equilibrium and non-equilibrium molecular dynamics (MD) simulations, where the non-equilibrium process was introduced by a shock impact. It has been found that the ensemble averaging has better convergence than time averaging due to the statistical independence of the thermomechanical quantities computed using ensemble averaging.

The second task was to test the validity of Hardy's theory by checking if it is able to conserve mass, momentum and energy numerically. A few highly non-equilibrium processes were simulated using MD, including Gaussian wave and shock impact propagation in 1D and 3D fcc crystals. Based on the test results, a new normalization rule has been proposed so that the computed thermomechanical quantities can conserve the fundamental properties more accurately. To a large extent, Hardy's theory has been found to be valid regardless of the width

of the localization function, the interatomic potential and crystal structure, and with and without ensemble averaging.

To further test the validity of Hardy's theory for more complex non-equilibrium processes, where plastic deformation is accomplished through dislocation glide and slip band emission, a crack propagation problem in iron crystal with a pre-created center crack is simulated using MD. The computed Hardy's thermomechanical quantities can generally conserve mass, momentum and energy. Exceptions have been found around the crack region, where the computed quantities cannot obey the balance of energy but still conserve mass and momentum.

The results from this dissertation will help 1) inspire confidence in employing Hardy's theory with the proposed modifications to analyze MD simulation results, especially for non-equilibrium thermomechanical processes and 2) pave the way for concurrent atomistic/continuum coupled simulations.

TABLE OF CONTENTS

LIST OF TABLES

LIST OF FIGURES

PREFACE

Working on my PhD degree has been a challenging, exciting, yet sometimes frustrating experience. I am grateful to have shared this wonderful journey with so many people, whom I am indebted to but will not be able to list in a single Acknowledgement section. Below I will simply mention those who have provided significant advice and help.

First of all, I am deeply thankful to my advisor, Dr. Albert C. To, who consistently guides me and encourages me through the doctoral program. He has so patiently given me advice, offered precious discussion time from his tight schedule and even helped me derive equations together with me to solve difficulties. He has provided me with many opportunities to attend conferences, talk to people in other areas and strengthen communication skills by exchanging ideas with other professors. His high academic standards and hard work have set an example and made a steady influence on me. All in all, I sincerely appreciate his guidance.

My second debt of gratitude goes to my committee, Dr. Kenneth Jordan, Dr. Scott Mao, Dr. Lisa Weiland and Dr. William Slaughter for their precious time and helpful suggestions. It has been a privilege to have them all as my committee, without whom I will not be able to complete my Ph.D.

Members of the computational nanomechanics group, Qingcheng Yang, Emre Biyikli, Pu Zhang, Mesut Kirca, Dr. Xueming Yang and Dr. Aditi Datta also deserve my sincerest thanks. I thank them for their support and encouragement not only as coworkers but also as friends. Their

work has inspired me in a lot of ways and their friendships help me through in my most difficult times. I am grateful to have worked together with them all.

I also want to thank my friends in the United States, China and other parts of the world for sharing happy and disappointing moments with me. Special thanks go to Yijen Wu, Manyu Li, Jia Zhong, Yu Wang, Mingjiang Zhong, Jie Song, Wenjun Kuang, Qingyun Lin, Jing Lv, Yujuan Zhao, Yi Xu and Haopeng Wang. My life becomes more meaningful because of them.

Finally, I want to thank my family in China, my father Guo Fu, mother Yuqin Wang and all my other family members. Their love is my driving force and my ultimate motivation to accomplish my degree. I am so much indebted to them and I appreciate their infinite support from the depth of my heart.

July, 2013

Yao Fu

1.0 INTRODUCTION

Non-equilibrium thermomechanical systems are systems that are not in thermomechanical equilibrium, because they are changing or can be triggered to change over time and are subjected to flux of matter and energy and to chemical reactions. Non-equilibrium thermomechanical processes such as shocked-induced molecular reactions in energetic materials and crack propagation problems are often of great interest since mass, momentum and energy transport, even chemical reactions, are involved. To enhance material performance by design, it is crucial to understand the underlying mechanism of the phenomena in non-equilibrium thermomechanical systems.

Molecular dynamics (MD) simulation [1-3], which provides a classical solution of equations of motions for interacting atoms, is a powerful way of studying time-dependent processes at the atomistic level [1-3]. On the other hand, continuum mechanics theory has also been successfully used to predict materials behavior at the macroscopic scale for decades. To bridge the atomistic mechanics and continuum mechanics, it is important to understand how macroscopic thermomechancial quantities such as stress, heat flux, and temperature can be expressed in terms of atomic position, velocity and potential. Virial theorem, Irving and Kirkwood's formulas and Hardy's formulas are among the efforts to derive continuum quantities from interacting atomic systems. Hardy's formulas enable us to compute local stress, heat flux and temperature conveniently from atomistic simulation results, which makes them more suitable

to investigate highly non-equilibrium systems simulated by MD. To achieve the expectation values of the computed thermomechanical quantities, time, spatial and ensemble averaging methods are often employed to remove the fluctuations caused by finite temperature.

The main objective of this dissertation is to establish a high-fidelity link between atomistic to continuum scales for highly non-equilibrium systems by applying an ensemble averaging method on Hardy's thermomechanical quantities and to test the validity of Hardy's theory by checking if the computed quantities obey continuum conservation equations.

1.1.1 Shock impact on metals and energetic materials

Shock impact on materials can trigger a variety of interesting non-equilibrium phenomena such as plastic deformation [4-9], phase transformation [10-13], and chemical reactions [14-18] depending on the shock loading conditions as well as the material states. MD simulation is capable of simulating real-time evolution at the atomistic scale, which naturally meets the requirement to capture the rapidity and locality of shockwave phenomena. The first non-equilibrium molecular dynamics (NEMD) simulation of a shockwave-like phenomenon was carried out by George Vineyard and his group at Brookhaven [19]. Since then NEMD has been widely used to study shocked induced plastic flow and phase transformation. A noteworthy example demonstrated by B. Holian and co-workers using NEMD simulations was shock waves in three-dimensional (3D) face-centered cubic (fcc) crystals containing 10-million atoms with cross-sectional dimensions of 100 by 100 unit cells [6]. They discovered that the system slips along all of the available slip planes and the shock waves propagating through the system can instantly create a large number of stacking faults.

Shock-initiated molecular reactions in energetic materials is another class of widely investigated phenomena using NEMD. Many useful energetic materials (PETN, TATB, TNT, RDX, HMX) are molecular crystals which are bonded together through covalent bonding within individual molecules and non-covalent bonding between adjacent molecules [20-23]. Stretching the covalent bonds gives rise to excitations termed intramolecular vibrations or simply vibrations, while stretching the intermolecular bonds gives rise to collective delocalized excitations termed phonons. The transfer of substantial amounts of mechanical energy from the shock front to the internal vibrational states of the molecules [24-29] is termed 'multiphonon up-pumping'. Recent developments in reactive force-field molecular dynamics (ReaxFF-MD) combined with advances in parallel computing have paved the way to accurately simulate reaction pathways along with the structure of shock fronts. Besides, MD simulation can also be used to characterize and follow details of important time-dependent processes occurring within the localized region of microscopic defects that might result in the generation of hot spots, which have been believed to be closely related to the initiation of the energetic materials and its sensitivity to impact [17, 30-33].

1.1.2 Crack propagation in iron-based alloys

Facture mechanism in iron-based alloys especially ferritic steels, has recently sparked some interest because of the broad application of iron-based alloys in various areas. A common problem for materials with a body centered cubic (bcc) lattice structure is that they are prone to low temperature brittleness. For ferritic-martensitic steels that are commonly used in modern nuclear reactors, severe radiation can even shift the brittleness from below room temperatures to higher temperatures. Understanding the processes occurring at the tips of the brittle or quasi-

brittle cracks during the crack nucleation and propagation can help develop fracture resistant steels and determine their safe application in particular environments. As the crack propagates, bonds break between atoms, and this process is often accompanied with generation of slips bands and twinning as well as the emission of edge dislocations. The fundamental mechanism of material fracture behaviors thus needs to be understood with the aid of atomistic scale simulations, such as MD simulations. The emergence of large scale parallel computers has allowed MD simulations to model crack propagation in systems that can size up to 1 billion atoms and have a time scale up to the nanosecond. Many computer simulations at the atomistic scale have been performed to clarify the fracture mechanism under monotonic loadings [34-40]. Cleri et al. studied crack-tip shielding by dislocation emitted from the crack tip at an atomistic level using MD simulation [41]. Emission of dislocation loops from the crack tip and dislocation intersections has been discovered using large scale MD simulations in a 3D model. In addition, MD simulations have been used to study 3D kinetics of micro-crack propagation in ferritic-iron and the accompanying lattice transformations at the crack tips. It has also been discovered that crack initiation on {001} planes in iron is preceded with the emission of compact slip bands from the pre-crack tips [35]. The crack propagation behaviors on other slip planes {110} and {211} have been reported by Gao et al.

1.2 LINK BETWEEN ATOMISTIC AND CONTINUUM SCALES

While MD simulations have been successfully used to provide information at the atomic level, the macroscopic behavior of materials has been modeled in terms of deterministic continuum mechanics. Continuum theory of material deformation at the macroscopic scale involves quantities such as stress, temperature and heat flux. Molecular dynamics theory, on the other

hand, involves quantities such as atomic velocity and position. Since the descriptions in these two frameworks are quite different, it is necessary to understand the way in which the relatively complicated microscopic many-body dynamics give rise to the relatively simple macroscopic behavior described by fewer variables in the continuum description. Bridging atomistic to continuum scales is also motivated by the development of multiscale simulations, which requires communication between atomic and continuum properties concurrently [42-53]. A key challenge of linking the atomistic and continuum descriptions lies in determining the continuum thermomechanical quantities from MD simulation with high spatial and time resolution, which is especially useful for the analysis of highly non-equilibrium processes happening at nano/atomistic scale. Thus far, much effort has been devoted to developing different definitions of thermomechanical quantities from the atomic quantities in MD simulations.

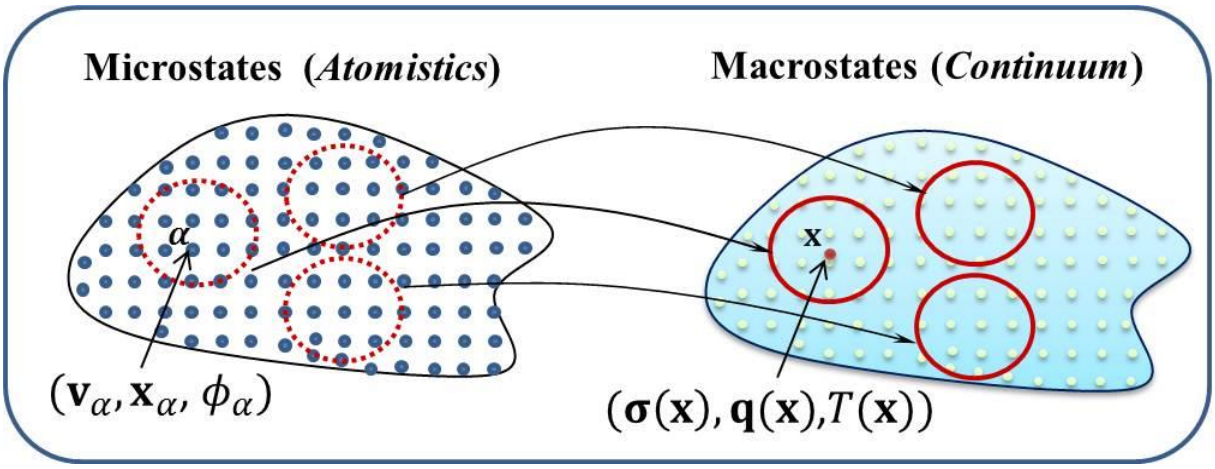

Figure 1.1 Schematic illustration of bridging atomistic and continuum scale quantities ($\mathbf{v}_\alpha$, $\mathbf{x}_\alpha$, and ϕ_α are the velocity, position and potential energy of atom α. And $\boldsymbol{\sigma}(\mathbf{x})$, $\mathbf{q}(\mathbf{x})$ and $T(\mathbf{x})$ are the stress, heat flux and temperature at the spatial point, $\mathbf{x}$, in the continua).

1.2.1 Virial theorem

The earliest effort is the development of the virial theorem (VT) by Clausius and Maxwell [54-56] to determine the stress field applied to the surface of a fixed volume containing *N* interacting particles. The virial stress developed based on the VT is shown below:

$$\boldsymbol{\sigma}^{\mathrm{V}} = -\frac{1}{\boldsymbol{\Omega}}\left\{\frac{1}{2}\sum_{\alpha=1}^{N}\sum_{\beta\neq\alpha}^{N}\mathbf{x}_{\alpha\beta}\otimes\mathbf{F}_{\alpha\beta} + \sum_{\alpha=1}^{N} m_{\alpha}\mathbf{v}_{\alpha}\otimes\mathbf{v}_{\alpha}\right\} \tag{1.1}$$

where β takes values 1 to *N* neighbors of atoms α, $\mathbf{x}_{\alpha\beta} = \mathbf{x}_{\alpha} - \mathbf{x}_{\beta}$ and $\mathbf{x}_{\alpha}$ is the position of atom α, m_{α} and $\mathbf{v}_{\alpha}$ represent the mass and velocity of atom α, $\mathbf{F}_{\alpha\beta}$ is the force between atoms α and β, and Ω is the total volume of the *N* particle system. The above definition of virial stress demonstrates fluctuations about the equilibrium average because of thermal fluctuations of the atomic positions, velocities, and forces. Hence, the virial stress calculated in MD simulations is typically averaged over time in order to obtain a good description of the system equilibrium average. This so-called 'time averaging' has been widely used in numerical studies of many material science phenomena [57-61]. Although the expression for VT is developed as a macroscopic-level average stress, it is often inappropriately used for calculating atomic-level local stress. As a result, erroneous estimates of stress have been found [62-64]. There have been several efforts to correct the misuse of the VT as local stress through new definitions for stress and/or heat flux that satisfy the conservation of mass/momentum/energy for a dynamic continuum [62, 65-70] or by using a stress tensor [63, 71-74].

1.2.2 Irving and Kirkwood's theory

Irving and Kirkwood [75] also presented formulas in their classical paper on the equations of hydrodynamics, thus making a pioneering contribution to correct the misuse of the VT. They proposed formulas for mass, momentum and energy densities that are defined for a spatial point at a time instant based on the statistical distribution of particles nearer to the point chosen and used the conservation equations to deduce formulas for stress and heat flux. The resulting equations for stress and heat flux require integration over phase space of quantities weighted by the Dirac delta function and a probability distribution function of phase space. One of these quantities is an infinite-series expansion of differential operators, which makes it difficult to implement within a standard MD simulation.

1.2.3 Hardy's theory

Among the attempts to improve upon the approach originally conceived by Irving and Kirkwood, Hardy and his colleagues bypassed some of the mathematical complexities of Irving and Kirkwood's approach by using a finite-valued and finite-ranged localization function in place of the Dirac delta function [76, 77]. The resulting expression for stress/heat flux contains terms that theoretically remain constant regardless of different volume sizes, namely, the characteristic size of the volume that contains atoms contributing to properties at the spatial point chosen. Hardy and his colleagues also derived an expression for temperature through the equipartition theorem and the kinetic energy associated with the atomic velocities relative to the velocity of the continuum at a spatial point [78].

Hardy's stress expression has been tested numerically by Zimmerman and coworkers for systems subjected to deformation, finite temperature or both using MD simulations. And it has been found that increasing characteristic volume of the localization function can lead to quicker convergence to the expected values. The behavior of Hardy's stress expression near a free surface was also examined and found to be consistent with the mechanical definition of stress. Webb III et al. performed the evaluation of stress using Hardy's formulas around the core of an edge dislocation in cylindrical aluminum after energy minimization [79]. Computed heat flux in a static non-equilibrium ensemble has been evaluated against the theoretical predictions from Fourier's Law. In both cases, the results obtained from Hardy's expressions are in good agreement with theoretical predictions.

1.3 TIME, SPATIAL AND ENSEMBLE AVERAGING

Previous investigations have demonstrated that the stress/heat flux fluctuations at finite temperature need to be eliminated through time averaging to reach the expected values beside spatial averaging inherent in the Hardy's formulas [80]. Fluctuations of properties around expected values introduced by finite temperature are commonly removed through a spatial and temporal averaging method [81]. For simulations involving inhomogeneous deformation or rapidly time varying thermomechanical fields, conventional approaches of choosing large volume/time window size to reduce fluctuations can over-smooth interesting thermomechanical properties. On the other hand, sharp features can be masked by the large fluctuations if a small volume/time window size is chosen. Either large or small window size adopted can cause deteriorated accuracy of the computed thermomechanical fields for highly non-equilibrium

processes. It is most desirable to have both high spatial/temporal resolution and high accuracy in the computed thermomechanical quantities.

For this purpose, a ‘many-realization approach’ is proposed to evaluate the ensemble average of continuum stress/heat flux/temperature for the first time in the present study. Note the many-realization approach is just the Monte Carlo method employed in engineering, but it is different from the conventional atomistic scale Monte Carlo [82, 83]. So that is why the name ‘many-realization approach’ is used to avoid confusion. Ensemble averaging has a unique advantage over spatial averaging and time averaging because it is not a function of time and space. Therefore, the quality of ensemble averaged quantities does not deteriorate when the thermomechanical process involved becomes farther away from the equilibrium. In addition, the computed thermomechanical quantities from different realizations employed in evaluating the ensemble averaged values are not correlated, in contrast to the time and spatial averaged ones. Another consideration of applying ensemble averaging to Hardy’s formulas is that the ensemble average of Hardy’s expressions for mass density, momentum density, energy density as well as the kinetic part of stress and heat flux, are equivalent to the corresponding formulas of Irving and Kirkwood [78]. The main difference between Hardy’s formulas from those developed by Irving and Kirkwood is that Hardy replaced the Dirac delta function with the general localization function. If applying ensemble averaging on Hardy’s formulas can lead to accurate thermomechanical quantities with high resolution, the validity of the continuum conservation equations should also be established.

1.4 RESEARCH OBJECTIVES

In this dissertation, the following three objectives are to be achieved: (1) the convergence of the ensemble average and time average of the Hardy's expressions are compared for some equilibrium systems at finite temperatures as well as a non-equilibrium process due to shock impact. Different situations that time and ensemble averaging can be applied to will be discussed. (2) Continuum conservation equations including balance laws of mass, momentum and energy will be validated numerically through a series of non-equilibrium processes using MD simulations, where atomistic-to-continuum thermomechanical fields are constructed using Hardy's formulas and ensemble averaging at finite temperatures. (3) The ensemble average of Hardy's quantities is also applied to a crack propagation problem in iron and to construct the stress field around the defective crack tip region as crack propagates under tensile and shearing loading. In addition, the validity of continuum conservation equations using Hardy's formulas will be tested around the crack tip where slip bands and other defects exist.

The accomplishment of the three objectives will contribute to the high-fidelity link between atomistic and continuum regimes for highly non-equilibrium systems.

2.0 THEORETICAL BACKGROUND

In this Chapter, molecular dynamics (MD) technique is briefly discussed and then the concepts of statistical ensemble and ensemble averaging are explained. The Liouville's theorem is given which describes the time dependence of density function of the ensemble, and from which the continuum conservation equations can be represented in terms of atomistic quantities. The derivation of stress and heat flux expressions by Irving and Kirkwood is demonstrated, as well as the derivation of Hardy's expressions for stress, heat flux and temperature. Finally, a many-realization approach is proposed, which implements ensemble averaging of Hardy's formulas without explicit knowledge of the density distribution function.

2.1 MOLECULAR DYNAMICS SIMULATION

Classical molecular dynamics (MD) simulations are widely used to study atomic and molecular scale phenomena and to compute the equilibrium and transport properties of atomic and molecular systems [1-3, 82]. Here, 'classical' means that the nuclear motion of the constituent particles obeys the laws of classical mechanics and that Newton's classical equations of motion (Eq. 2.1) are used to compute the trajectories of the atoms. The incomplete discussion in this section only provides necessary information regarding the calculation of thermomechanical

quantities from MD simulation results. The equation of motion for atom α in a system of interacting atoms is given as:

$$m_\alpha \boldsymbol{a}_\alpha = -\nabla_{\mathbf{x}_\alpha} U + \boldsymbol{f}^{ext} \tag{2.1}$$

where U is interatomic potential energy, m_α and $\mathbf{x}_\alpha$ are the mass and the instantaneous position of atom α, $\boldsymbol{a}_\alpha$ is the acceleration of atom α and $\boldsymbol{f}^{ext}$ is the external force.

To start a MD simulation, initial positions and velocities need to be assigned to all atoms in the system. The atom positions should be chosen corresponding to the material structure under consideration. After each atom is placed in its appropriate position, their velocity components can be assigned with values drawn from a Maxwell-Boltzmann distribution. All velocities can be shifted later on so that the total momentum of the atomic system is zero. The most time-consuming part of MD simulations is to calculate the force acting on every atom.

The force on the αth atom $\boldsymbol{f}_\alpha$ is obtained from a spatial derivative of the potential energy U: $\boldsymbol{f}_\alpha = -\nabla_{\mathbf{x}_\alpha} U$. Pair potentials (such as Lennard-Jones and Morse potentials) are probably the most prevalent types of potential energy and involve only the position of two atoms when computing a discrete contribution to the total energy. Pair potentials have been used to model the physics of inert gas solids. Many three-body potentials consider the bond angle formed by two bonds, where a bond exists between the first and second atoms as well as the first and third atoms. Therefore, three atoms are considered when computing a discrete contribution to the total energy. Such potentials have been used to model covalent semiconductor material such as silicon (Si). Many-body potentials also exist, where the energy of a given atom is a function of the total bonding environment surrounding it. The embedded atom method (EAM) potential is a multibody potential where U of a system of N atoms is given by [84-87]:

$$U = \sum_{\alpha}^{N} F_{\alpha}(\rho_{h,\alpha}) + \frac{1}{2} \sum_{\substack{\alpha,\beta \\ \alpha \neq \beta}} V(x_{\alpha\beta}) \tag{2.2}$$

where $F_{\alpha}(\rho_{h,\alpha})$ is the embedding energy of atom α to the background electron density $\rho_{h,\alpha}$. The electron density at the site of atom α is approximated by the superposition of atomic densities, $\rho_{h,\alpha} = \sum_{\beta \neq \alpha} \rho_{\beta}^{a}(x_{\alpha\beta})$, where $\rho_{\beta}^{a}(x)$ is the electron density contributed by atom β at a distance x. And $V(x_{\alpha\beta})$ is the core-core pair repulsion between the atoms α and β separated by the distance $x_{\alpha\beta}$. The dependence of $\rho_{h,\alpha}$ upon a summation over the surrounding atoms in the system represents the many-body nature of EAM.

After all forces between the atoms are calculated, Newton's equations of motion can be integrated using the so-called Verlet algorithm, which is not only one of the simplest but also the most commonly used [88]. The standard implementation scheme of this algorithm is:

1. Calculate $\mathbf{v}_{\boldsymbol{\alpha}}\left(t + \frac{1}{2}\Delta t\right) = \mathbf{v}_{\boldsymbol{\alpha}}(t) + \frac{1}{2}\boldsymbol{a}_{\boldsymbol{\alpha}}\Delta t$.
2. Calculate $\mathbf{x}_{\boldsymbol{\alpha}}(t + \Delta t) = \mathbf{x}_{\boldsymbol{\alpha}}(t) + \mathbf{v}_{\boldsymbol{\alpha}}\left(t + \frac{1}{2}\Delta t\right)\Delta t$.
3. Derive $\boldsymbol{a}_{\boldsymbol{\alpha}}\left(t + \frac{1}{2}\Delta t\right)$ from the interaction potential using $\mathbf{x}_{\boldsymbol{\alpha}}(t + \Delta t)$.
4. $\mathbf{v}_{\boldsymbol{\alpha}}(t + \Delta t) = \mathbf{v}_{\boldsymbol{\alpha}}\left(t + \frac{1}{2}\Delta t\right) + \frac{1}{2}\boldsymbol{a}_{\boldsymbol{\alpha}}(t + \Delta t)\Delta t$.

$\mathbf{v}_{\alpha}$ and $\mathbf{x}_{\alpha}$ are the instantaneous velocity and position of atom α and $\boldsymbol{a}_{\alpha}$ is the acceleration of atom α computed from its mass m_{α} and force $\boldsymbol{f}_{\alpha}$. The duration over which atomic displacements are computed (i.e. the time step Δt) is typically around 1 fs and it is small enough to resolve atomic oscillations at finite temperature. With successive iterations of force computation and integration process the time/space trajectory for all atoms in the system can be established.

From the atomic positions, velocities and forces at every time step, macroscopic scale thermodynamics quantities can be calculated through an appropriate atomistic-to-continuum

relationship. For example, the instantaneous stress of the atomic system can be computed according to the virial stress definition given in Eq. 1.1. Note that finite temperature equilibrium simulations demonstrate fluctuations in systems properties about the equilibrium average. Therefore, the computed stress needs to be averaged over some window of simulation time to obtain the expectation value.

2.2 STATISTICAL ENSEMBLE

An ensemble is a collection of all the possible microscopic states that a system could be in, consistent with its observed macroscopic properties. A microstate of a system of atoms is a complete specification of all positions and momenta of the atoms. For example, a state of a system consisting of *N* particles can be specified by the 3*N* canonical coordinates $x_1, \dots, x_{3N}$ and their conjugate momenta $p_1, \dots, p_{3N}$. The 6N dimensional space spanned by $\{p_i, x_i\}$ is called the Γ space, or phase space, of the system. A point in Γ space represents a state of the entire *N*-particle system, and is referred to as the representative point. In contrast, for a macroscopic state, only very few features such as temperature, density, and total energy are specified. Thus, an ensemble could be a collection of all the ways a set of atoms could be arranged for a system as long as the extensive quantities defined for the macroscopic state are satisfied. Using the example of a gas system, it is apparent that a very large (in fact, infinite) number of microscopic states of the gas can correspond to a given macroscopic condition of the gas. For example, the velocities of atoms for two different microscopic states are different but the gas temperatures are the same. Through macroscopic measurements we would not be able to distinguish between two gases existing in different microstates (thus corresponding to two distinct representative points in

Γ space) but satisfying the same macroscopic conditions (Fig. 2.1). Therefore when we speak of a gas system under certain macroscopic conditions, we are in fact referring not to a single state, but to an infinite number of states. That is to say, we refer not to a single system, but to a collection of systems, identical in composition and macroscopic condition but existing in different microscopic states. According to Gibbs, such a collection of systems is called an ensemble, which is geometrically represented by a distribution of representative points in space, usually a continuous distribution. It may be conveniently described by a density function $f(p, x, t)$, where (p, x) is an abbreviation for $(p_1, \dots, p_{3N}; x_1, \dots, x_{3N})$, so that $f(p, x, t) d^{3N}p \, d^{3N}x$ is the number of representative points contained in the infinitesimal volume element $d^{3N}p \, d^{3N}x$ of Γ space centered about the point (p, x) at time *t*. An ensemble is completely specified by $f(p, x, t)$. It is to be emphasized that members of an ensemble are mental copies of a system and do not interact with one another.

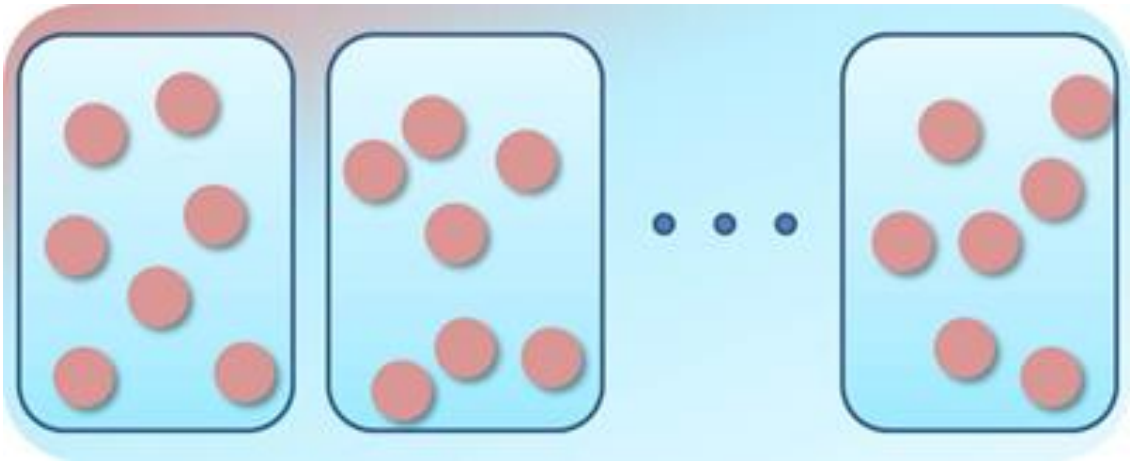

Figure 2.1 Schematic illustration of 'ensemble' concept using a gas with constant volume, pressure and number of particles

2.3 LIOUVILLE'S THEOREM

The time dependence of the density function $f(p,x,t)$ is described by Liouville's theorem [89]:

$$\frac{\partial f}{\partial t} = \sum_{\alpha=1}^{N} \left[-\frac{\mathbf{p}_\alpha}{m_\alpha} \cdot \nabla_{\mathbf{x}_\alpha} f + \nabla_{\mathbf{x}_\alpha} U \cdot \nabla_{\mathbf{p}_\alpha} f \right] \tag{2.3}$$

where U is the potential energy of the entire system, m_α is the mass of atom α. Vectors and tensors are represented in bold font. Any dynamical variable $O(p,x)$, which is generally a function of the coordinates and conjugate momenta, has an expectation value given at time t by

$$\langle O; f \rangle = \frac{\int d^{3N}p \, d^{3N}x \, O(p,x) f(p,x,t)}{\int d^{3N}p \, d^{3N}x \, f(p,x,t)} \tag{2.4}$$

$\langle O; f \rangle$ is used to denote the expectation value of O for a distribution function f, which is the inner product of O and f taken over phase space. If O does not depend on time explicitly, the rate of change of the expectation value of O is given by

$$\frac{\partial}{\partial t}\langle O; f \rangle = \langle O; \frac{\partial f}{\partial t} \rangle = \sum_{\alpha=1}^{N} \left[\langle O; -\frac{\mathbf{p}_\alpha}{m_\alpha} \cdot \nabla_{\mathbf{x}_\alpha} f \rangle + \langle O; \nabla_{\mathbf{x}_\alpha} U \cdot \nabla_{\mathbf{p}_\alpha} f \rangle \right] \tag{2.5}$$

Using Green's theorem applied in the space of $\mathbf{x}_\alpha$ and in the momentum space of $\mathbf{p}_\alpha$ yields

$$\langle O; -\frac{\mathbf{p}_\alpha}{m_\alpha} \cdot \nabla_{\mathbf{x}_\alpha} f \rangle = \langle \frac{\mathbf{p}_\alpha}{m_\alpha} \cdot \nabla_{\mathbf{x}_\alpha} O; f \rangle \tag{2.6a}$$

$$\langle O; \nabla_{\mathbf{x}_\alpha} U \cdot \nabla_{\mathbf{p}_\alpha} f \rangle = -\langle \nabla_{\mathbf{x}_\alpha} U \cdot \nabla_{\mathbf{p}_\alpha} O; f \rangle \tag{2.6b}$$

Therefore, Eq. 2.5 becomes

$$\frac{\partial}{\partial t}\langle O; f\rangle = \sum_{\alpha=1}^{N} \langle \frac{\mathbf{p}_\alpha}{m_\alpha} \cdot \nabla_{\mathbf{x}_\alpha} O - \nabla_{\mathbf{x}_\alpha} U \cdot \nabla_{\mathbf{p}_\alpha} O; f\rangle \tag{2.7}$$

Thus giving the rate of change of the expectation value of O as the expection value of the dynamical variable $\sum_{\alpha=1}^{N}\left[\frac{\mathbf{p}_\alpha}{m_\alpha} \cdot \nabla_{\mathbf{x}_\alpha} O - \nabla_{\mathbf{x}_\alpha} U \cdot \nabla_{\mathbf{p}_\alpha} O\right]$.

2.4 IRVING AND KIRKWOOD'S THEORY

In the seminal work by Irving and Kirkwood, Eq. 2.7 is used to derive stress tensor and heat flux vector expressions in terms of atomistic variables. In that work, the mass density $\rho(\mathbf{x}, t)$, momentum density $\mathbf{p}(\mathbf{x}, t)$ and energy density $e^0(\mathbf{x}, t)$ are given in terms of atomic positions and momenta through the delta function δ and density distribution function f:

$$\rho(\mathbf{x}, t) = \textstyle\sum_{\alpha=1}^{N} m_\alpha \langle \delta(\mathbf{x}_\alpha - \mathbf{x}); f\rangle \tag{2.8a}$$

$$\mathbf{p}(\mathbf{x}, t) = \rho(\mathbf{x}, t)\mathbf{v}(\mathbf{x}, t) = \sum_{\alpha=1}^{N} \langle \mathbf{p}_\alpha \delta(\mathbf{x}_\alpha - \mathbf{x}); f\rangle \tag{2.8b}$$

$$e^0(\mathbf{x}, t) = \sum_{\alpha=1}^{N} \langle (\frac{p_\alpha^2}{2m_\alpha} + \varphi_\alpha)\delta(\mathbf{x}_\alpha - \mathbf{x}); f\rangle + \frac{1}{2}\sum_{\alpha}\sum_{\beta\neq\alpha} \langle V_{\beta\alpha}\delta(\mathbf{x}_\alpha - \mathbf{x}); f\rangle \tag{2.8c}$$

where $\varphi_\alpha(\mathbf{x}_\alpha)$ is the potential energy of the αth atom in an external field of force, and $V_{\beta\alpha}$ is the mutual potential between the βth and αth atoms. The material velocity field $\mathbf{v}(\mathbf{x}, t)$ is defined such that $\mathbf{p} = \rho\mathbf{v}$.

The continuum conservation equations from the phenomenological point of view are given by:

$$\frac{\partial \rho}{\partial t} = -\nabla_{\mathbf{x}} \cdot (\rho \mathbf{v}), \tag{2.9a}$$

$$\frac{\partial \mathbf{p}}{\partial t} = \nabla_{\mathbf{x}} \cdot (\boldsymbol{\sigma} - \rho \mathbf{v} \otimes \mathbf{v}) + \rho \mathbf{b}, \tag{2.9b}$$

$$\frac{\partial e^0}{\partial t} = \nabla_{\mathbf{x}} \cdot (\boldsymbol{\sigma} \cdot \mathbf{v} - e^0 \mathbf{v} - \mathbf{q}) + \rho \mathbf{b} \cdot \mathbf{v} + \rho s, \tag{2.9c}$$

$\mathbf{b}(\mathbf{x}, t)$ is the body force density, and $s(\mathbf{x}, t)$ is the energy source per unit mass. Definitions for stress tensor $\boldsymbol{\sigma}$ and heat flux vector $\mathbf{q}$ are derived by taking the derivative of mass, momentum and energy density given by Eq. 2.8 with respect to time, applying the Liouvilles's theorem (Eq. 2.7), and comparing with the right hand side (RHS) of Eq. 2.9. Details of the derivation can be found in [75]. The expressions (Eq. 2.10) have been claimed to be not only the most apparent choice of satisfying conservation equations both phenomenologically and at the atomistic scale, but also the only choice that is physically reasonable.

$$\begin{aligned}\boldsymbol{\sigma}(\mathbf{x}, t) = &- \sum_{\alpha=1}^{N} m \left\langle \left(\frac{\mathbf{p}_\alpha}{m} - \mathbf{v}\right)\left(\frac{\mathbf{p}_\alpha}{m} - \mathbf{v}\right) \delta(\mathbf{x}_\alpha - \mathbf{x}); f \right\rangle \\ &+ \frac{1}{2} \int \frac{\mathbf{X}\mathbf{X}}{X} V'(X) \left\{1 - \frac{1}{2}\mathbf{X} \cdot \nabla_{\mathbf{x}} + \cdots \frac{1}{n!}(-\mathbf{X} \cdot \nabla_{\mathbf{x}})^{n-1} + \cdots \right\} \rho^{(2)}(\mathbf{x}, \mathbf{x} \\ &+ \mathbf{X}, t) d\mathbf{X},\end{aligned} \tag{2.10a}$$

$$\begin{aligned}\mathbf{q}(\mathbf{x}, t) = &\sum_{\alpha=1}^{N} \left\langle \frac{m}{2} \left|\frac{\mathbf{p}_\alpha}{m} - \mathbf{v}\right|^2 \left(\frac{\mathbf{p}_\alpha}{m} - \mathbf{v}\right) \delta(\mathbf{x}_\alpha - \mathbf{x}); f \right\rangle - \frac{1}{2}\mathbf{v}(\mathbf{x}, t) \\ &\cdot \int \left[V(X)\mathbf{I} - \frac{\mathbf{X}\mathbf{X}}{X} V'(X) \left\{1 - \frac{1}{2}\mathbf{X} \cdot \nabla_{\mathbf{x}} + \cdots \frac{1}{n!}(-\mathbf{X} \cdot \nabla_{\mathbf{x}})^{n-1} + \cdots \right\}\right] \rho^{(2)}(\mathbf{x}, \mathbf{x} \\ &+ \mathbf{X}, t) d\mathbf{X} \\ &+ \frac{1}{2} \int \Big[V(X)\mathbf{I} \\ &- \frac{\mathbf{X}\mathbf{X}}{X} V'(X) \left\{1 - \frac{1}{2}\mathbf{X} \cdot \nabla_{\mathbf{x}} + \cdots \frac{1}{n!}(-\mathbf{X} \cdot \nabla_{\mathbf{x}})^{n-1} + \cdots \right\}\Big] \mathbf{j}_1{}^{(2)}(\mathbf{x}, \mathbf{x} + \mathbf{X}, t) d\mathbf{X}\end{aligned} \tag{2.10b}$$

where pair density $\rho^{(2)}(\mathbf{x}, \mathbf{x}', t) = \sum_\alpha \sum_{\beta \neq \alpha} \langle \delta(\mathbf{x}_\alpha - \mathbf{x}) \delta(\mathbf{x}_\beta - \mathbf{x}'); f \rangle$, and particle current density in pair space is given by the six-component vector $\mathbf{j}^{(2)}(\mathbf{x}, \mathbf{x}', t) = \sum_\alpha \sum_{\beta \neq \alpha} \langle (\frac{\mathbf{p}_\alpha}{m_\alpha} \oplus \frac{\mathbf{p}_\beta}{m_\beta}) \times \delta(\mathbf{x}_\alpha - \mathbf{x}) \delta(\mathbf{x}_\beta - \mathbf{x}'); f \rangle$.

The resulting formulas for stress and heat flux (Eq 2.9) contain terms that require integration over phase space quantities weighted by the Dirac delta function δ and a density

distribution function f. One of these quantities is an infinite-series expansion of differential operators. Therefore, the expressions developed by Irving and Kirkwood are very hard to implement for MD simulation result.

2.5 HARDY'S EXPRESSIONS FOR STRESS, HEAT FLUX AND TEMPERATURE

Hardy bypasses the numerical difficulties in Irving and Kirkwood's formulism by defining the mass, momentum and energy density using localization function ψ instead of Dirac delta function δ [76]:

$$\rho(\mathbf{x},t)=\sum_{\alpha=1}^{N} m_\alpha \psi(\mathbf{x}_\alpha-\mathbf{x}), \tag{2.11a}$$

$$\mathbf{p}(\mathbf{x},t)=\sum_{\alpha=1}^{N} m_\alpha \mathbf{v}_\alpha \psi(\mathbf{x}_\alpha-\mathbf{x}), \tag{2.11b}$$

$$e^0(\mathbf{x},t)=\sum_{\alpha=1}^{N}\left[\frac{1}{2}m_\alpha v_\alpha^2+\phi_\alpha\right]\psi(\mathbf{x}_\alpha-\mathbf{x}), \tag{2.11c}$$

Here ϕ_α represent the potential energy of atom α. The localization function ψ spreads out the properties of the atoms $\alpha=(1,2,\dots,N)$, and allows each atom to contribute to a continuum property at the position **x** at time *t* as shown in Fig 2.2. The function ψ has units of inverse volume and $\psi \neq 0$ only in some characteristic volume surrounding the spatial point **x**. Hardy has established a few rules with regard to the behavior of ψ:

1. $\psi(\mathbf{x}_\alpha-\mathbf{x})$ has its maximum at $\mathbf{x}_\alpha=\mathbf{x}$.
2. $\psi(\mathbf{x}_\alpha-\mathbf{x})\to 0$ as $|\mathbf{x}_\alpha-\mathbf{x}|\to\infty$.
3. $\psi(\mathbf{x}_\alpha-\mathbf{x})$ is smooth and non-negative.
4. $\int \psi(\mathbf{x}_\alpha-\mathbf{x})dV_\mathbf{x}=1$. $dV_\mathbf{x}$ is a volume element in the continuum space.

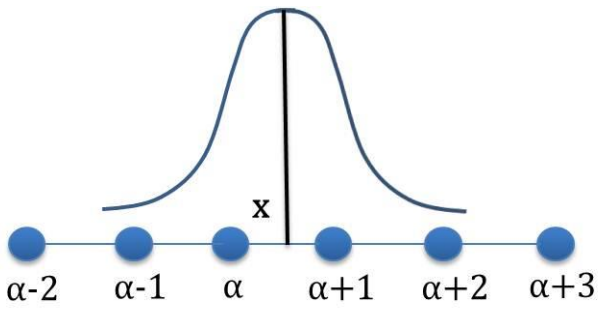

Figure 2.2 Schematic illustration of the localization function, linking the atomistic and continuum scales by assigning different weights to the atoms that contribute to the quantities computed at spatial point **x** in the continua

A bond function $B^{\alpha\beta}(\mathbf{x})$ between atoms α and β is defined by the expression: $B^{\alpha\beta}(\mathbf{x}) \equiv \int_0^1 \psi(\lambda\,\mathbf{x}_{\alpha\beta} + \mathbf{x}_\beta - \mathbf{x})d\lambda$, where $\mathbf{x}_{\alpha\beta} = \mathbf{x}_\alpha - \mathbf{x}_\beta$. $B^{\alpha\beta}$ represents a weighted fraction of the bond length segment between atoms α and β that lies within the characteristic volume. In order to derive an expression for a symmetric stress tensor, Hardy has made four key assumptions about the forms of the energies and forces for the atoms in the system:

(i) The total energy of the system Φ can be considered to be the summation of individual potential energies of each atom within the system, $\Phi = \sum_{\alpha=1}^{N} \phi_\alpha$.

(ii) The force on any atom can be expressed by the summation $\mathbf{F}_\alpha \equiv -\partial\Phi/\partial\mathbf{x}_\alpha = \sum_{\beta\neq\alpha}^{N} \mathbf{F}_{\alpha\beta}$. When Φ is the summation of pair potentials, $\phi_\alpha = \frac{1}{2}\sum_{\beta\neq\alpha}^{N} \phi_{\alpha\beta}(x_{\alpha\beta})$ where $x_{\alpha\beta} = |\mathbf{x}_{\alpha\beta}|$, $\mathbf{F}_{\alpha\beta}$ obviously means the force exerted on atom α from atom β. However, for some multibody potentials the meaning is not so straightforward.

(iii) The atomic potential energies depend only on interatomic distances, $\phi_\alpha = \phi_\alpha(x_{\alpha\beta}, x_{\alpha\gamma}, \ldots, x_{\beta\gamma})$. So $\boldsymbol{F}^\alpha = -\sum_{\beta\neq\alpha}^{N}\sum_{\gamma=1}^{N}(\partial\phi_\gamma/\partial x_{\alpha\beta})(\mathbf{x}_{\alpha\beta}/x_{\alpha\beta})$. This expression includes the possibility that α=γ. While this assumption clearly holds for radially symmetric potentials such as pair potentials and the embedded atom method

(EAM), it is necessary to consider the invariance of the system potential energy to show that it also holds for potentials that depend on bond orientations.

(iv) Each atomic potential energy depends only on the distances between the atom under consideration and all other atoms, $\phi_\alpha = \phi_\alpha(x_{\alpha\beta}, x_{\alpha\gamma}, \dots, x_{\alpha N})$. Thus, the force between atoms α and β can be expressed as $\mathbf{F}_{\alpha\beta} = -\{\partial\phi_\alpha/\partial x_{\alpha\beta} + \partial\phi_\beta/\partial x_{\alpha\beta}\}(\mathbf{x}_{\alpha\beta}/x_{\alpha\beta})$. Clearly, while this assumption holds for pair potentials and EAM, it does not for some multibody potentials such as the three-body potential of Stillinger Weber [90] used to model silicon.

Using the density functions shown above (Eq. 2.11) together with the conservations equations (Eq. 2.9) and by considering the four assumptions listed, Hardy developed the following expressions for stress and heat flux at a spatial point:

$$\boldsymbol{\sigma}(\mathbf{x}, t) = -\left\{\frac{1}{2}\sum_{\alpha=1}^{N}\sum_{\beta\neq\alpha}^{N}\mathbf{x}_{\alpha\beta}\otimes\mathbf{F}_{\alpha\beta}\,B^{\alpha\beta}(\mathbf{x}) + \sum_{\alpha=1}^{N} m_\alpha\tilde{\mathbf{v}}_\alpha\otimes\tilde{\mathbf{v}}_\alpha\psi(\mathbf{x}_\alpha-\mathbf{x})\right\} \tag{2.12}$$

where $\tilde{\mathbf{v}}_\alpha \equiv \mathbf{v}_\alpha - \mathbf{v}$.

$$\mathbf{q}(\mathbf{x}, t) = -\sum_{\alpha=1}^{N}\left[\sum_{\beta\neq\alpha}^{N}\frac{\partial\phi_\beta}{\partial x_{\alpha\beta}}\frac{\mathbf{x}_{\alpha\beta}\otimes\mathbf{x}_{\alpha\beta}}{x_{\alpha\beta}}B^{\alpha\beta}(\mathbf{x})\right]\cdot\tilde{\mathbf{v}}_\alpha + \sum_{\alpha=1}^{N}\left\{\frac{1}{2}m_\alpha(\tilde{v}_\alpha)^2 + \phi_\alpha\right\}\tilde{\mathbf{v}}_\alpha\psi(\mathbf{x}_\alpha-\mathbf{x}) \tag{2.13}$$

Hardy and colleagues also derived an expression for temperature by considering the equipartition theorem and the kinetic energy associated with atomic velocities relative to the velocity of the continuum at a spatial point [78]:

$$T(\mathbf{x}, t) = \frac{1}{3k_B}\frac{\sum_{\alpha=1}^{N} m_\alpha(\tilde{v}_\alpha)^2\psi(\mathbf{x}_\alpha-\mathbf{x})}{\sum_{\alpha=1}^{N}\psi(\mathbf{x}_\alpha-\mathbf{x})} \tag{2.14}$$

where k_B is Boltzmann's constant. This expression was not rigorously defined within the context of the same balance laws as was done for **σ** and **q**. However, it offers an ability to calculate T at an arbitrary location in an atomistic simulation similar to what is done for **σ** and **q**.

The ensemble average of the formulas given by Hardy for mass, momentum and energy density are equivalent to the corresponding formulas given by Irving and Kirkwood. The main difference is that Irving and Kirkwood used Dirac delta function instead of the general localization function. In stress and heat flux expressions, the infinite series are thus avoided and it is easy to implement Hardy's formulas in MD simulations.

2.6 MANY-REALIZATION METHOD

The many-realization method is employed to compute the ensemble averaged thermomechanical quantities without explicit knowledge of the density distribution function [91]. The microscopic states (i.e. atomic velocities and positions) corresponding to the same initial macroscopic state of the ensemble are sampled, and then the atoms in each realization are left to evolve into new microscopic states corresponding to the same macroscopic ensemble. The ensemble concept is also valid for non-equilibrium processes [89], and hence, the many-realization method can be applicable to analyze such processes (Fig. 2.3).

Figure 2.3 Schematic illustration of the many-realization method [92]

The procedure to implement the many-realization method is as follows:

1) Determine number of atoms, volume and energy of the NVE ensemble to be studied.

2) Set the number of atoms and the initial position of the atoms the same in each of the N realizations.

3) Initiate each of the N realizations of the ensemble (macroscopic state) by assigning each atom with a velocity sampled from the Maxwell-Boltzmann distribution at the prescribed temperature.

4) Let each realization evolve and equilibrate in parallel after atomic velocity and position is assigned.

5) Collect atomic velocities and positions from the N realizations as the system evolves to study systems under equilibrium state after equilibration is achieved.

6) Apply an external stress to the material model to drive the system to non-equilibrium if non-equilibrium process is to be investigated. Collect the atomic velocities and positions from the N realizations over time as the system evolves.

Thermomechanical quantities can be calculated at a selected time instant for the N realizations using Hardy's expressions and ensemble averaging can be performed over the N calculated values. For time averaging, data can be collected over N time steps at a randomly chosen realization and thus the thermomechanical quantities can be calculated and time averaging can be performed for this chosen realization.

3.0 COMPARISON BETWEEN ENSEMBLE AND TIME AVERAGING IN EVALUATING HARDY'S THERMOMECHANICAL QUANTITIES

In this Chapter, the 'many-realization approach' is implemented to evaluate the ensemble average of Hardy's stress/heat flux/temperature. Even though time and spatial averaging are conventional approaches to remove fluctuations of the computed thermomechanical quantities at finite temperature, ensemble average has a unique advantage in that it does not deteriorate the computed quantities when the thermomechanical process involved becomes farther away from equilibrium. In addition, the computed thermomechanical quantities from different realizations employed in evaluating the ensemble averaged values are not correlated, in contrast to the time and spatial averaged ones. Here correlation refers to the statistical relationship between two random variables or two sets of data. The superiority of ensemble averaging over time averaging will be demonstrated through computing the stress/heat flux/temperature for nickel (Ni) crystal in equilibrium and under shock impact. The convergence of the ensemble average and the time average of Hardy's expressions as well as different situations that time and ensemble averaging can be applicable will be discussed .

3.1 SIMULATIONS

A Ni crystal with dimensions of L_x =10[100], L_y=10[010], and L_z=20[001] in the *x*, *y*, and *z* direction is chosen for studying equilibrium systems. Free boundary conditions are applied to all the directions (Fig. 3.1a). The interaction of the Ni atoms is described by the embedded atom method (EAM) [86, 87, 93] interatomic potential. The many-realizations of the Ni NVE ensemble after initial energy minimization are simulated in parallel and 1000 realizations (simulations) are conducted in total. Each realization is initiated by assigning the atoms with the velocities sampled from the Maxwell-Boltzmann distribution defined by the temperature. The total number of atoms and their positions are kept the same after energy minimization. With the same initial kinetic energy (determined by temperature) and potential energy (determined by atomic position) among the different simulations, these realizations (simulations) constitute the same NVE ensemble. The realizations are then left to evolve and equilibrate before atomic velocities and positions are collected. Atomistic information at a chosen time instant after the system has achieved equilibrium is collected for the 1000 realizations and used for calculating ensemble-averaged thermomechanical quantities. For time averaging, atomistic information for an arbitrarily chosen realization is collected for 1000 times with different time intervals, every 10, 100 and 1000 time steps with time step size of 0.4 fs. Hardy's expressions for stress, heat flux, and temperature are calculated and their convergence using ensemble and time averaging are discussed.

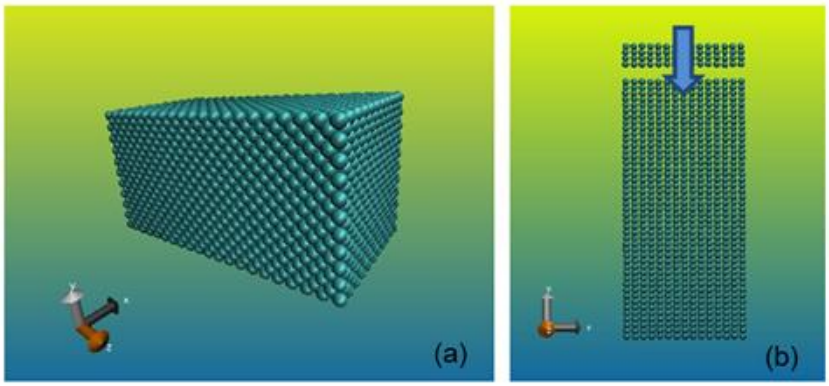

Figure 3.1 Snapshots of (a) nickel (Ni) crystal after energy minimization and (b) Ni crystal plate subjected to shock loading from dropping the Ni hammer on top [92]

A Ni plate is created for the study of the non-equilibrium system, with dimensions of L_x =16[100], L_y=25[011], and L_z=2.8[0$\bar{1}$1] in the *x*, *y*, and *z* direction. Periodic boundary conditions are applied to the *x* and *z* directions while free surface conditions are employed in the *y* direction (Fig. 3.1b). The interaction of the Ni atoms is also described by the EAM interatomic potential. Applying the many-realization method, 500 realizations with the same simulation setup described above are carried out. Each realization is initialized with atomic velocities randomly sampled at 300 K. After global thermal equilibrium has been achieved for the system, a smaller Ni plate is assigned with an initial constant velocity of 1500 m/s in the –*y* direction and subsequently induces an impact loading on top of the larger Ni plate, which results in a shock wave propagating in the plate. Atomistic information is collected at chosen time instants over the 500 realizations to construct the continuum thermomechanical fields using ensemble averaging. Time averaging is also used to construct the continuum thermomechanical fields through averaging the thermomechanical quantities calculated at 50 and 500 consecutive time steps with the time instant interested at the center of the averaging time window.

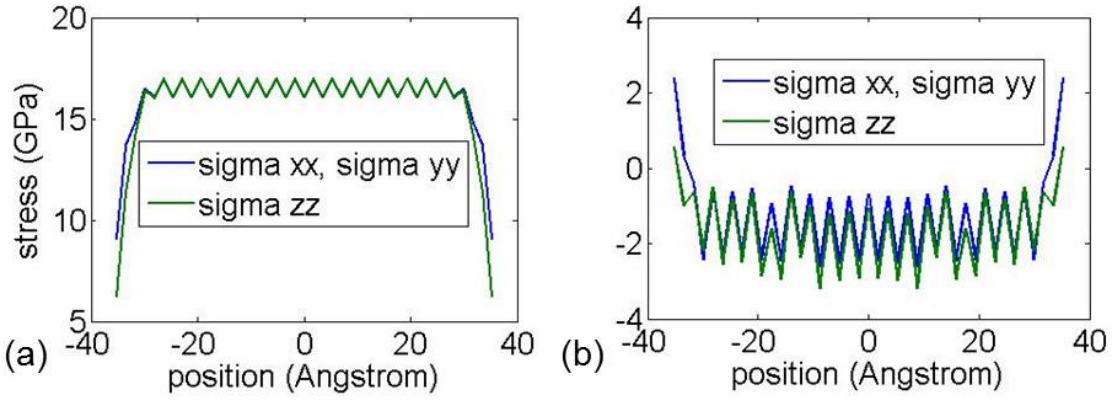

Figure 3.2 Stress profile for the Ni crystal (a) before energy minimization and (b) after energy minimization [92]

3.2 RESULTS AND DISCUSSIONS

To test the stress calculation using Hardy's expression, spatial points are chosen along the line in the *z* direction that passes through the 3D Ni crystal from the center of the surface in the negative *z* axis to the center of the surface in the positive *z* axis. The stress profile before and after energy minimization shows that before relaxation, the tensile stress near the surface is much lower than that in the middle (Fig. 3.2a), but after relaxation, the crystal becomes under tension at the surface and compression in the central region (Fig. 3.2b). The shear stresses not shown here are around zero, as expected. No ensemble or time averaging is employed in these calculations since this static case involves no thermal fluctuations introduced by a finite temperature.

For a Ni crystal that equilibrates at 300 K and 1000 K, the point at the center of the crystal is chosen to perform time and ensemble averaging on Hardy's expressions. Different time intervals have been chosen to perform time averaging, which means data is collected every 10,

100 and 1000 time steps for 1000 times, and the time averaging window size changes correspondingly. From the statistical point of view, either time or ensemble averaging in our study is to get estimated values of the expected thermomechanical quantities (stress/heat flux/temperature) by averaging the values calculated from randomly chosen microstates, which constitute a statistical sample. For ensemble averaging, the random variables (thermomechanical quantities) are obtained from the many-realizations that constitute the same NVE ensemble. For time averaging, the random variables are obtained from the different time instants as the system evolves. If the system is ergodic which is assumed here, the time and ensemble averaging should be equivalent on the condition that the time averaging is over the thermomechanical quantities calculated at every time step for infinite long time and ensemble averaging is over all the possible microstates which is also an infinite number. But in practice, the sample size should be restricted.

According to the central limit theorem in statistics, if the random variables are independent and identically distributed and the sample size is sufficiently large, the sample average would converge almost surely to the expected value. To have a good estimate of the expected value for the calculated thermomechanical quantities, it is therefore necessary to have a large enough sample size and have the random variables involved to be identically distributed and independent as well. For ensemble averaging, the many-realizations are conducted in parallel and thus evolve independently from each other. Therefore, the atomic quantities from the many-realizations should be independent, as are the thermomechanical quantities calculated from them. For time averaging, since the atomic information is collected from the same realization, autocorrelation needs to be considered. A large enough time interval is necessary to reduce the autocorrelation so that the thermomechanical quantities constitute a valid sample for calculating

expected values. With these basic conditions satisfied, the sample mean would reach the expected value with large enough sample size, when the computed thermomechanical quantities are considered to be accurate.

In our study, the expected values of the thermomechanical quantities are not always known in theory. In these situations, the computed quantities are assumed to be accurate when convergence of the quantities are achieved, i.e., the averaged quantities become stabilized with increasing number of averaging time steps and realizations. In the study below, the influence of different time intervals on convergence are investigated for time averaging. The sample size effects (the number of calculations for averaging) on convergence for both time and ensemble averaging are also studied.

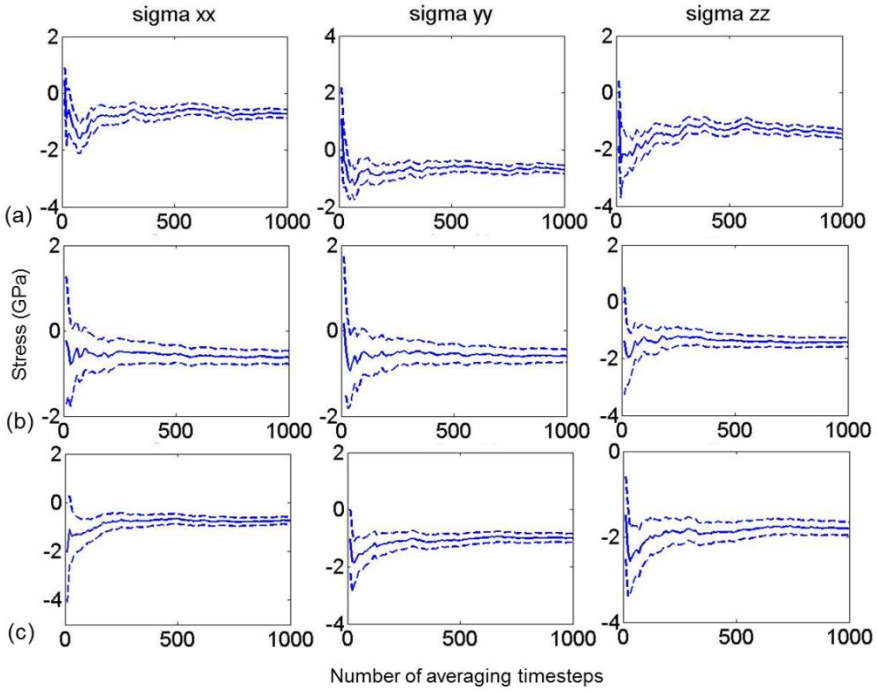

Figure 3.3 Convergence of time averaging for Hardy's stress with different averaging time interval at around 300 K: (a) every 10 time steps, (b) every 100 time steps, (c) every 1000 time steps with time step size = 0.4 fs [92]

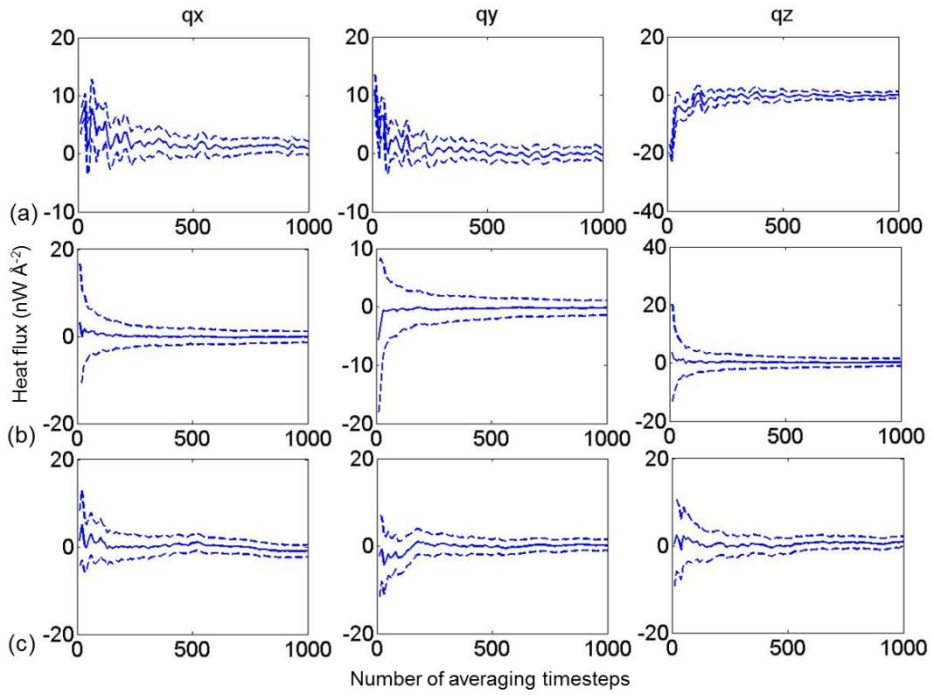

Figure 3.4 Convergence of time averaging for Hardy's heat flux with different averaging time interval at around 300 K: (a) every 10 time steps, (b) every 100 time steps, (c) every 1000 time steps with time step size = 0.4 fs [92]

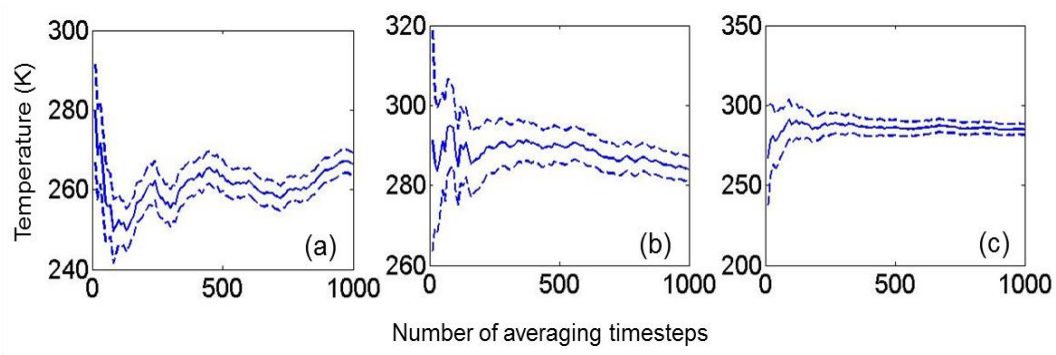

Figure 3.5 Convergence of time averaging for Hardy's temperature with different averaging time interval at around 300 K: (a) every 10 time steps, (b) every 100 time steps, (c) every 1000 time steps with time step size = 0.4 fs [92]

Convergence plots are made by plotting the averaged values (solid lines) of a number of calculations with their 95% confidence intervals (given by dotted lines) against the number of averaged calculations. Figures 3.3-3.5 show the convergence for stress, heat flux and temperature at 300 K with different time intervals using time averaging. From Fig. 3.3, it can be clearly seen that collecting data and calculating every 10 time steps (4 fs) can lead to larger fluctuations in the convergence curves for stress and heat flux. Obvious non-convergence can be observed for temperature as the convergence curve does not exhibit the smoothness and flatness even as the number of averaging time steps reaches 1000. Increasing the time intervals to 100 time steps significantly increases the convergence of time averaging for stress and heat flux. Compared with a time interval of 10 time steps, at the same number of averaging time steps, the convergence curves of stress and heat flux become smoother at a time interval of 100. Increasing the time intervals to 1000 time steps (0.4 ps) has only a negligible effect on the total features of the convergence curve of stress and heat flux much. The difference of convergence with different averaging time interval can be most clearly observed from the plots for temperatures. This is not surprising in that temperature solely depends on kinetic energy (decided by atomic velocities) while the dominating terms in stress and heat flux are potential energy (decided by atomic force and positions). The kinetic energy term has shown to more easily fluctuate at finite temperature (the ratio of fluctuation part is greater) compared with the potential energy term [69]. Large fluctuations for a time interval equal to 4 fs (10 time steps), and smoother curve at time interval equal to 40 fs (100 time steps) but with nonzero slope at the end and steady convergence can be observed at the time interval of 0.4 ps. Though the temperature for the whole system is set to be 300 K initially, the temperature can deviate from 300 K locally for a NVE ensemble. Similar tests are performed at 1000 K for a Ni crystal and the convergence tests for stress, heat flux and

temperature shows consistent results with that at 300 K. Increasing temperature from 300 K to 1000 K does not affect the convergence significantly.

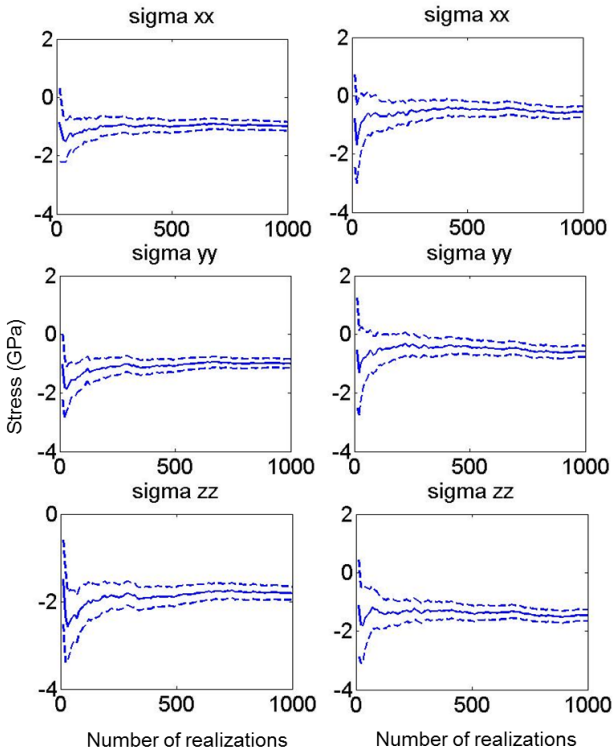

Figure 3.6 Convergence of ensemble averaging for Hardy's stress at temperatures around 300 K (left column) and 1000 K (right column) [92]

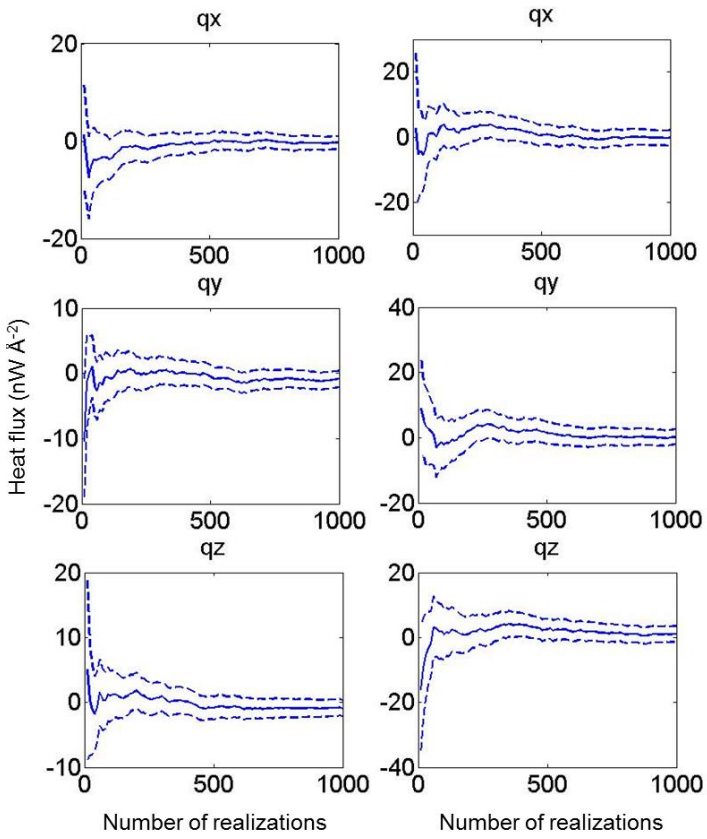

Figure 3.7 Convergence of ensemble averaging for Hardy's heat flux at temperatures around 300 K (left column) and 1000 K (right column) [92]

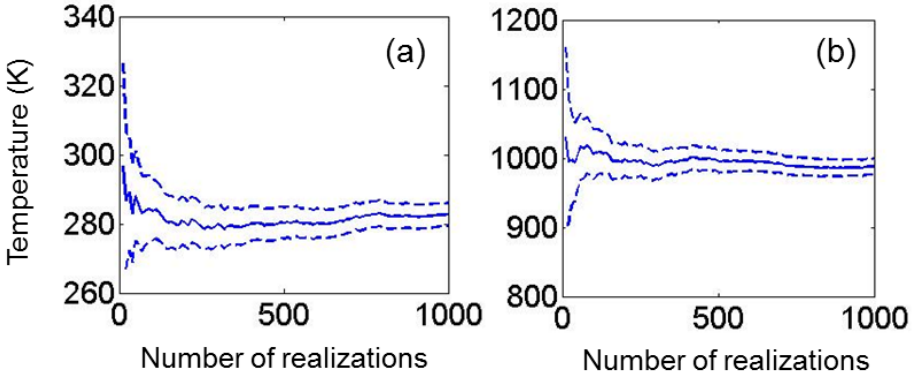

Figure 3.8 Convergence of ensemble averaging for Hardy's temperature at temperatures around (a) 300 K and (b) 1000 K [92]

Figures 3.6-3.8 demonstrate the convergence for the stress/heat flux/temperature at 300 K and 1000 K using ensemble averaging. It can be easily observed that at either temperature, the thermomechanical quantities achieve convergence with increasing averaging number of realizations. As mentioned previously, different realizations are simulated in parallel, and therefore the computed thermomechanical quantities in different realizations are independent and thus are not correlated. Compared with time averaging, ensemble averaging achieves convergence similar to time averaging with 1000 time steps interval. The confidence interval is about the same between time and ensemble averaging for the same averaging number of calculations.

As discussed above, it is desirable to have the thermomechanical quantities to be independent and identically distributed so that a valid sample is obtained for calculating the estimated values. To determine if the thermomechanical quantities are independent, it is necessary to investigate the correlation of the atomic velocities and positions. Figures 3.9-3.11 are the autocorrelation function (ACF) and power spectral density (PSD) of the velocity in three directions for a randomly chosen atom recorded for a certain time duration. The same atom is chosen for comparison between time averaging at 300 K and 1000 K and also between time and ensemble averaging. The ACF and PSD of the atomic position are also studied and plotted together with the velocity. For the thermomechanical quantities to be as independent as possible, the atomic velocities and positions collected should be least autocorrelated. It can be seen that the ACF for atomic velocity is quite high within 400 time steps and oscillate less drastically, afterwards. If the time interval chosen is less than this critical value (around 400 time steps), the correlation between at least two successive points would be significant. If the sample size is not large enough, the sample average will not give a good estimate. This explains why using a time

interval of 10 time steps, no good convergence can be reached with averaging time steps as large as 1000. In addition, the convergence can be improved gradually up to the time interval of 100 time steps because the autocorrelation has been reduced significantly. One can clearly observe the periodicity of the ACF and the critical time steps for choosing time interval is approximately consistent with this value.

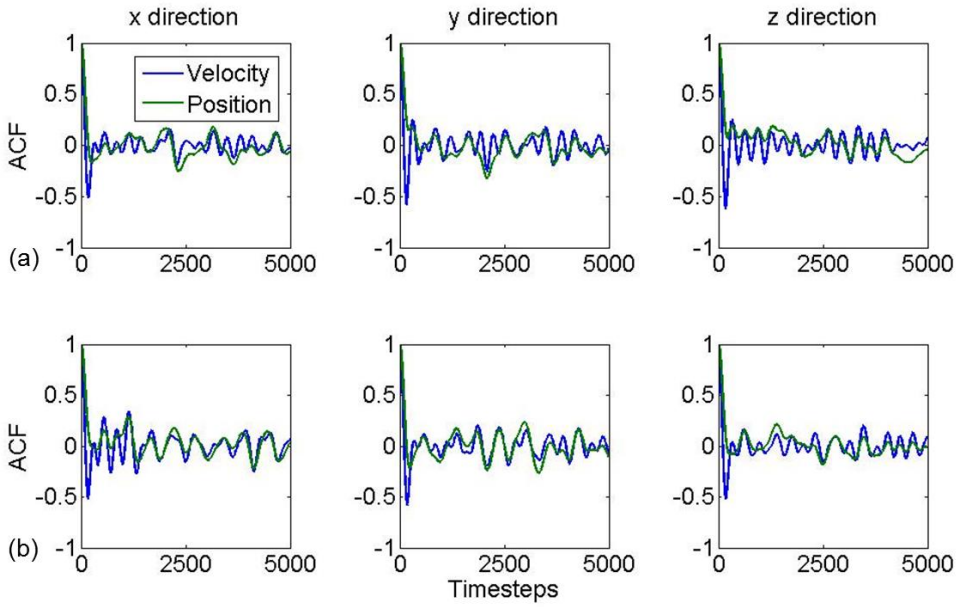

Figure 3.9 Autocorrelation function (ACF) of the velocity and position for a randomly chosen atom collected at every time step for 10000 time steps in a realization at (a) 300 K and (b) 1000 K, respectively [92]

The PSD of the velocity, which is also the Fourier transform of the ACF, demonstrates this critical frequency, at which the PSD has the highest value, is around 5~10 THz. In the time domain, this corresponds to 0.1~0.2 ps, which is 250~400 time steps with time step size of 0.4 fs. This critical atomic vibrational frequency can be estimated by using the Einstein model, which states that the solid is composed of single-frequency harmonic oscillators. Then the vibrational frequency $\nu = c_s/\lambda_{min}$, where c_s is the speed of sound inside the solid and λ_{min} is the minimum wavelength sustainable by the atomic lattice (about twice the lattice constant a). The sound

speed c_s can be computed by $\sqrt{(\lambda + 2\mu)/\rho}$, where λ and μ are respectively the first and second Lame's constants and ρ is material density. Utilizing the material properties for Ni (a=3.52 Å, λ=125 GPa, μ=76 GPa, and ρ=8.91 g cm^{-3}), the calculated vibrational frequency is around ~8.0 THz, which is consistent with what we found for the critical frequency through the frequency analysis of atomic velocity (i.e. 5~10 THz).

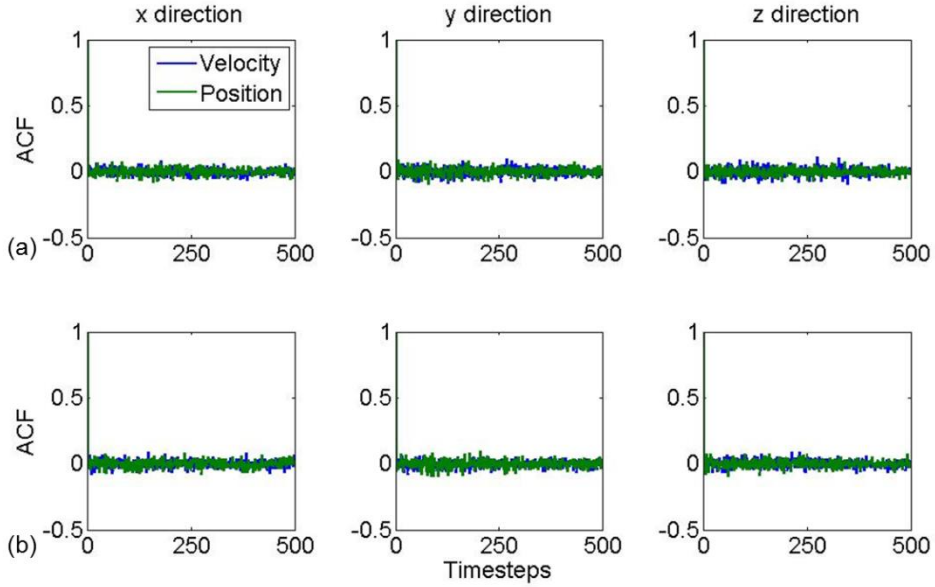

Figure 3.10 Autocorrelation function (ACF) of the velocity and position for a randomly chosen atom collected from the 1000 realizations at (a) 300 K and (b) 1000 K, respectively [92]

Comparing the velocity and position PSD and ACF, one can easily observe that position has stronger density at lower frequency content. However, its ACF also shows that the autocorrelation drops to a relatively small value almost at the same time steps as the velocity. Although it drops more slowly, it does not reach far in the negative direction. Therefore, one would expect the thermomechanical quantities that depend differently on atomic position and velocity may converge differently at the same chosen time interval. If the time interval is chosen

where the ACF for velocity is in the valley when that for position is a quite small value, the convergence of the quantities that are more dependent on velocity should be worse because position is less autocorrelated at this time interval. If the time interval chosen is smaller when the velocity has reached a lower value than position, the convergence for the quantities that are more dependent on position should be worse. The difference in convergence criterion, however, should not be large as long as the time interval is chosen to be larger than the critical value where the autocorrelations for both velocity and position lie in the flatter region. This chosen critical value (time interval) can be the same for position dependent quantities and for velocity dependent quantities as estimated by the Einstein model. The increased temperature does not affect the convergence noticeably as the comparison of PSD for the atom in system at 300K and 1000K shown, in Fig. 3.11, exhibits no significant shift in the critical frequency resulted from the temperature increase.

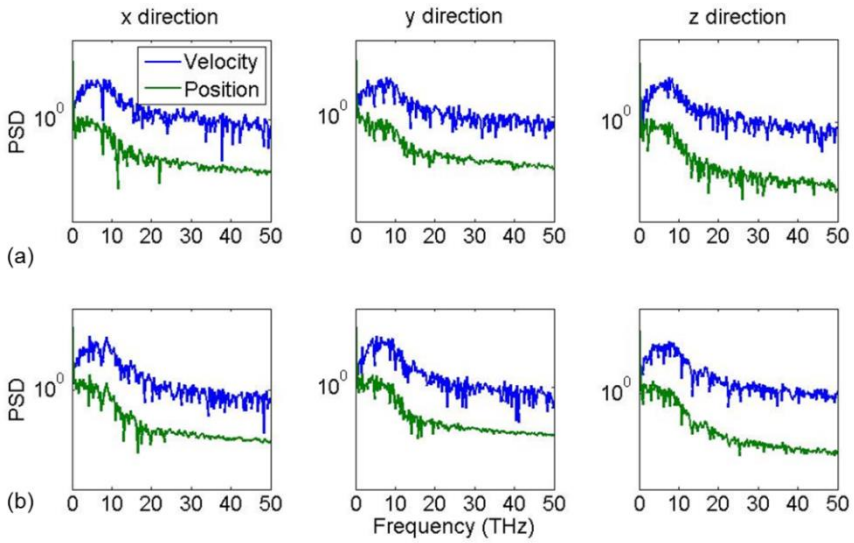

Figure 3.11 Power spectral density (PSD) of the velocity and position for a randomly chosen atom collected at every time step for 10000 time steps at (a) 300 K and (b) 1000 K, respectively [92]

The ACF plot for velocities and positions of the same atom at 300 K and 1000 K in ensemble averaging clearly shows no correlation among the different realizations. Therefore, if the time interval chosen for time averaging is not large enough, it is expected that ensemble averaging would lead to better convergence with the same sample size or that ensemble averaging can reach convergence with smaller sample size. This can be observed from the convergence plot. The convergence for ensemble averaging is better than time averaging with a time interval of 10 and 100 time steps. While with a time interval of 1000 time steps, time averaging and ensemble averaging seems equivalent as the autocorrelations for time averaging have been reduced a lot by then.

Equipped with the knowledge of applying time and ensemble averaging to equilibrium situations, we are going to analyze a highly non-equilibrium problem in which significant temporal gradient exists and time averaging most likely would fail. In the shock impact problem we chose to demonstrate the superior performance of ensemble averaging of the various thermomechanical fields evaluated at different time instants. Spatial points calculated are along the shock wave propagation direction at the center of the plate in the x and z directions. The stress/heat flux/temperature fields are constructed using ensemble averaging at different time instants (see Figs. 3.12-3.14). From the convergence plot of equilibrium systems, it has be observed that convergence (accuracy) can be achieved after approximately 400 realizations for ensemble averaging. Therefore, 500 realizations are chosen to conduct ensemble averaging to construct the thermomechanical fields in this shock impact problem. The dashed lines are from a randomly chosen realization before ensemble averaging is applied.

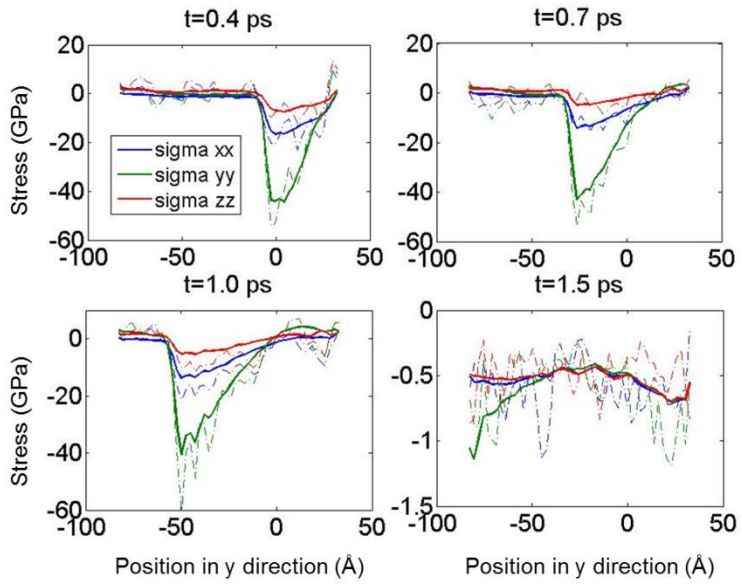

Figure 3.12 Stress profile constructed by ensemble averaging of the shock impacted nickel plate as the shock wave propagates, and dash lines are chosen from a random realization without averaging [92]

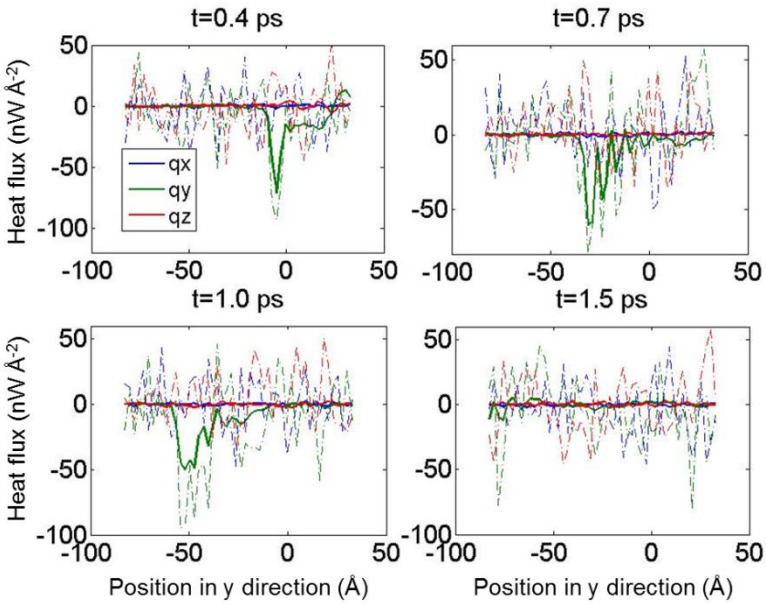

Figure 3.13 Heat flux profile constructed by ensemble averaging of the shock impacted nickel plate as the shock wave propagates, and dash lines are chosen from a random realization without averaging [92]

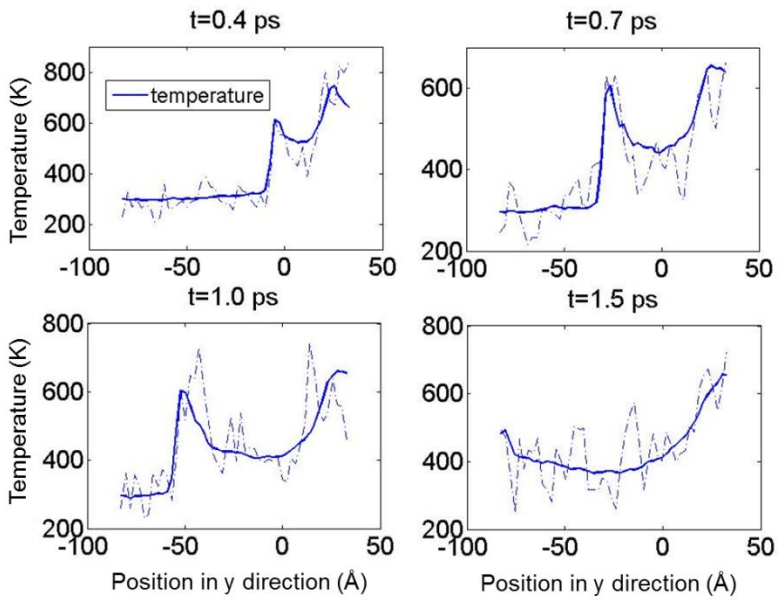

Figure 3.14 Temperature profile constructed by ensemble averaging of the shock impacted nickel plate as the shock wave propagates, and dash lines are chosen from a random realization without averaging [92]

Before the shock wave arrives, the crystal has already equilibrated at 300 K, is in slight compression at the center, and experiences no heat flux in any direction at the spatial points chosen for analysis. It can be observed that the shock wave propagation in the *y* direction leads to strong compression, heat flux in the *y* direction, and significant temperature rise at the shock front. In the *x* and *z* directions, which are perpendicular to the shock wave propagation direction, the stresses also vary, but the heat fluxes remain close to zero. This fast propagating shock wave and the corresponding rapidly varying thermomechanical fields present great difficulty for time averaging to perform well. From the experience gained from analyzing the same material at equilibrium, especially through studying the ACF, we have obtained a good estimate of the thermomechanical quantities when the averaging number of time steps is at least 400 and the time interval is 250 time steps (0.1 ps). Therefore, a time window size of 40 ps is needed to achieve convergence. With the wave propagating speed in the shock impact problem, the actual

thermomechanical fields have varied drastically within the time duration of 40 ps. Therefore, it is impossible to build high fidelity thermomechanical fields using this window size for time averaging, and thus, only reduced time interval and window size will be considered for this kind of highly non-equilibrium problem.

As a result, stress, heat flux and temperature are constructed with the chosen time instant in the middle of the time window and a time interval of single time step is applied (0.4 fs). The total averaging time steps of 50 and 500 are employed, respectively, and the results are shown in Fig. 3.15. For stress and heat flux, only results for σ_{yy} and q_y are shown here because the spatial and temporal gradients are greatest in the wave propagating direction. It can be easily observed that the thermomechanical profiles with averaging time steps of 50 resemble the noisy profiles without averaging. This is especially obvious for the plot of heat flux where the gradient around the shock front is almost unidentifiable from the thermal noise. However, when the larger time averaging window size is applied (averaging time steps equal to 500), the peaks at the shock front are widened and even shifted, although smoother curves can be obtained. Therefore, ensemble averaging is more desirable in this case.

Computational expense is also a consideration because constructing thermomechanical fields using ensemble averaging requires hundreds of simulations. Therefore, if the thermomechanical fields are slowly varying in time or in equilibrium, time averaging would still be a first option because ensemble averaging requires much more computational cost on simulations. However, for a highly non-equilibrium system where the thermomechanical fields change very rapidly, ensemble averaging is certainly more suitable. In addition, the more accurately computed thermomechanical fields using ensemble averaging can be employed to investigate the validity of continuum thermomechanical equations, especially in non-equilibrium

situations. The problem related with computational cost can be alleviated by the rapid development of parallel computing techniques.

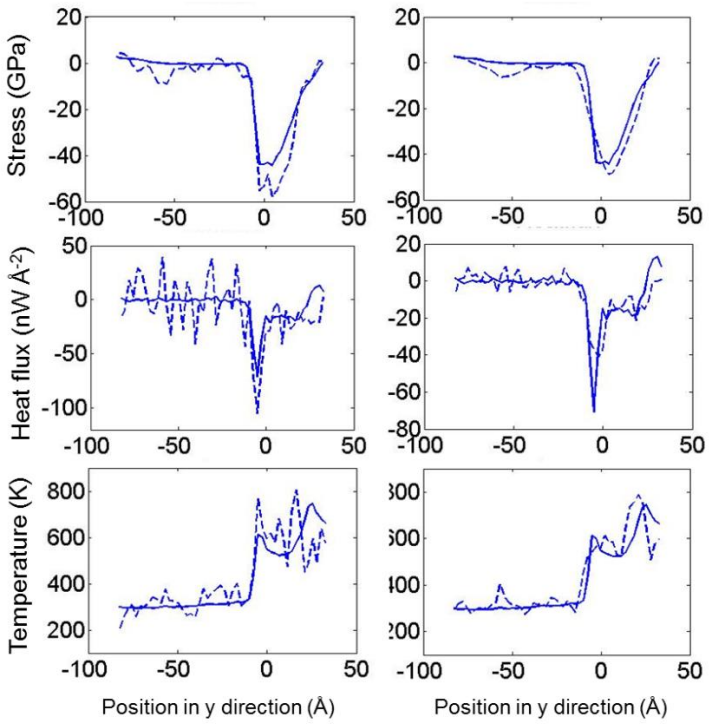

Figure 3.15 Comparison between ensemble (solid line) and time (dashed line) averaging with 50 (left column) and 500 (right column) averaging time steps at t=0.4 ps [92]

3.3 CONCLUSIONS

In this chapter, ensemble averaging is applied to evaluate Hardy's stress, heat flux, temperature expressions for the first time through a many-realization approach. Comparison between the convergence of time and ensemble averaging has been performed for a Ni crystal that equilibrates at 300 K and 1000 K, as well as that under shock impact. This study thoroughly investigates the two averaging methods in details and provides specific guidance on

implementing the two methods. The thermomechanical fields have been constructed for a shock impact problem by ensemble and time averaging respectively. The following conclusions can be drawn:

1. Time interval and the number of averaging timesteps are important factors when time averaging is employed to compute various thermomechanical quantities. It is found that a critical time interval exists for a given material such that the atomistic quantities sampled and the associated thermomechanical quantities have little correlation among themselves. This critical time interval can be estimated by the Einstein model using the material's sound velocity. For equilibrium system, time averaged thermomechanical quantities with a sufficient large time interval are almost equivalent to the ensemble averaged ones.
2. Stress converges faster than heat flux and temperature with the same number of averaging points. This is because stress primarily depends on atomic forces and velocities, in comparison heat flux and temperature are more related to atomic velocities, and atomic forces and positions fluctuate less than atomic velocities at finite temperatures. Increase in temperature mainly leads to an increase in the variance of the computed quantities, but does not affect their convergence rate.
3. For highly nonequilibrium systems in which the thermomechanical fields drastically vary with time, ergodic theorem is no longer applicable and enlarging time window size only leads to less accurate estimation of the thermomechanical quantities. Ensemble averaging is the only appropriate way to obtain the expectation value in this case. The number of realizations can be chosen based on analyzing the corresponding equilibrium ensemble. Because the variance of atomistic quantities may increase in nonequilibrium conditions, it is neccessary to employ larger number of realizations than that in equilibrium studies. The

main disadvantage of ensemble averaging is its computational expense, but with ever increasing computing power, this disadvantage will become less of an issue in the future.

4.0 ON THE VALIDITY AND APPLICABILITY OF HARDY'S THEORY TO NON-EQUILIBRIUM PROCESSES MODELED AT ATOMISTIC SCALE

Even though Hardy's thermomechanical quantities have been derived analytically to obey continuum conservation laws, they have never been proven numerically, especially for non-equilibrium processes. Therefore, the main task of this Chapter is to investigate the validity of Hardy's theory by using the continuum conservations laws to test the computed Hardy's themomechanical quantities for a few non-equilibrium processes. Gaussian pulse and shock wave propagating in one dimensional (1D) gold (Au) chain, 3D Au and Ni bar are simulated, for which the interatomic interaction is described by harmonic, Morse and EAM potentials, respectively. Since these highly dynamic processes happen in systems with different dimensions and modeled by various potentials, they represent a wide variety of problems for testing the applicability of Hardy's formulas and ensemble averaging approach. In Hardy's theory, ensemble averaging is not required for the validity of conservation equations, in contrast to Irving and Kirkwood's formalism [75]. Here, the question of whether the ensemble averaged Hardy's continuum quantities obey conservation equations will also be answered.

4.1 VALIDATION PROCEDURE

Hardy's formulas will be validated by comparing two sides of the conservation equations using the computed quantities at the spatial points chosen along the 1D Au chain and the central line of 3D Au and Ni bar. These points are located along the Gaussian/shock wave propagation direction and where the thermomechanical fields change most drastically. For this purpose, the conservation equations will be discretized by the finite difference method.

The conservation equations of mass, linear momentum and energy for a continuum point given in Chapter 2 (Eq. 2.9) are obeyed in the analytical development of Hardy's formulas. The conservation equations can be rewritten by using total time derivative $\frac{\mathrm{d}}{\mathrm{d}t}$ instead of the partial time derivative $\frac{\partial}{\partial t}$ in Eq. 2.9, and body force and energy source are not considered in the equations below:

Balance of Mass
$$\frac{\mathrm{d}\rho}{\mathrm{d}t} = -\rho\, \boldsymbol{\nabla}\cdot\mathbf{v} \tag{4.1a}$$

Balance of Momentum
$$\rho\frac{\mathrm{d}\mathbf{v}}{\mathrm{d}t} = \boldsymbol{\nabla}\cdot\boldsymbol{\sigma} \tag{4.1b}$$

Balance of Energy
$$\frac{\mathrm{d}e}{\mathrm{d}t} = \boldsymbol{\sigma}:(\boldsymbol{\nabla}\mathbf{v}) - \boldsymbol{\nabla}\cdot\mathbf{q} \tag{4.1c}$$

where $\frac{\mathrm{d}\rho}{\mathrm{d}t} = \frac{\partial\rho}{\partial t} + \nabla_x\rho\cdot\mathbf{v}$ is the material time derivative of ρ, $\frac{\mathrm{d}\mathbf{v}}{\mathrm{d}t}$ is the material time derivative of **v,** $\frac{\mathrm{d}e}{\mathrm{d}t}$ is the material time derivative of *e*. $\boldsymbol{\nabla}\cdot\mathbf{v} = v_{i,i}$, $\boldsymbol{\nabla}\mathbf{v} = v_{i,j}\mathbf{e}_i\otimes\mathbf{e}_j$ and $\boldsymbol{\nabla}\cdot\boldsymbol{\sigma} = \sigma_{ij,j}\mathbf{e}_i$, where *i=x,y,z.* Equations 2.9 and 4.1 can be derived from one another [94, 95]. Whereas Eq. 2.9 is more commonly applied to fluid dynamics problems, Eq. 4.1 is mainly employed for solid mechanics analysis.

For 3D problems, discretized version of the conservation equations by finite difference method can be expressed as Eq. 4.2. Note here the balance of momentum is only written in the wave propagation direction (*y* direction in this Chapter).

$$\frac{\rho^{(j+1)}-\rho^{(j)}}{\delta t}+\left\{\frac{\rho^{(i+1)}-\rho^{(i)}}{\delta x}v_x+\frac{\rho^{(k+1)}-\rho^{(k-1)}}{2\delta y}v_y+\frac{\rho^{(m+1)}-\rho^{(m)}}{\delta z}v_z\right\}$$
$$=-\rho\left\{\frac{{v_x}^{(i+1)}-{v_x}^{(i)}}{\delta x}+\frac{{v_y}^{(k+1)}-{v_y}^{(k-1)}}{2\delta y}+\frac{{v_z}^{(m+1)}-{v_z}^{(m)}}{\delta z}\right\} \tag{4.2a}$$

$$\rho\frac{{v_y}^{(j+1)}-{v_y}^{(j)}}{\delta t}+\rho\left\{\frac{{v_y}^{(i+1)}-{v_y}^{(i)}}{\delta x}v_x+\frac{{v_y}^{(k+1)}-{v_y}^{(k-1)}}{2\delta y}v_y+\frac{{v_y}^{(m+1)}-{v_y}^{(m)}}{\delta z}v_z\right\}$$
$$=\frac{{\sigma_{yx}}^{(i+1)}-{\sigma_{yx}}^{(i)}}{\delta x}+\frac{{\sigma_{yy}}^{(k+1)}-{\sigma_{yy}}^{(k-1)}}{2\delta y}+\frac{{\sigma_{yz}}^{(m+1)}-{\sigma_{yz}}^{(m)}}{\delta z} \tag{4.2b}$$

$$\frac{e^{(j+1)}-e^{(j)}}{\delta t}+\left\{\frac{e^{(i+1)}-e^{(i)}}{\delta x}v_x+\frac{e^{(k+1)}-e^{(k-1)}}{2\delta y}v_y+\frac{e^{(m+1)}-e^{(m)}}{\delta z}v_z\right\}$$
$$=\begin{bmatrix}\sigma_{xx}&\sigma_{xy}&\sigma_{xz}\\ \sigma_{yx}&\sigma_{yy}&\sigma_{yz}\\ \sigma_{zx}&\sigma_{zy}&\sigma_{zz}\end{bmatrix}:\begin{bmatrix}\frac{{v_x}^{(i+1)}-{v_x}^{(i)}}{\delta x}&\frac{{v_x}^{(k+1)}-{v_x}^{(k-1)}}{2\delta y}&\frac{{v_x}^{(m+1)}-{v_x}^{(m)}}{\delta z}\\ \frac{{v_y}^{(i+1)}-{v_y}^{(i)}}{\delta x}&\frac{{v_y}^{(k+1)}-{v_y}^{(k-1)}}{2\delta y}&\frac{{v_y}^{(m+1)}-{v_y}^{(m)}}{\delta z}\\ \frac{{v_z}^{(i+1)}-{v_z}^{(i)}}{\delta x}&\frac{{v_z}^{(k+1)}-{v_z}^{(k-1)}}{2\delta y}&\frac{{v_z}^{(m+1)}-{v_z}^{(m)}}{\delta z}\end{bmatrix}$$
$$-\left\{\frac{{q_x}^{(i+1)}-{q_x}^{(i)}}{\delta x}+\frac{{q_y}^{(k+1)}-{q_y}^{(k-1)}}{2\delta y}+\frac{{q_z}^{(m+1)}-{q_z}^{(m)}}{\delta z}\right\} \tag{4.2c}$$

Here ${\sigma_{xx}}^{(ikmj)}$ represents $\sigma_{xx}(x_i, y_k, z_m, t_j)$ and similarly for $\rho^{(ikmj)}$, $\mathbf{v}^{(ikmj)}({\mathrm{v}_p}^{(ikmj)})$, $\mathbf{q}^{(ikmj)}({q_p}^{(ikmj)})$ and $e^{(ikmj)}$, $p = x, y, z$. For simplicity, superscript are not explicitly written at (x_i, y_k, z_m, t_j). For example, ${\sigma_{xx}}^{((i+1)kmj)}$ is written as ${\sigma_{xx}}^{(i+1)}$. $\delta x = x_{i+1} - x_i$, $\delta y = y_{k+1} - y_k, \delta z = z_{m+1} - z_m$ and $\delta t = t_{j+1} - t_j$. δt is chosen to be the simulation time step size 1 fs and δx≈0.5 Å for 1D cases. For 3D problems, δt is chosen to be the simulation time step size 1 fs and δx= δz=0.2 Å and δy≈0.2 Å. The spatial discretization is chosen to be small enough so that there is no obvious change in the two sides of the balance laws. The conservation equations for 3D problems are plotted against the *y* coordinates of spatial points, which is the direction along which wave propagates.

In 1D cases, Eqs. 4.2 can be simplified as below since only quantities along the *x* direction are nonzero:

Balance of Mass
$$\frac{\rho^{(j+1)} - \rho^{(j)}}{\delta t} + \frac{\rho^{(i+1)} - \rho^{(i-1)}}{2\delta x} v_x = -\rho \frac{{v_x}^{(i+1)} - {v_x}^{(i-1)}}{2\delta x} \tag{4.3a}$$

Balance of Momentum
$$\rho\left\{\frac{{v_x}^{(j+1)} - {v_x}^{(j)}}{\delta t} + \frac{{v_y}^{(i+1)} - {v_y}^{(i-1)}}{2\delta x} v_x\right\} = \frac{{\sigma_{xx}}^{(i+1)} - {\sigma_{xx}}^{(i-1)}}{2\delta x} \tag{4.3b}$$

Balance of Energy
$$\frac{e^{(j+1)} - e^{(j)}}{\delta t} + \frac{e^{(i+1)} - e^{(i-1)}}{2\delta x} v_x = \sigma_{xx} \frac{{v_x}^{(i+1)} - {v_x}^{(i-1)}}{2\delta x} - \frac{{q_x}^{(i+1)} - {q_x}^{(i-1)}}{2\delta x} \tag{4.3c}$$

Thermomechanical quantities are computed in terms of atomic variables at the chosen spatial points and time instants using Hardy's formulas. The agreement between the two sides of the balance laws are tested by plotting the left hand side (LHS) and right hand side (RHS) of the

equations. In this Chapter, LHS of the conservation equations are always represented in blue line while RHS in green line.

4.2 SIMULATIONS

Wave propagation in a 1D Au chain initiated by a Gaussian pulse is investigated in our study. The Gaussian pulse is initiated in the middle of the 1D Au chain that consists of 500 atoms, for which the nearest neighboring atomic interaction is described by harmonic potential (Eq. 4.4) and Morse potential (Eq. 4.5), respectively:

$$U(r_{ij}) = D_e \alpha^2 (r_{ij} - r_0)^2 \tag{4.4}$$

$$U(r_{ij}) = D_e \left(1 - e^{-\alpha(r_{ij} - r_0)}\right)^2 \tag{4.5}$$

where r_{ij} is the distance between atoms *i* and *j*, r_0 is the equilibrium bond distance, D_e is the energy well depth relative to the dissociated atoms and α controls the width of the potential. The harmonic potential used here is actually the linearized Morse potential for 1D gold chain. The initial displacement introduced by the Gaussian pulse of amplitude *A* and width σ is given by Eq. 4.6:

$$u(x, t = 0) = \begin{cases} A \dfrac{e^{-(x/\sigma)^2} - u_c}{1 - u_c}, & |x| \le L_c \\ 0, & |x| > L_c \end{cases} \tag{4.6}$$

where the pulse is truncated at $x = \pm L_c$ and $u_c = e^{-(L_c/\sigma)^2}$. Wave propagating is simulated for the 1D gold chain that is at 0 K and that equilibrates at 300 K, respectively. The values used for the parameters of the Gaussian pulse are σ = 10.0 a, $A = a$ and L_c = 4.0 σ at 0 K and σ = 10.0 a,

A = 2.0 a and L_c = 4.0 σ at 300 K. The displacement of the atoms in the 1D chain simulated using harmonic potential at 0 K at different snapshots is shown in Fig. 4.1. The propagating wave initiated by the Gaussian pulse in the *y* direction is also investigated in 3D Ni bar having dimensions L_x =4[100], L_y=50[010], and L_z=4[001] in the *x*, *y*, and *z* directions. Free surface boundary conditions are applied to all directions and EAM potential developed by Foiles et al. [86, 87] are employed to describe the atomic interaction of the Ni bar. The values used for the parameters of the Gaussian pulse in 3D cases are σ = 5.0 r_0, A = 0.5 r_0 and L_c = 2.0 σ. Similar test is also conducted in a 3D Au bar of the same dimension as the Ni bar, for which the atomic interaction is described by the Morse potential. The parameters of the Morse potential for the 1D and 3D Au are listed in Table 4.1.

Table 4.1 Lattice parameter *a*, and Morse potential parameters D_e, α and r_0 for Au [96-98]

	a (Å)	D_e (eV)	α (Å^{-1})	r_0 (Å)
1D	2.922	0.5600	1.6370	2.9220
3D	4.070	0.1071	1.9788	2.9372

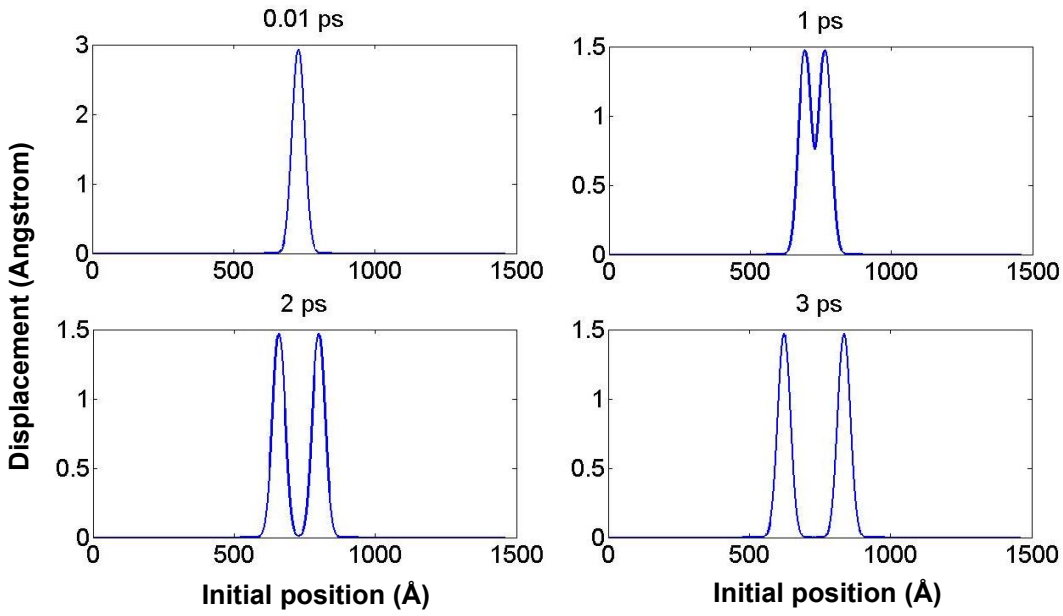

Figure 4.1 Displacement of the atoms in the harmonic chain during the Gaussian pulse propagates at initially 0 K at different time instants [98]

Highly non-equilibrium process of shock wave propagation in 1D and 3D cases are then investigated. For the 1D gold chain, the shock wave is initiated by assigning velocities of 1000 m/s in the +x direction to five atoms at one end of the chain described by Morse potential that is at 0 K and that equilibrates at 300 K, respectively. For the 3D case, shock impact is introduced by assigning velocities of 1000 m/s in the *-y* direction (see Fig. 4.2) to the atoms within two lattice distance in the *y* direction at the end of the Ni bar described by EAM potential initally at 0 K (Fig. 2). Shock wave propagation in 3D Ni bar is also investigated at 300 K, and the many-realization method described in Ch. 2.5 is used to evaluate ensemble averaged values of the thermomechanical quantities in order to remove thermal noise and preserve high spatial and temporal gradients of the thermomechanical fields. Totally, 500 realizations are conducted in parallel and ensemble averaging of the Hardy's quantities is performed over the 500 realizations.

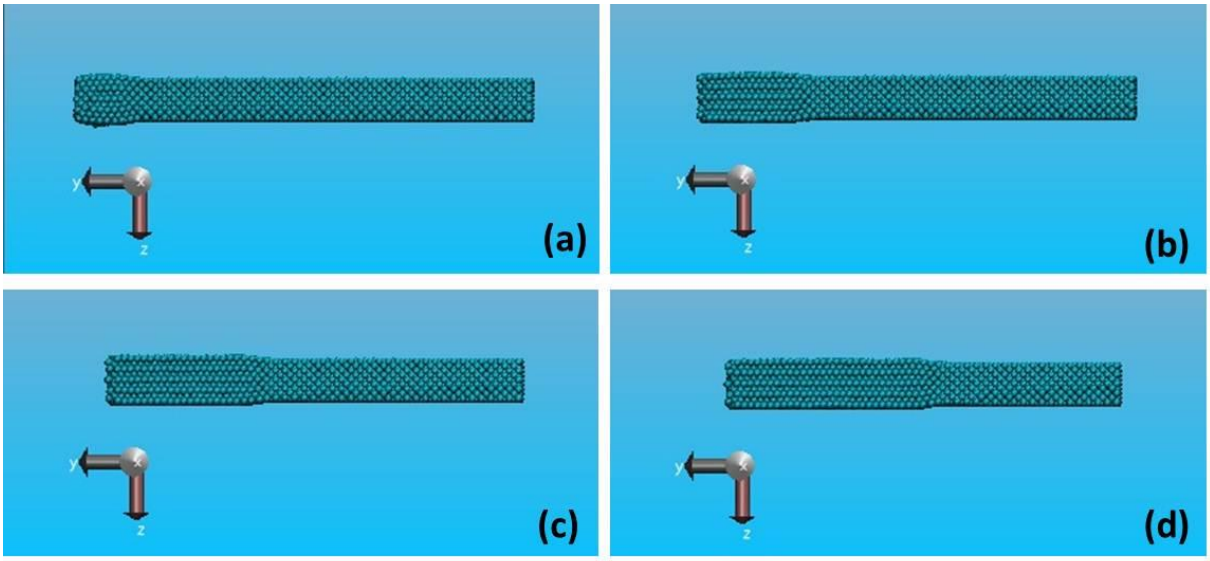

Figure 4.2 Displacement of the atoms in the 3D Ni crystal during the shock wave propagates at initially 0 K at (a) 1 ps (b) 3 ps (c) 5 ps and (d) 7 ps [98]

The characteristic volume used in our study for the 1D problems is a cylinder with cross-section area of 1 Å^2 and length L of 4.8 r_0 unless otherwise stated. For the 3D problems the volume is a sphere with radius R_c of 1.5 times the lattice constant. The localization function $\psi(r)$ used for 1D and 3D problems in Chapters 4 and 5 are given as Eq. 4.7, respectively as:

$$\psi(r) = \begin{cases} \sim\left\{1 - 2\left(\frac{r}{L}\right)^2 + \left(\frac{r}{L}\right)^4\right\}, & r = |\mathbf{x}_{\boldsymbol{\alpha}} - \mathbf{x}| < L \\ 0, & \text{otherwise} \end{cases} \tag{4.7a}$$

$$\psi(r) = \begin{cases} \sim\left\{1 - 3\left(\frac{r}{R_c}\right)^2 + 2\left(\frac{r}{R_c}\right)^3\right\}, & r = |\mathbf{x}_{\alpha} - \mathbf{x}| < R_c \\ 0, & otherwise \end{cases} \tag{4.7b}$$

4.3 RESULTS AND DISCUSSIONS

Figure 4.3 shows the stress and heat flux profiles along the chain at different time instants as the Gaussian wave propagates, showing nonzero values mainly at the wave fronts. Figure 4.4 compares the two sides of the balance of momentum with different characteristic volume chosen for the localization function and shows good agreement between the two sides in all cases. There are some noticeable spikes around the mean values for both stress's spatial derivative (i.e., RHS) and velocity's time derivative (i.e., LHS) when characteristic volume is small. These spikes are observed to diminish in number and magnitude as the characteristic volume increases, but the tradeoff is the over-smoothing of the curves as observed from the smaller peaks at position 700 Å and 750 Å in Fig. 4.4. A length of 4.8 r_0 is chosen for the characteristic volume in all 1D cases, because this choice seems to preserve the sharp features of conservation equations and reduce the number and amplitude of spikes.

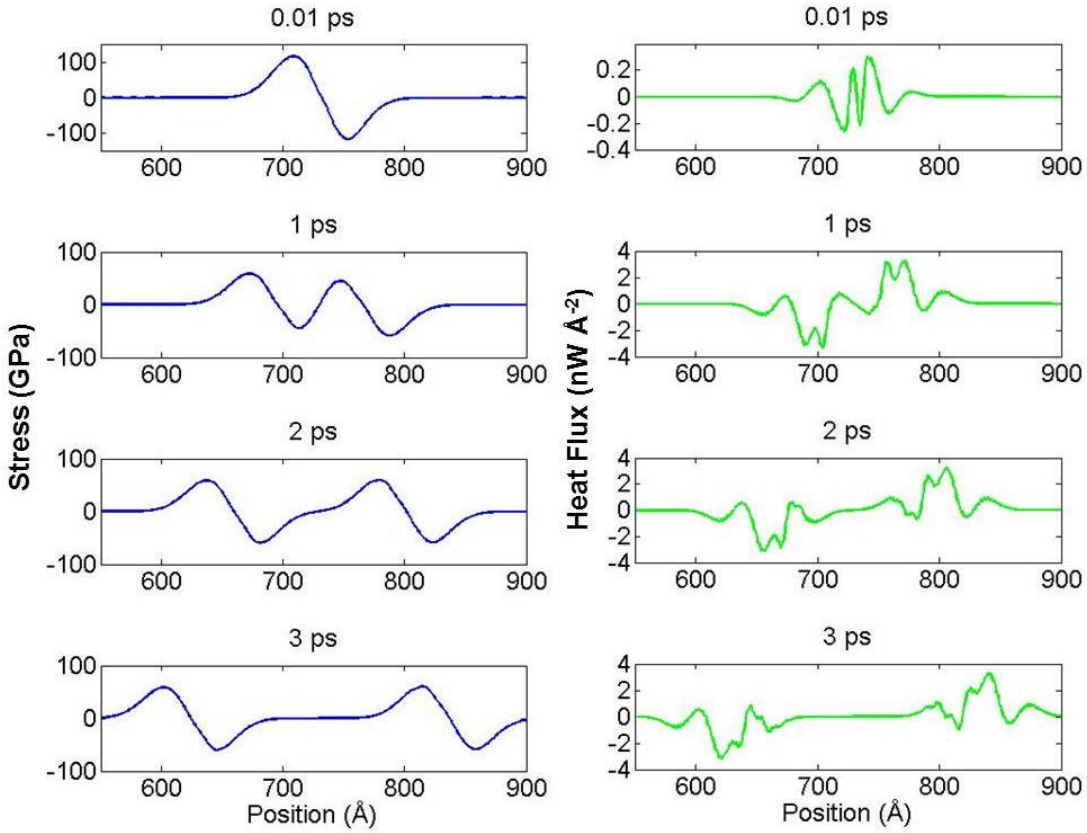

Figure 4.3 Stress and heat flux profiles as the Gaussian wave propagates in the harmonic chain at different time instants at initially 0 K (length of the characteristic volume is chosen to be 4.8 r_0) [98]

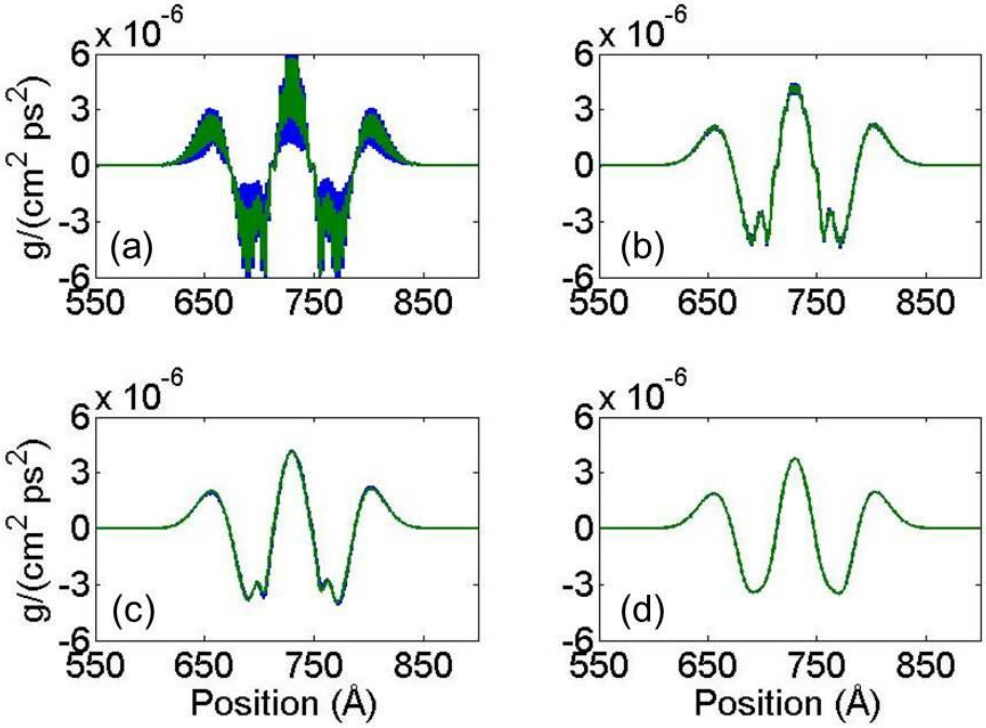

Figure 4.4 Comparison between two sides of balance of momentum as the Gaussian pulse propagates in the harmonic chain at initially 0 K with different length of the characteristic volume (a) length=1.2 r_0 (b) length=2.4 r_0 (c) length=4.8 r_0, and (d) length=9.6 r_0 at the time instant t=1 ps [98]

The behavior of Hardy's expressions with changing characteristic volume is due to the different number of atoms included in the characteristic volume. Even with uniform spacing of atoms having zero velocity at the area away from wave fronts, a different number of atoms can be included as the spatial point changes from point to point. For example, when the spatial point is located at the site of the atom, only one atom is included in the characteristic volume with a length of 1.2 r_0. If the spatial point is located in the middle between two atoms, these two atoms will be included. This effect can be magnified at wave front, which can affect density, velocity and energy by the varying number of atoms contributing to the calculation of the corresponding properties. For stress and heat flux, this can also affect the number of individual interacting atomic pairs in the potential term of the respective expressions. As characteristic volume

increases, the number of atoms in the characteristic volume and pairs of atoms in the potential terms change less significantly as the spatial point changes. Thus, this explains why the spikes in the spatial derivative diminish with increasing characteristic volume (see Fig. 4.4). Similarly, small characteristic volume is more sensitive to atom reconfiguration with time at a fixed spatial point. Therefore, the spikes of time derivative are also reduced as characteristic volume increases.

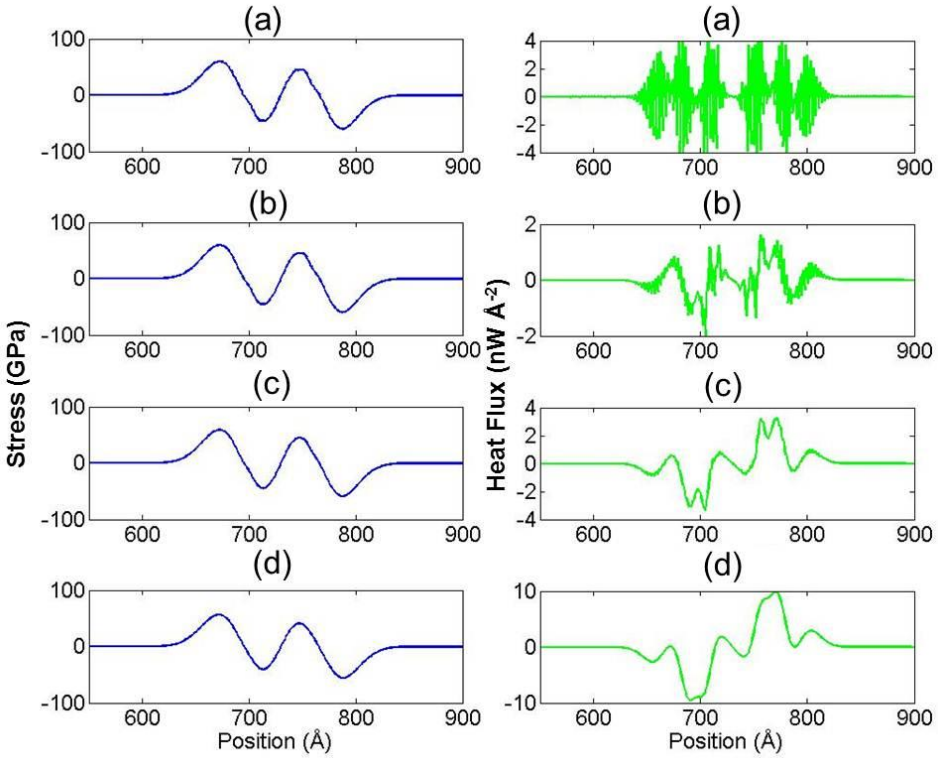

Figure 4.5 Stress and heat flux as the Gaussian pulse propagates in the harmonic chain at initially 0 K with different length of the characteristic volume (a) length=1.2 r_0 (b) length=2.4 r_0 (c) length=4.8 r_0, and (d) length=9.6 r_0 at the time instant t=1 ps [98]

The influence of characteristic volume change on stress and heat flux is shown in Fig. 4.5. Changing characteristic volume does not affect the stress profile but affects heat flux, significantly. In theory, the mechanical energy introduced by the Gaussian pulse should

propagate in the form of a mechanical wave without heat dissipation. Thus no heat flux is supposed to be observed in the harmonic chain as the wave propagates. However, the calculation from Hardy's heat flux expression generates values that are nonzero and vary with different characteristic volume. Comparing expressions for stress and heat flux given by Hardy (Eqs. 2.12 and 2.13), the dominating term in the stress expression is the potential term and so is in the heat flux expression. The steady profile of stress indicates the potential term of stress is insensitive to changing characteristic volumes, which should be the same for the potential term inside the bracket of heat flux due to their resemblance. The changing heat flux with length of the characteristic volume is due to the relative velocity, $\tilde{\mathbf{v}}_\alpha$, outside the bracket. From the physical point of view, $\tilde{\mathbf{v}}_\alpha$ should be zero as there is no thermal fluctuation for individual atoms in a harmonic chain at an initial 0 K ($\tilde{\mathbf{v}}_\alpha$ is used to compute local temperature in Hardy's expression). However, it can be easily seen that Hardy's expression would give nonzero $\tilde{\mathbf{v}}_\alpha$ and thus nonzero temperature at the wave front; and the value of $\tilde{\mathbf{v}}_\alpha$ can vary a lot with changing characteristic volume.

As pointed out by Webb III et al., one may obtain erroneous material velocity, $\mathbf{v}$, and temperature when applying Hardy's expressions. The systems they are concerned with are quasi-static, where material velocity, $\mathbf{v}$, should be equal to zero. Problems arise when the characteristic volume is chosen to be too small for the atomic velocities within the volume to be de-correlated, so $\mathbf{v}$ ($=\frac{\sum_{\alpha=1}^{N} m_\alpha \mathbf{v}_\alpha \psi(\mathbf{x}_\alpha-\mathbf{x})}{\sum_{\alpha=1}^{N} m_\alpha \psi(\mathbf{x}_\alpha-\mathbf{x})}$) computed by Hardy's definition is not zero as it should be. This can lead to an erroneous value of relative atomic velocity, $\tilde{\mathbf{v}}_\alpha$, ($=\mathbf{v}_\alpha - \mathbf{v}$) within the volume, as is the temperature of the spatial point. In the work of Webb III et al., this problem was tackled by conducting time averaging on $\mathbf{v}$, which can lead to $\mathbf{v}$ that is very close to zero. However, the wave propagation problem shown in Fig. 4.5 is a dynamic process, where $\tilde{\mathbf{v}}_\alpha$ is supposed to be

zero. At the wave front where atomic velocities change drastically, only when the characteristic volume is so small that it contains only one atom, the computed $\tilde{\mathbf{v}}_\alpha$ can be zero**.** Larger characteristic volume that contains more than one atom will lead to material velocity which is an average of the velocities of atoms at the wave front. This gives nonzero $\tilde{\mathrm{v}}_\alpha$ for the atoms within the volume and thus nonzero temperature. The material velocity, **v**, at the spatial point can change with different characteristic volume as is $\tilde{\mathbf{v}}_\alpha$ for the atom within the volume. This explains why heat flux profile changes with varying characteristic volume.

Next, we investigate the validity of Hardy's theory through several numerical tests. Figure 4.6 shows the conservation equations as the Gaussian pulse propagates in the harmonic chain at an initial 0 K. Two time instants are chosen and good fit between two sides of the balance laws are observed. The positions of the wave fronts can be clearly identified. At 300 K, validity of Hardy's formulas is tested in a similar fashion for the Gaussian pulse in the harmonic chain at time instant t=3 ps. In Fig. 4.7(a) thermomechanical quantities are computed from a randomly chosen realization and in Fig. 4.7(b) ensemble averaged values over the 500 realizations of the themomechanical quantities are employed. The validity of Hardy's formulas can be established in both cases. The profiles of the balance laws after ensemble averaging at 300 K resemble those at 0 K. In comparison, the profiles of the balance laws before ensemble averaging are affected by the fluctuating thermomechanical quantities and thus are much noisier compared to those after averaging.

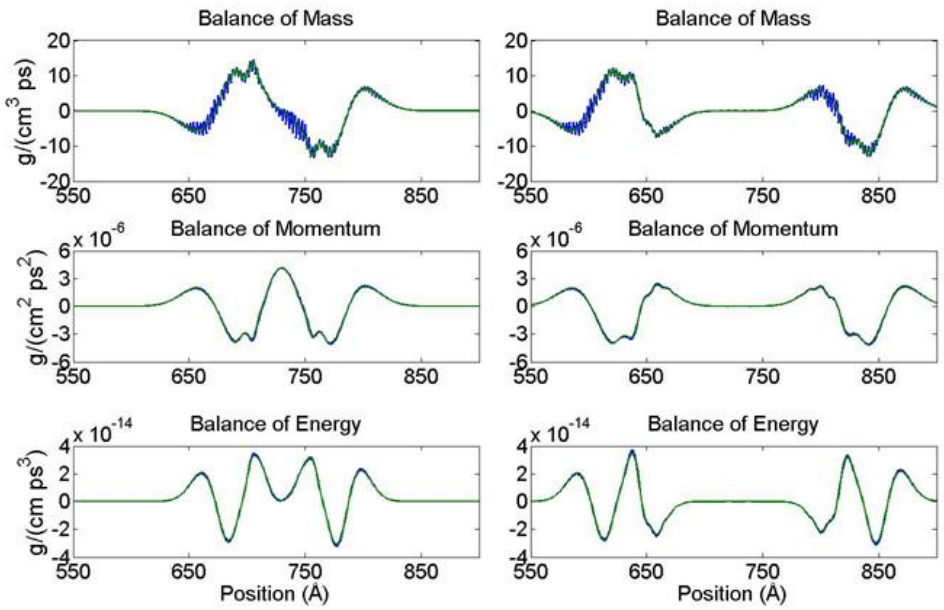

Figure 4.6 Comparison between two sides of the continuum governing equations as the Gaussian pulse propagates in the harmonic chain at initially 0 K at 1 ps (left column) and 3 ps (right column) [98]

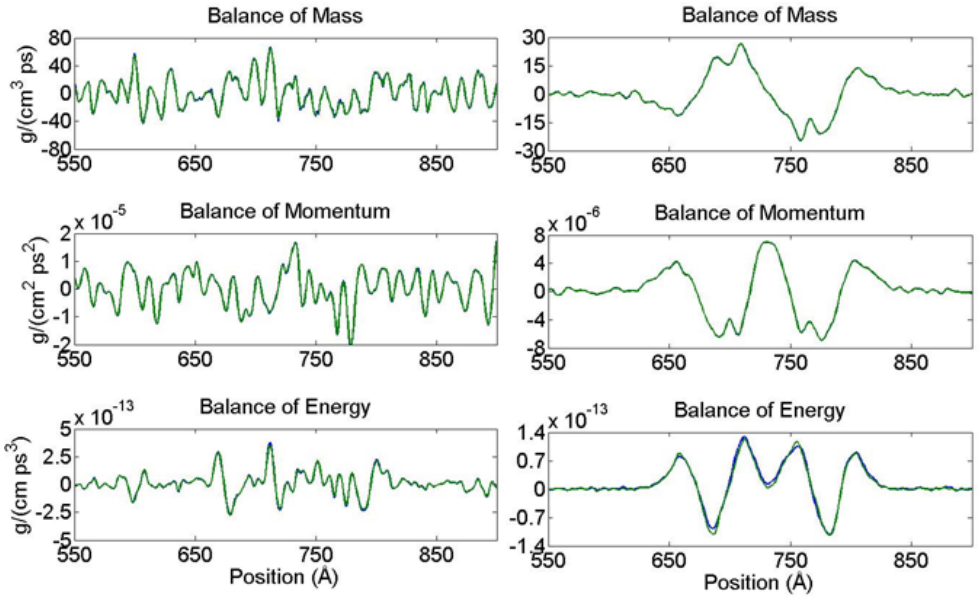

Figure 4.7 Comparison between two sides of the continuum governing equations before (left column) and after (right column) ensemble averaging as the Gaussian pulse propagates in the harmonic chain at 1 ps at around 300 K [98]

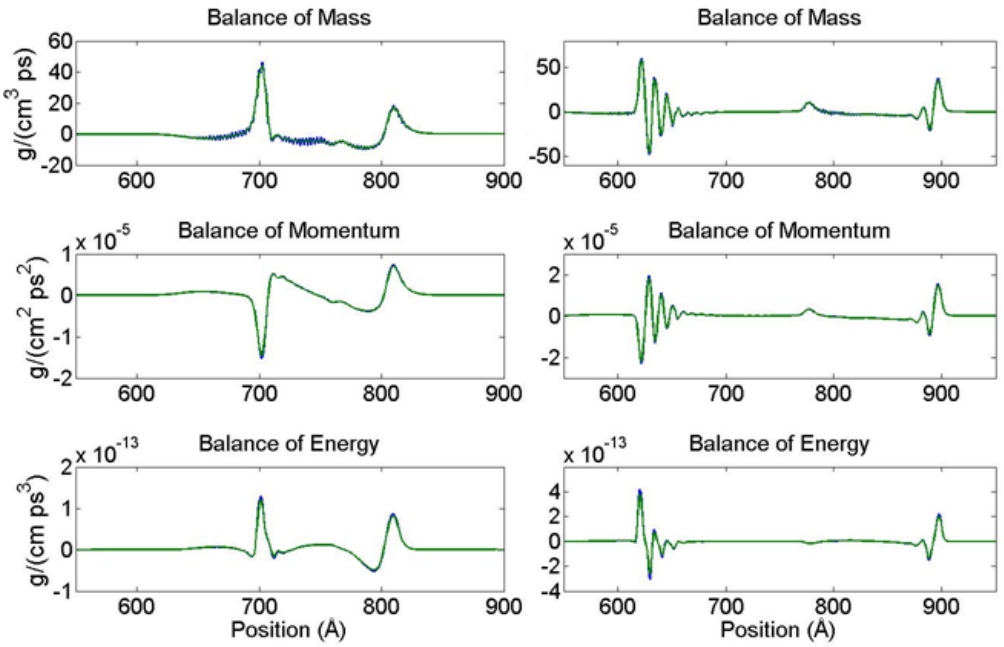

Figure 4.8 Comparison between two sides of the continuum governing equations as the Gaussian pulse propagates in the Morse chain at initially 0 K at 1 ps (left column) and 3 ps (right column) [98]

It should be mentioned that in the original theory developed by Hardy, conservation equations are obeyed without ensemble averaging, which has also been demonstrated here through numerical calculation. As shown in Chapter 3, expected values of thermomechanical quantities often cannot be reached for non-equilibrium systems without ensemble averaging. Therefore, conservation equations are obeyed when the thermomechanical quantities are away from their expected values in those cases. Hardy did not mention, however, whether the time averaging or ensemble averaging used, which is necessary to achieve the expectation values of the thermomechanical quantities, would affect the validity of the computed quantities. Apparently, the validity of ensemble averaged quantities cannot be justified by the result from individual realization because of the nonlinearity of the conservation equations. Numerical tests shown in Fig. 4.7(b) demonstrate the ensemble averaged thermomechanical quantities do obey conservation equations. Similar analysis has been performed on the Gaussian pulse propagation

in the Morse chain at 0 and 300 K (Figs. 4.8 and 4.9) and the shock wave propagation in the 1D Morse chain at 0 and 300 K (Figs. 4.9 and 4.10). Our results also show that the balance laws are obeyed in all these cases as well. The slight discrepancy in the balance of energy after ensemble averaging shown in Figs. 4.7(b), 4.9(b) and 4.11(b) is still not clearly known.

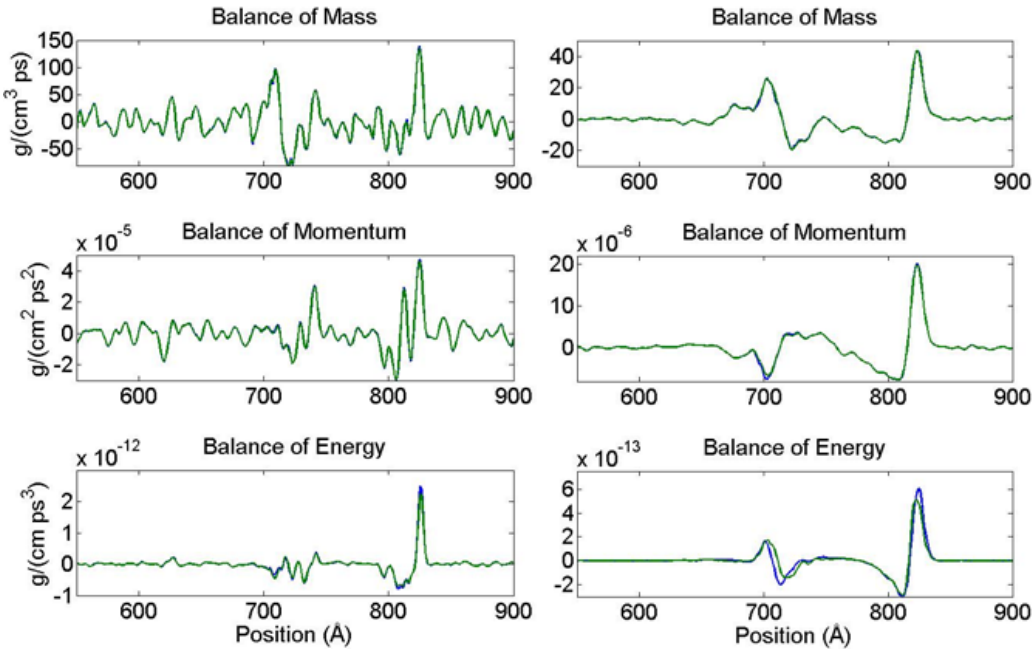

Figure 4.9 Comparison between two sides of the continuum governing equations before (left column) and after (right column) ensemble averaging as the Gaussian pulse propagates in the Morse chain at 1 ps at around 300 K [98]

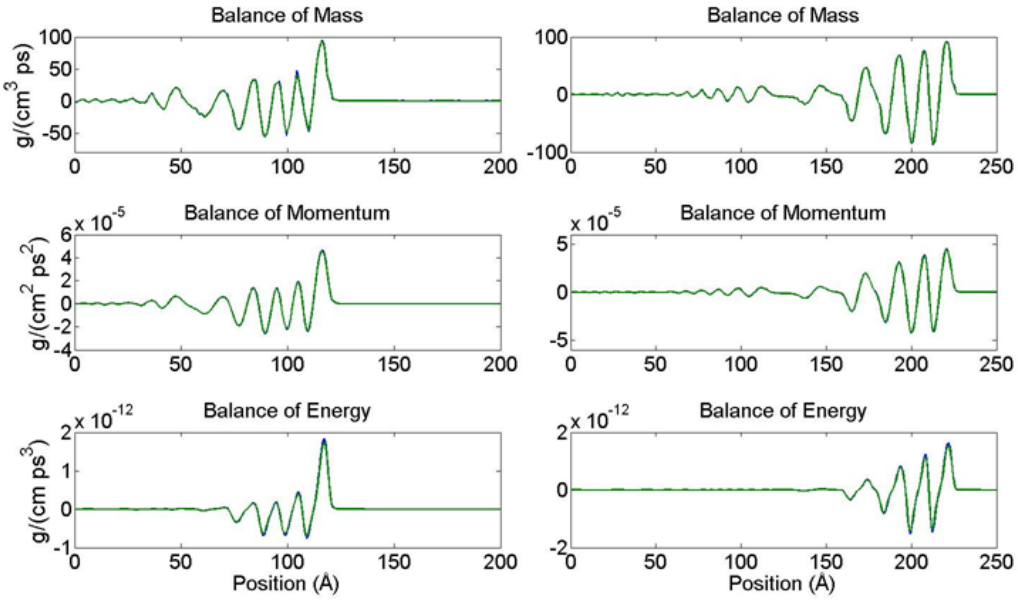

Figure 4.10 Comparison between two sides of the continuum governing equations as the shock wave propagates in the Morse chain at 2 ps (left column) and 4 ps (right column) at initially 0 K [98]

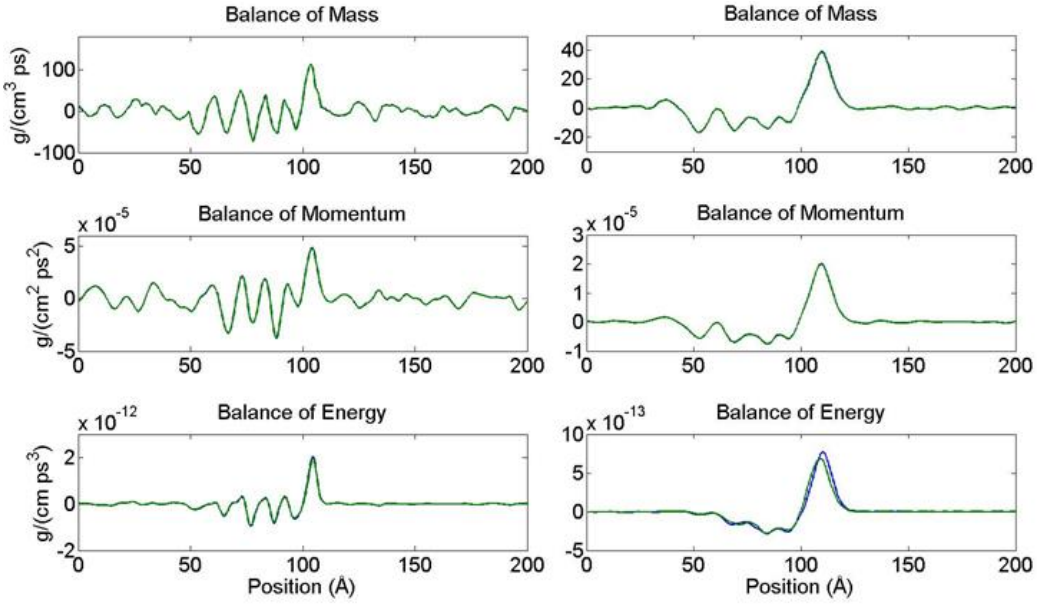

Figure 4.11 Comparison between two sides of the continuum governing equations before (left column) and after (right column) ensemble averaging as the shock wave propagates in the Morse chain at 2 ps at around 300 K [98]

During the process of testing the validity of Hardy's expressions by comparing two sides of the conservation equations, it is discovered that the localization function should be normalized depending on the spatial volume (V) and number of atoms (N) contained in the characteristic volume. The new normalization criterion is as follows:

$$\sum_{\alpha}^{N} \psi(\mathbf{x}_\alpha - \mathbf{x})\Delta V = 1 \tag{4.8}$$

where $\Delta V = N/V$, even though in theory the normalization criterion for the localization function given by Hardy is $\int \psi(\mathbf{x}_\alpha - \mathbf{x})\mathrm{d}\mathbf{x} = 1$. The original normalization criterion (see Ch. 2.4) is set to conserve the property for the entire system and the integration is over the entire system. However, to conserve local properties in the atomistic-to-continuum link in numerical calculation, $\sum_{\alpha}^{N} \psi(\mathbf{x}_\alpha - \mathbf{x})\Delta V = 1$ needs to be satisfied instead. Otherwise, significant discrepancies between the two sides of the balance laws can appear for both 1D and 3D problems. Figure 4.12 shows the comparison between two sides of balance of momentum and energy by applying different normalization criteria for the Gaussian pulse propagation in the Morse chain at 0 K. The left column of Fig. 4.12 shows the balance laws of momentum and energy by using $\int \psi(\mathbf{x}_\alpha - \mathbf{x})\mathrm{d}\mathbf{x} = 1$. Clear discrepancy between the LHS and RHS of the balance law of energy can be observed. The right column of Fig. 4.12 shows the corresponding results by applying $\sum_{\alpha}^{N} \psi(\mathbf{x}_\alpha - \mathbf{x})\Delta V = 1$, where the discrepancy in the balance law of energy has been eliminated. It is still not clear why the balance of momentum is not affected by the normalization rules as balance of energy. Though rigorous derivation for the normalization criteria cannot be given here, one can view this normalization criterion as the discrete version of the original normalization criterion $\int \psi(\mathbf{x}_\alpha - \mathbf{x})\mathrm{d}\mathbf{x} = 1$. This new normalization criterion has been employed in all the validation tests.

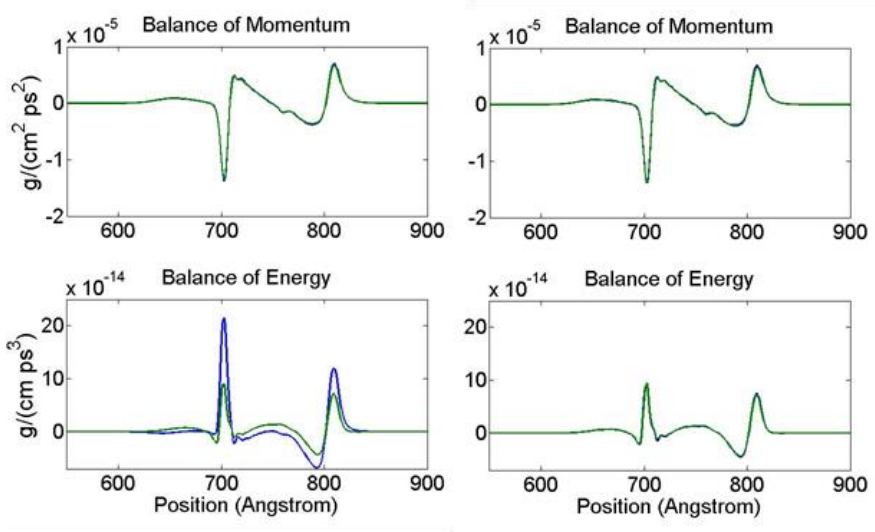

Figure 4.12 Demonstration of the different normalization rules on the conservation of momentum and energy as the Gaussian wave propagates in the Morse chain at 1 ps at initially 0 K. Left column is to use the original normalization rule and right column is to use the new normalization rule [98]

Finally, validity of Hardy's formulas as the Gaussian pulse propagates in the 3D Au and Ni crystals as well as shock impact response in the 3D Ni are demonstrated in Figs. 4.13-4.16. The 3D tests are conducted for systems initially at 0 K as well as 300 K. Figures 4.13 and 4.14 show Gaussian pulses propagation in the 3D Au and Ni crystals at an initial 0 K. Figures 4.15 and 4.16 shows shock wave propagation in the Ni crystal at an initial 0 K and 300 K. Good agreement between the two sides of the balance laws can be observed in all cases though they do not fit as well as the 1D examples. This can be ascribed to the more complex calculations and multiple terms involved in computing the differential conservation equations. It is worth mentioning that there are large discrepancies between the two sides of balance of energy if the thermomechanical quantities have not been not computed based on the new normalization criterion.

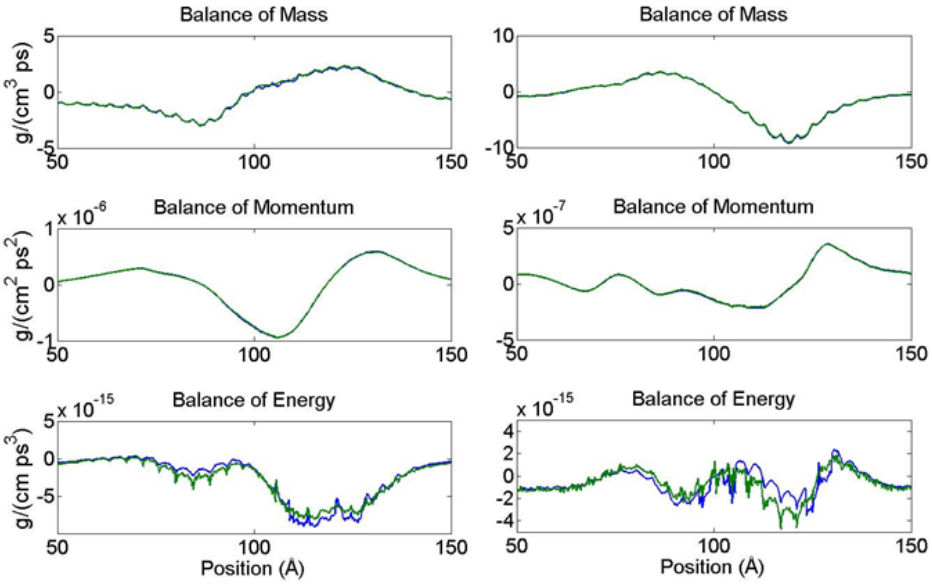

Figure 4.13 Comparison between two sides of the continuum governing equations as the Gaussian wave propagates in the 3D gold crystal modeled by Morse potential at 1 ps (left column) and 2 ps (right column) at initially 0 K [98]

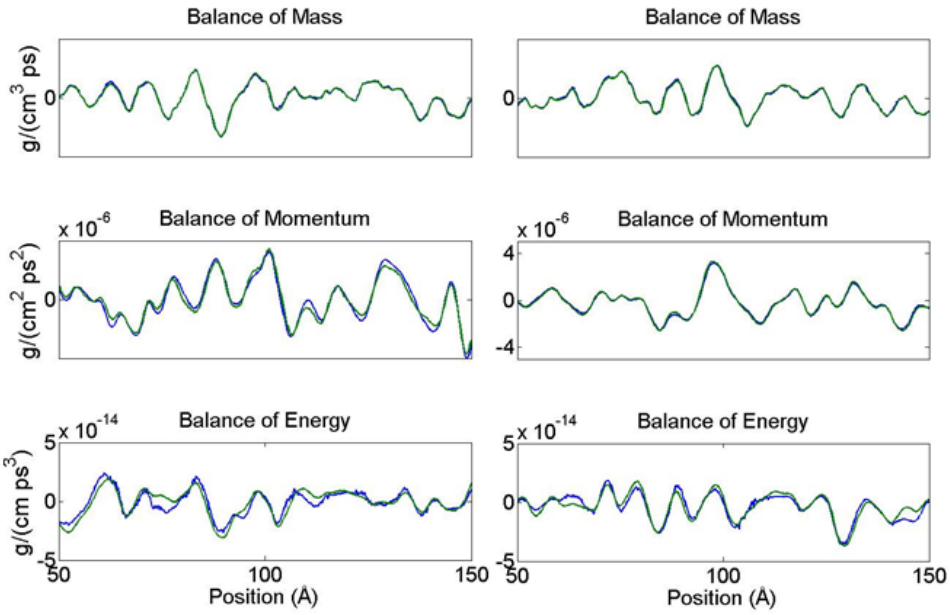

Figure 4.14 Comparison between two sides of the continuum governing equations as the Gaussian wave propagates in the 3D nickel crystal modeled by EAM potential at 1 ps (left column) and 2 ps (right column) at initially 0 K [98]

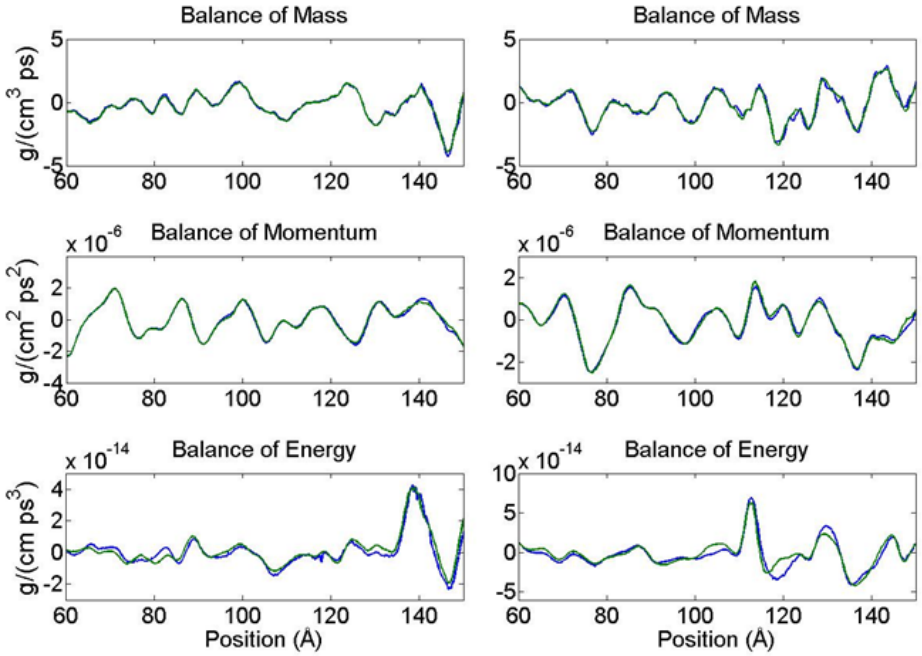

Figure 4.15 Comparison between two sides of the continuum governing equations as the shock wave propagates in the 3D nickel crystal modeled by EAM potential at 1 ps (left column) and 3 ps (right column) at initially 0 K [98]

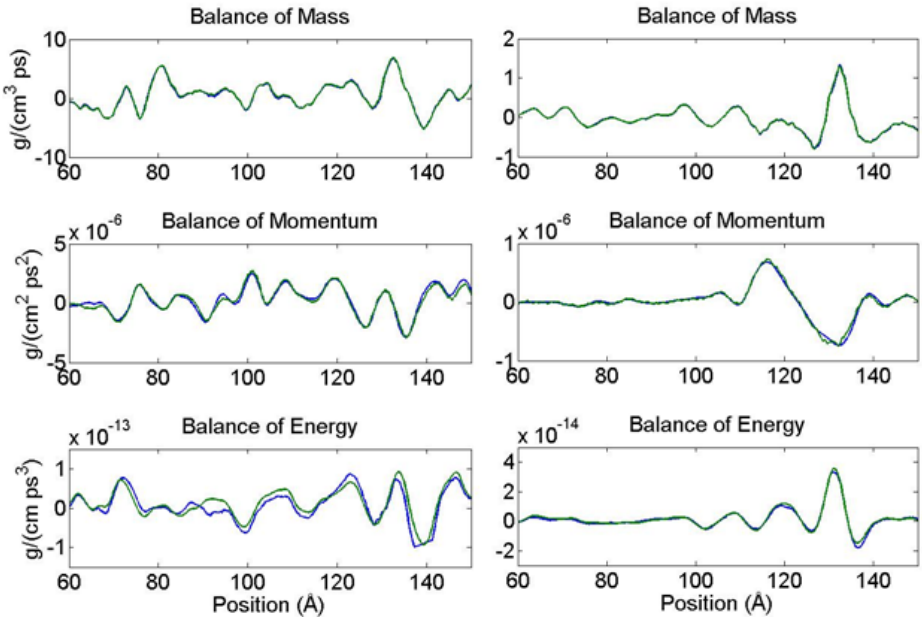

Figure 4.16 Comparison between two sides of the continuum governing equations as the shock wave propagates in the 3D nickel crystal modeled by EAM potential at 2 ps at around 300 K before (left column) and after (right column) ensemble averaging [98]

4.4 CONCLUSIONS

In this Chapter, Hardy's thermomechanical quantities are validated by testing if they obey continuum governing equations including balance laws of mass, momentum, and energy for a series of non-equilibrium processes. These non-equilibrium processes involve Gaussian pulse and shock wave propagating in 1D chains and 3D crystals, for which the atomic interactions are described by harmonic, Morse and EAM potential in different situations. The following conclusions can be drawn:

1. The validity of Hardy's expressions for non-equilibrium processes has been demonstrated by the good agreement between two sides of the balance laws, regardless of the size of the characteristic volume, the interatomic potential and crystal structure.
2. At a finite temperature, the ensemble averaged Hardy's thermomechanical quantities also obey conservation equations, although slight discrepancies in the balance of energy have been observed.
3. A modification to the localization function normalization criterion has been proposed and discussed in order to better conserve mass, momentum and energy, which is especially important for the validity of the balance law of energy.

5.0 APPLICATION OF HARDY'S FORMULAS TO ANALYZE CRACK PROPAGATION IN AN IRON CRYSTAL

In Chapter 4, a few highly non-equilibrium processes have been simulated and Hardy's theory has been verified for such processes through the conservation equations. However, it is still uncertain if Hardy's thermomechanical quantities would break down when more complex deformation mechanisms exist such as dislocation glide, slip band, and twinning. As such, MD simulation is conducted to investigate crack propagation in bcc iron (Fe) crystal under tensile and shearing loading and stress fields are constructed around the defective crack tip region using the many-realization approach. To justify the applicability of Hardy's formulas, the comparison between two sides of continuum conservation equations using Hardy's thermomechanical quantities are conducted around the crack tip region where slip bands and other defects exist.

5.1 SIMULATIONS

An iron crystal with dimensions L_x =40[110], L_y=40[001], and L_z=6[$1\bar{1}0$] in the *x*, *y*, and *z* directions is created, containing a center crack of five unit cells wide in the center (Fig. 5.1). The crack is created by excluding interactions between atoms above the center-plane of the Fe crystal

and atoms below the center plane. The crack plane lies parallel to the (001) plane (normal to *y*-axis) and the crack propagation direction coincides with the *x*-axis. Therefore, the crack propagation system is $(001)[110]$. Periodic boundary conditions are used in the *x* and *z* directions while a free boundary condition is used in the *y* direction. Due to the periodic boundary conditions in the *z* direction, this corresponds to a quasi-two-dimensional pre-crack.

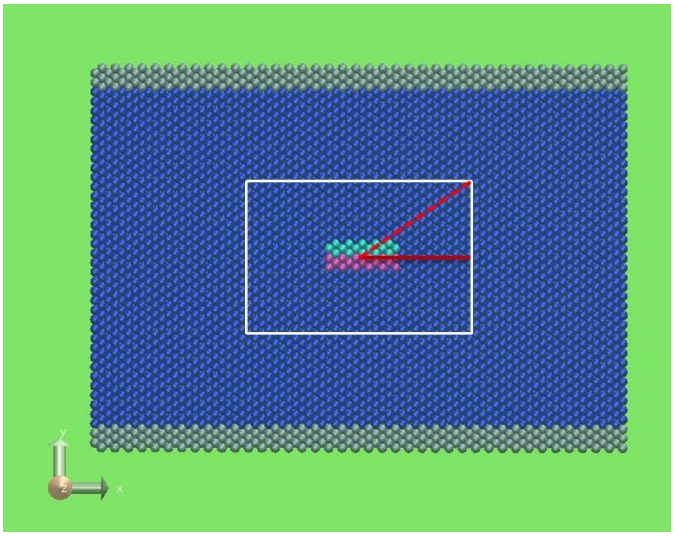

Figure 5.1 Configuration of the Fe crystal with pre-created center crack submitted to either tensile or shearing straining

The iron crystal under tensile and shear loading is studied using Hardy's theory. In the tensile case, the atoms within two unit cells of the system's upper and lower boundaries are displaced to the positive and negative *y* directions, respectively, to create a constant strain rate of 5E-3 ps^{-1}. Tensile stretching is applied to the system after energy minimization. In the case of a finite temperature, 500 realizations are conducted by assigning different velocities to the atoms and then the realizations are left to equilibrate at around 300 K before the tensile strain is applied. Similarly, in the shearing case, a shear strain rate of 5E-3 ps^{-1} is created by displacing

identical groups of atoms at the boundaries to positive and negative *x* directions. The interaction among Fe atoms are described by embedded-atom method (EAM) potentials.

5.2 STRESS ANALYSIS USING HARDY'S EXPRESSIONS

Hardy's stress expression has been utilized to compute stress distribution around the core of an edge dislocation in an elastic medium simulated by an EAM model [79]. In that study, the stresses are computed after conjugate gradient energy minimization. The characteristic volume is chosen to be a cylindrical analysis volume element and stress fields computed with various cylinder radius were compared. Peculiar oscillations appear in the computed stress fields when the radius is chosen to be smaller or comparable to the lattice constant and the stress fields vary smoothly and are consistent with what is expected from the local elasticity theory when the radius is around 1.7 times the lattice constant. Even though a larger volume element tends to yield better convergence, the spatial volume radius is often chosen to be comparable to the cut-off distance of the potential for the sake of spatial resolution. Hardy's stress formulation has also been employed to construct the stress fields of a center-cracked body after conjugate gradient minimization. The spatial characteristic volumes consisting of rectangular parallelepipeds and the localization functions are multiples of three linear shape functions, one for each orthogonal direction as in the finite element method. The constructed fields are consistent with expectations from fracture mechanics: concentrations of tensile stress near the crack tips and zero stress in the crack opening region. It is noted that these simulations are all conducted at temperatures close to 0 K.

At finite temperature, Hardy's expressions have been used to calculate local density, temperature, and velocity from the results of MD simulations of shock waves in a two-dimensional model system [77]. The width of the localization function is varied to optimize the resolution of the turbulence behind the shock front. When choosing a value for the width, it was found that a balance must be made between masking interesting phenomena by excessive fluctuations with small width and over-smoothing the fields with large width.

In our study, stress is computed at the nodes of a 25×15×1 grid bound by the white rectangle shown in Fig. 5.1 and the grid is used to construct the contour plot. The characteristic volume is chosen to be a sphere centered at the spatial point of interest having diameter 1.5 times the lattice constant of the Fe crystal. The localization function employed is the same as that used for 3D problem in Chapter 4 (Eq. 4.7b). The new normalization rule, $\sum_{\alpha}^{N} \psi(\mathbf{x}_{\alpha} - \mathbf{x})\Delta V = 1$, is applied in this Chapter as well (N is the total number of atoms within the characteristic volume, V, and ΔV is the volume per atom). The width of the localization function is chosen as 1.5 times the lattice constant. Instead of removing noise by enlarging window size in spatial averaging, the ensemble average used here can preserve the spatial resolution as well as achieve satisfactory accuracy.

5.3 VALIDATION PROCEDURE

Along the horizontal and diagonal lines drawn in Fig. 5.1 (colored in red), the validity of Hardy's theory is tested by comparing two sides of the conservation equations using the thermomechanical quantities computed with Hardy's formulas. At finite temperature, comparisons between two sides of the balance laws are conducted using the quantities computed

from a randomly chosen realization and after ensemble averaging over 500 realizations. In Chapter 4, the discrete version of the balance laws (Eq. 4.2) is given but balance of momentum is only given in the *y* direction along which the Gaussian wave and shock wave propagate and the thermomechanical quantities vary most drastically. In this Chapter, balance of momentum is not only tested in the *y* direction but also in the *x* direction. The balance of momentum in the *x* direction (Eq. 5.1) is only slightly different from that in the *y* direction (see Eq. 4.2b):

$$\rho \frac{{v_x}^{(j+1)} - {v_x}^{(j)}}{\delta t} + \rho \left\{ \frac{{v_x}^{(i+1)} - {v_x}^{(i)}}{\delta x} v_x + \frac{{v_x}^{(k+1)} - {v_x}^{(k)}}{\delta y} v_y + \frac{{v_x}^{(m+1)} - {v_x}^{(m)}}{\delta z} v_z \right\} = \frac{{\sigma_{xx}}^{(i+1)} - {\sigma_{xx}}^{(i)}}{\delta x} + \frac{{\sigma_{xy}}^{(k+1)} - {\sigma_{xy}}^{(k)}}{\delta y} + \frac{{\sigma_{xz}}^{(m+1)} - {\sigma_{xz}}^{(m)}}{\delta z} \tag{5.1}$$

Along the horizontal line, only balance of momentum in the *x* direction is tested. Central finite difference is used for the spatial derivative in this direction and the forward finite difference is used for the spatial derivative in the other directions as well as for the time derivative. Along the diagonal line, the balance of momentum in both the *x* and *y* directions are tested but only that for the *x* direction is demonstrated. Forward finite difference is used for the spatial derivative in all directions and time derivative. δt is chosen to be the simulation time step size, 1 fs, δx≈0.3 Å, δy≈0.3 Å and δz ≈0.2 Å. The spatial discretization is also chosen by reducing it until there is no obvious change in the two sides of the balance laws. Note that the origin of the coordinate system is located at the center of the pre-created crack. The conservation equations along the horizontal direction are plotted against the *x* coordinates of spatial points, and those along the diagonal direction are plotted against the *y* coordinates of spatial points.

5.4 RESULTS AND DISCUSSIONS

Several snapshots during the crack initiation and propagation under tensile straining at 0 K are shown Fig. 5.2. Straining below a threshold strain value does not result in any significant structural modifications or crack propagation at the pre-crack tips (Fig. 5.2a and 5.2b). For the crack system $(001)[110]$ which is employed in our investigation, the emission of slip bands from the pre-crack tips can only be observed when strain is above a critical value, and its range is reported to be usually around 6%-8% [35] but this depends on the pre-crack size, orientation, simulation cell size and shape. In our investigation, the slip band emission can be clearly observed at a strain of 6% (Fig. 5.2d) though atomic reconfiguration around the crack tip can already be seen at a strain of 4.5% (Fig. 5.2c). These slip bands emitting from the moving crack tip progressively shift together with the tip without significant change of the slip band thickness. Slip band emission from either atomistically sharp or slightly blunt pre-crack tip has been observed for a crack front oriented along the $\langle 110 \rangle$ direction for an Fe crystal modeled with different EAM potentials [40, 99-103]. In spite of the continuous slip band sliding together with the crack tip during the crack propagation, the crack faces remain flat and quite smooth, so that the appearance of the fracture surface resembles that expected for an ideal brittle cleavage, except for obvious blunt crack tips at a later stage of the cracking. The cracks should be able to propagate from either (or both) end of the central pre-crack. The slip band behavior at opposite crack tips is completely uncorrelated. At each crack tip two equivalent slip systems are available for the crack front orientation and hence either one or two slip bands per tip can form. The slip band emission in single-band or fork-shape geometry is partially determined by the pre-crack tip shape and is partially a matter of chance. In our simulation setup, slip bands are prone to form in

the upper half of the Fe crystal because of the slight asymmetry of the atomic configuration at the two surfaces of the crack tip (Fig. 5.2d).

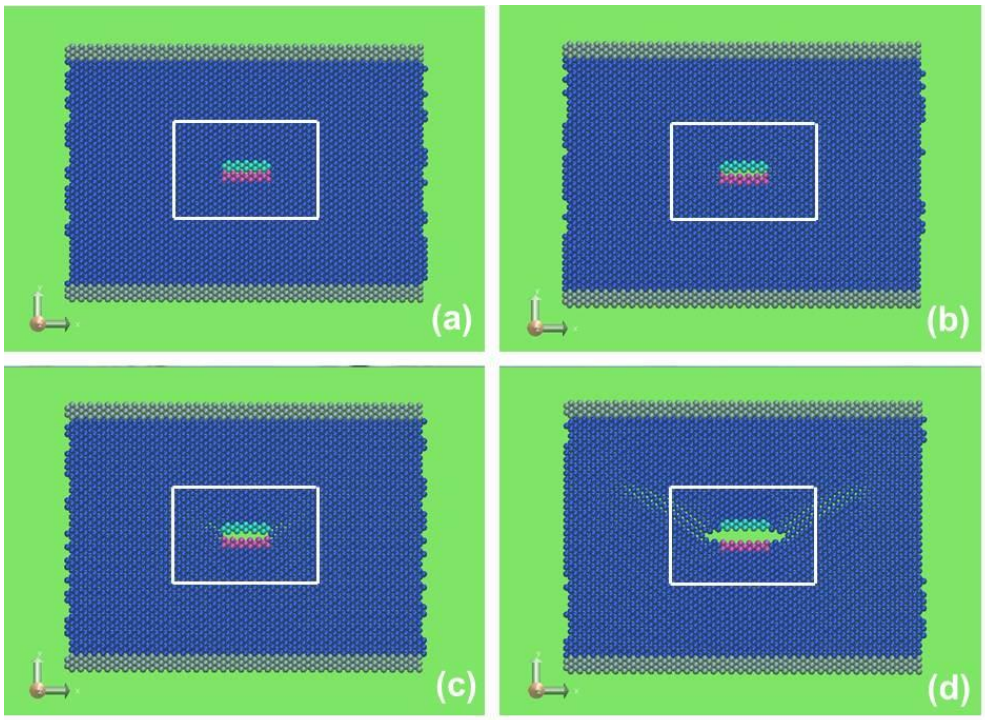

Figure 5.2 Snapshots of Fe crystal with a center crack tensile strained to (a) 1.5% (b) 3% (c) 4.5% and (d) 6% at initially 0 K

Stress contour plots constructed using Hardy's expressions at different time instants as the crack propagates under tensile loading at 0 K are shown in Figs. 5.3 and 5.4. σ_{xx} and σ_{yy} presented here have been compared with the linear elastic solution of an infinite plate having a center crack and applied with far field tensile stress. The stress fields in Figs. 5.3b and 5.4b around the crack tips resemble the linear elastic solutions, qualitatively. To better understand the mechanical response of the Fe crystal to tensile loading, maximum principal stress and maximum shear stress are plotted in Figs. 5.5 and 5.6. The material experiences different stages of deformation under tensile straining:

Stage I: At the strain level of 1.5%, no crack opening can be observed and the surface stress at the two surfaces of the crack is still high (Figs. 5.5a and 5.6a). Tensile stress around the crack tips starts to increase and extend towards the diagonal directions in front of crack tips. In between the high tensile stress regions, the areas away from the crack surfaces are under compression.

Stage II: As the strain level increases to 3%, the crack starts to open. The surface tensile stress on the crack surfaces has decreased due to crack opening while tensile stress concentration at the crack tips becomes obvious. The high tensile stress regions have extended out further in the diagonal directions ahead of the crack tips. Shear stress concentration cannot be observed at the crack tips but can be seen in front of tips at a certain angle from the crack surfaces. In fact, the highest shear stress region seems to overlap with a part of the highest tensile stress region (Figs. 5.5b and 5.6b). Although slip bands have not emitted at this strain level, the highest shear stress region may prepare for the initiation of slip bands.

Stage III: Slip bands start to emit from the crack tips as strain level increases to 4.5% and the crack opening can be more clearly seen. The tensile stress concentration at the tips is now released by the slip band emission while both tensile and shear stresses have shifted and concentrated at where the slip bands terminate. The stress plots become obviously asymmetric from this strain level as slip bands only emit in the upper half of the Fe crystal (Figs. 5.5c and 5.6c).

Stage IV: At a strain level of 6%, slip bands can be clearly observed, which have evolved and now terminate out of the range of the contour plot. Tensile and shear stress becomes concentrated again at the propagating crack tips. High tensile and shear stress also extends towards the slip band directions. As mentioned above, the crack propagation is accompanied by

the shifted slip bands at the crack tips. The high tensile and stress probably is the driving force for the movement of slips bands and crack tips (Figs. 5.5d and 5.6d).

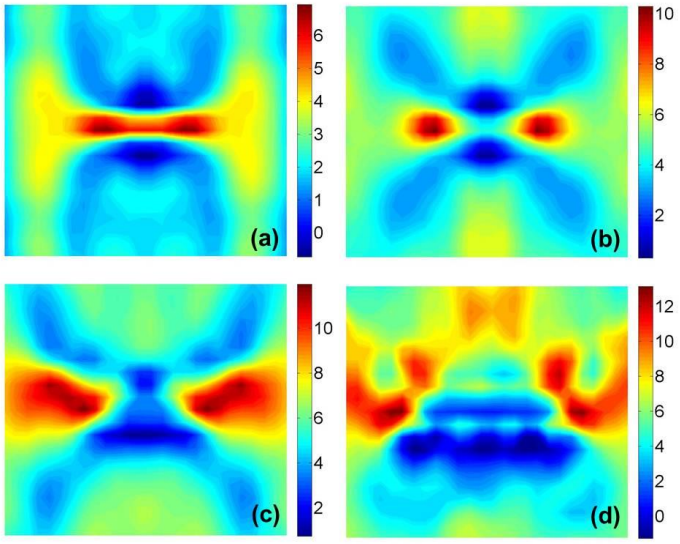

Figure 5.3 σ_{xx} of the center-cracked Fe crystal tensile shear strained to (a) 1.5% (b) 3% (c) 4.5% and (d) 6% at initially 0 K (stress has the unit of GPa)

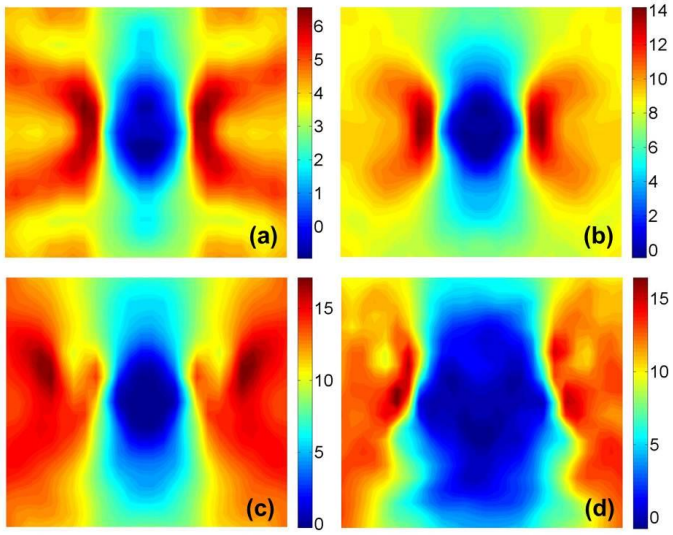

Figure 5.4 σ_{yy} of the center-cracked Fe crystal tensile strained to (a) 1.5% (b) 3% (c) 4.5% and (d) 6% at initially 0 K (stress has the unit of GPa)

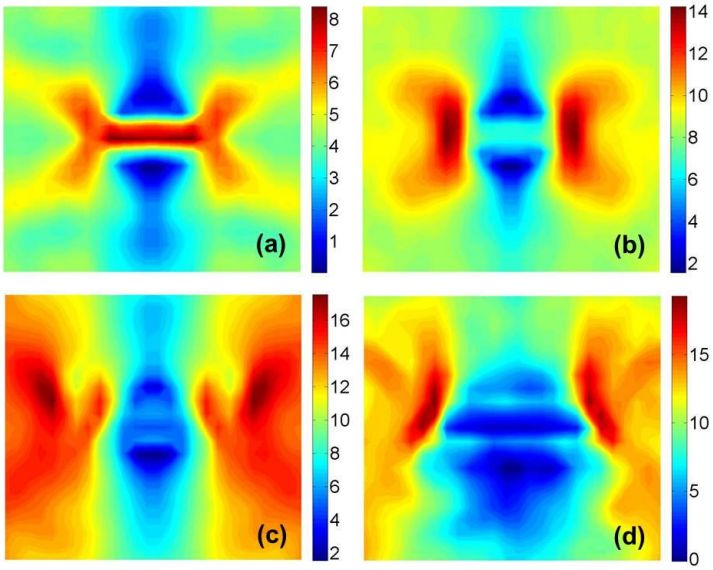

Figure 5.5 Maximum principal stress of the center-cracked Fe crystal tensile strained to (a) 1.5% (b) 3% (c) 4.5% and (d) 6% at initially 0 K (stress has the unit of GPa)

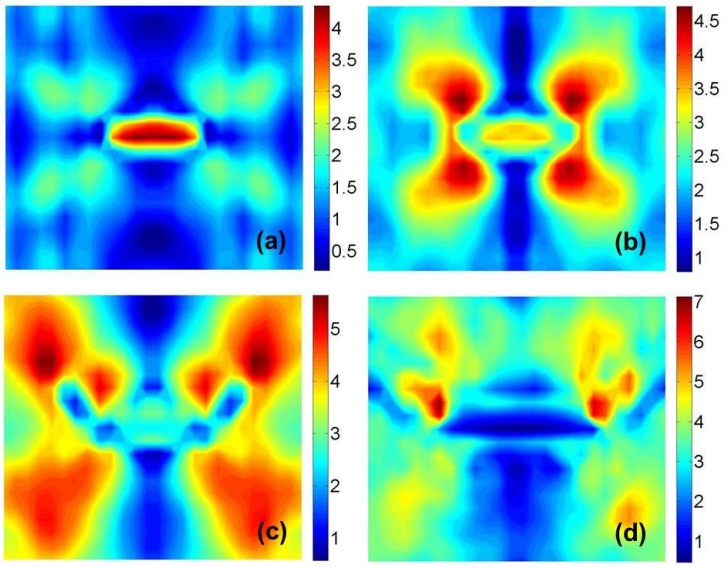

Figure 5.6 Maximum shear stress of the center-cracked Fe crystal tensile strained to (a) 1.5% (b) 3% (c) 4.5% and (d) 6% at initially 0 K (stress has the unit of GPa)

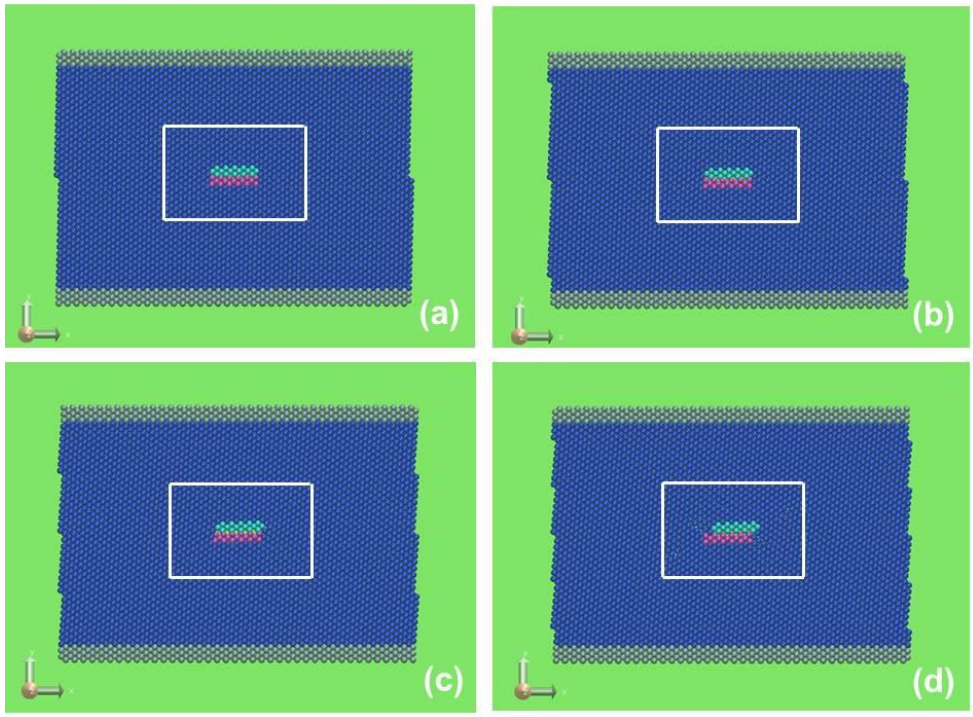

Figure 5.7 Snapshots of Fe crystal with a center crack shear strained to (a) 1.5% (b) 3% (c) 4.5% and (d) 6% at initially 0 K

Snapshots of the Fe crystal under shear straining are shown Fig. 5.7. No crack opening or propagation can be clearly observed under shear loading. Up to the strain level of 4.5%, no dislocation emission from the crack tips can be observed and the crystal is in the elastic deformation regime. The atoms move collectively to adjust to the applied shear strain. The upper and lower half of the crystal shift towards opposite directions through emission of dislocations from the pre-crack tips at a later stage, which can be seen in Fig. 5.7d. Stress contour plots for σ_{xx} and σ_{xy} are given in Figs. 5.8 and 5.9, and have been compared with linear elastic solution of an infinite plate having a center crack and applied with far field shear stress. Around the crack tips, good qualitative agreement can be found between our results and the predictions from linear elastic solutions. Maximum principal stress and shear stress of the center-cracked Fe crystal under shear loading are plotted in Figs. 5.10 and 5.11. Maximum principal stress contour plots generally resemble the contour plot of σ_{xx} (Fig. 5.8) and maximum shear stress contour plot resembles the contour plot of σ_{xy} (Fig. 5.9), indicating that the other stress components are quite low. Combining the atomistic snapshots and maximum principal as well as shear stress, the mechanical response of the Fe crystal under shear loading can be better analyzed:

Stage I: Up to the strain level of 4.5%, the Fe crystal is still in the elastic deformation regime. Atoms are moving collectively without obvious shift of two surfaces of the crack. The crack surface stress is obvious at the strain of 1.5% and is largely reduced at a strain of 3%. Stress at the crack tips then starts to increase until the strain reaches 4.5%. Areas above and below the crack surfaces have lower stress values than those ahead of the crack tips (Figs. 5.10a-c and Figs. 5.11a-c).

Stage II: Dislocations start to emit from the crack tips at a strain level of 6% and the two crack surfaces are shifted against each other via dislocation glide. The stress concentration at the crack tips is released and moves to areas where dislocations are located (Figs. 5.10d and 5.11d).

Stage III: At a later stage with large strain level (atomistic snapshots and contour plots are not shown here), part of the crystal surrounding the crack region has been observed to rotate through dislocation glide from the crack tips. Stacking faults and slip bands also form in other places of the crystal.

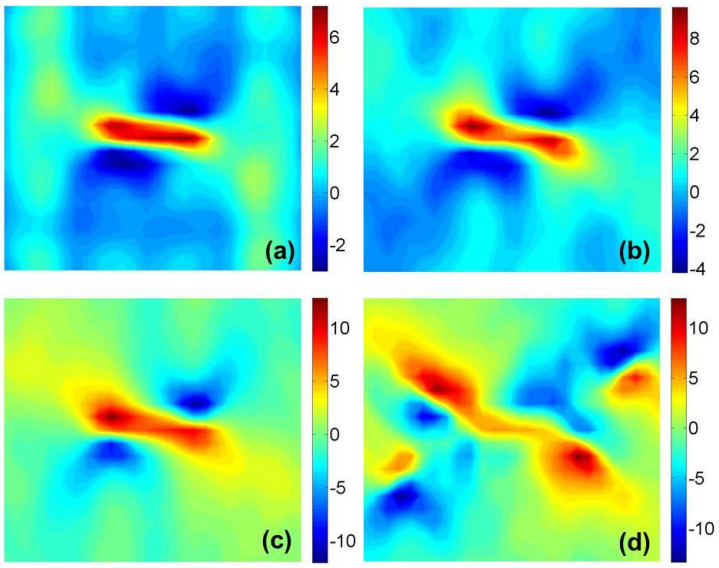

Figure 5.8 σ_{xx} of the center-cracked Fe crystal shear strained to (a) 1.5% (b) 3% (c) 4.5% and (d) 6% at initially 0 K (stress has the unit of GPa)

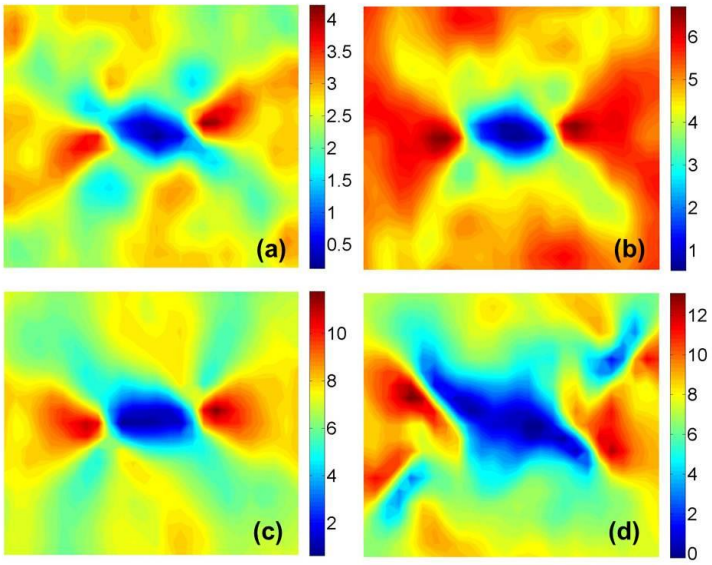

Figure 5.9 σ_{xy} of the center-cracked Fe crystal shear strained to (a) 1.5% (b) 3% (c) 4.5% and (d) 6% at initially 0 K (stress has the unit of GPa)

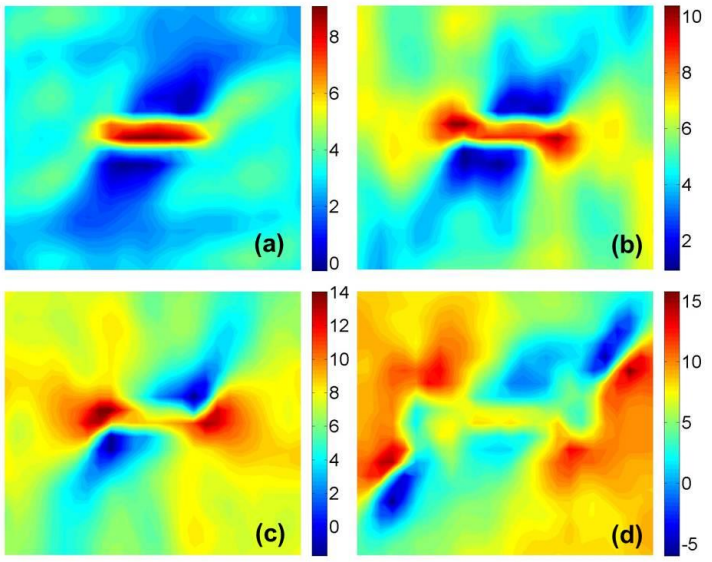

Figure 5.10 Maximum principal stress of the center-cracked Fe crystal shear strained to (a) 1.5% (b) 3% (c) 4.5% and (d) 6% at initially 0 K (stress has the unit of GPa)

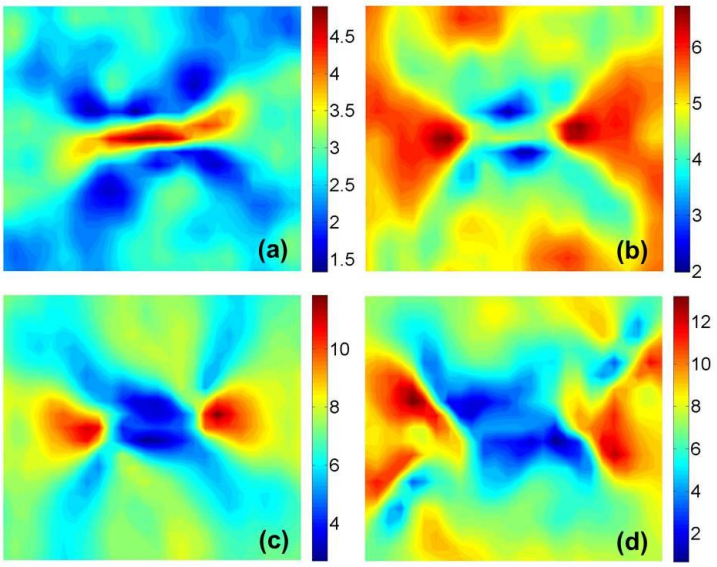

Figure 5.11 Maximum shear stress of the center-cracked Fe crystal shear strained to (a) 1.5% (b) 3% (c) 4.5% and (d) 6% at initially 0 K (stress has the unit of GPa)

The center-cracked Fe plate under tensile and shear loading has also been simulated using the XFEM (extended finite element method) [104, 105], which allows for simulating arbitrary crack growth without remeshing. To enable the comparison between the MD and Finite Element Analysis (FEA) results, the model is set to be proportional to the atomistic model simulated using MD, and consist of plane strain elements with free boundary conditions in the *x* and *y* directions. Displacement control is applied to the upper and lower boundaries of the crystal in the *y* direction. Since static analysis procedure is used in the XFEM, two kinds of displacement boundary controls are applied to enable the strain levels of 3% and 6%, respectively. Isotropic condition is used and the results would only be compared with the MD result qualitatively.

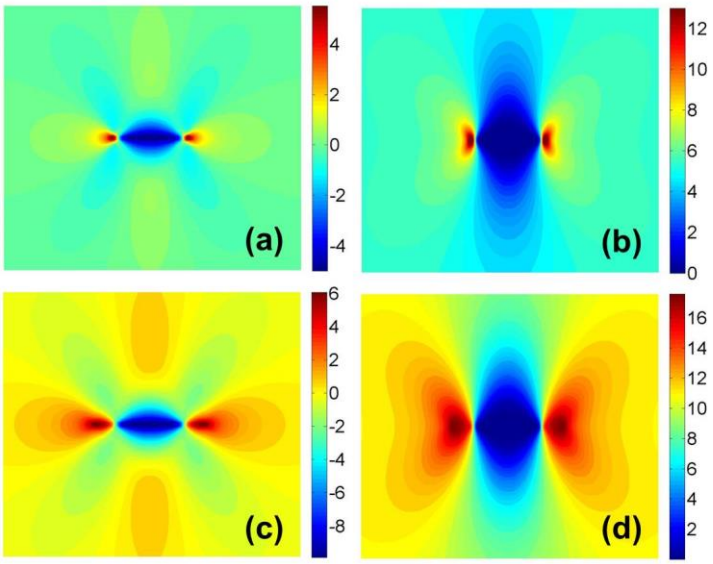

Figure 5.12 Stress distribution of the center-cracked Fe plate under tensile loading simulated in FEA: (a) σ_{xx} at the strain 3% (b) σ_{yy} at the strain 3% (c) σ_{xx} at the strain 6% and (d) σ_{yy} at the strain 6% (stress has the unit of GPa)

The materials properties such as Young's modulus, Poison's ratio, and plasticity have been obtained from MD simulations of an Fe bar under tensile loading with its crystal orientation the same as the center-cracked Fe crystal. Its dimensions has been set as L_x=10[110], L_y=50[001], and L_z=10[1$\bar{1}$0] under uniaxial tensile loading in the y direction, and as L_x =50[110], L_y=10[001], and L_z=10[1$\bar{1}$0] under uniaxial tensile loading in the x direction, respectively. The pressure of the whole simulation box is kept at zero in the transverse directions and increased in the tensile loading direction so that a tensile loading is applied and the material is gradually stretched. An averaged Young's modulus of 185 GPa is obtained through linear fitting of the true stress – true strain curves from the tensile loading in the two directions, and the Poison's ratio is 0.3365. Maximum principle stress beyond which the crack propagates is estimated to be the averaged maximum stress obtained from the uniaxial tensile loading in the two directions.

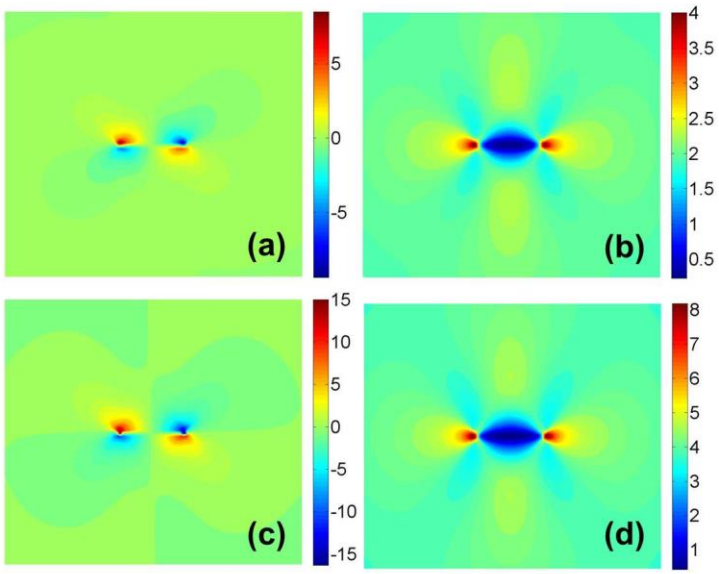

Figure 5.13 Stress distribution of the center-cracked Fe plate under shear loading simulated in FEA: (a) σ_{xx} at the strain 3% (b) σ_{xy} at the strain 3% (c) σ_{xx} at the strain 6% and (d) σ_{xy} at the strain 6% (stress has the unit of GPa)

The stress distributions for the iron plate under tensile and shear loading with the strain levels of 3% and 6% modeled are shown in Figs. 5.12 and 5.13. A comparison between the simulation results from MD and FEA (comparing 5.3b,d with 5.12a,c; 5.4b,d with 5.12b,d; 5.8b,d with 5.13a,c; 5.9b,d with 5.13b,d) shows that the stress distribution generally resembles each other qualitatively, especially at the strain level of 3%. The stress values are also within the similar ranges. At the strain level of 6% at which plastic deformation occurs, FEA is unable to simulate the dislocation emission at the crack tips. Therefore, unlike the MD results, the stress fields from FEA still demonstrate perfect symmetrical features though the crack has started propagating in the case of tensile loading. This can be seen from the shift of stress concentration at the crack tips. No crack propagation can be observed for the shear loading case.

The comparison between two sides of the conservation equations along the horizontal and diagonal directions for the Fe crystal under tensile loading at a strain of 3% and 6% is shown in Figs. 5.14 and 5.15, and that under shearing loading at a strain of 3% and 6% are shown in Figs.

5.16 and 5.17. The blue curves are computed from the LHS of the equations while the green curves are from the RHS. Note that the origin of the coordinate system coincides with the center of the pre-crack. The conservation equations along the horizontal direction are plotted against the *x* coordinates of spatial points, and those along the diagonal direction are plotted against the *y* coordinates of spatial points.

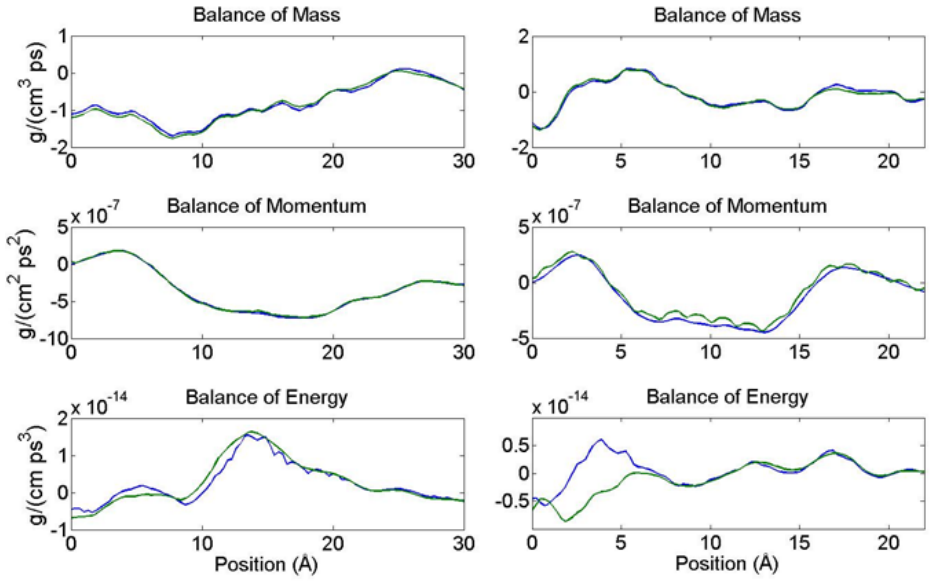

Figure 5.14 Comparison between two sides of the conservation equations in the horizontal (left column) and diagonal (right column) directions for the Fe crystal tensile strained to 3% at initially 0 K

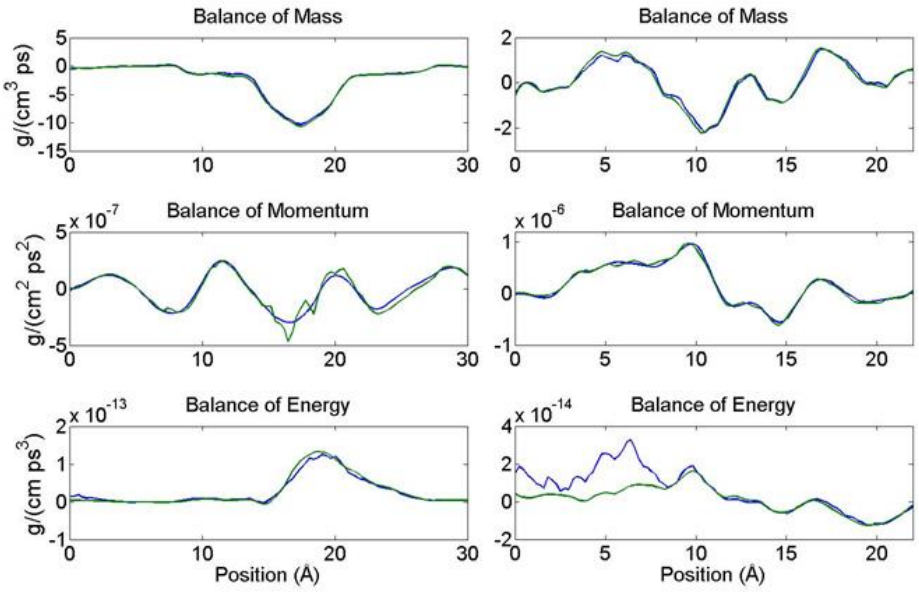

Figure 5.15 Comparison between two sides of the conservation equations in the horizontal (left column) and diagonal (right column) directions for the Fe crystal tensile strained to 6% at initially 0 K

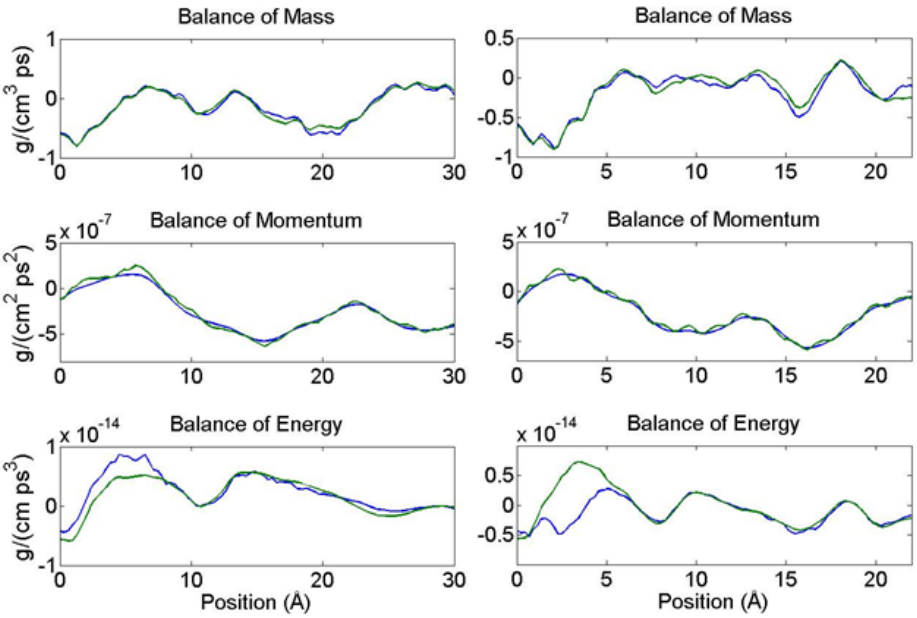

Figure 5.16 Comparison between two sides of the conservation equations in the horizontal (left column) and diagonal (right column) directions for the Fe crystal shear strained to 3% at initially 0 K

From the observation of the atomistic simulations in Figs. 5.2 and 5.7, no plastic deformation occurs at a strain level of 3% while slip bands or dislocations emit at the crack tips at a strain level of 6%. In both cases, mass and momentum are conserved as observed from the good agreement between the two sides of the equations, though there are some irregular bumps from the RHS of balance of momentum. However, significant discrepancies appear for balance of energy at the crack region (x coordinate ranges from -10.09 Å to 10.09 Å), which can be observed from the balance of energy along both the horizontal and diagonal directions though the discrepancy is more obvious in the diagonal direction. Since the imbalance of energy around the crack region occurs for Fe crystal under tensile loading when there is obvious cleavage and under shear loading when a crack opening cannot be observed, the discrepancies between two sides of the balance of energy should not be caused by the atomic configuration at the crack opening. It can also be observed that the balance of mass and momentum is still valid while the balance of energy fails at this region. The reason for this phenomenon is not totally clear at the present stage and requires more detailed studies.

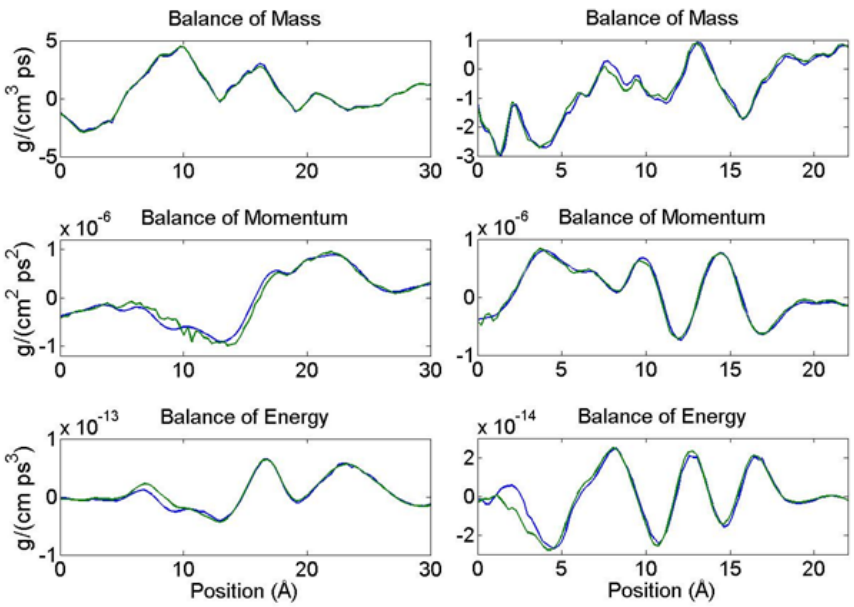

Figure 5.17 Comparison between two sides of the conservation equations in the horizontal (left column) and diagonal (right column) directions for the Fe crystal shear strained to 6% at initially 0 K

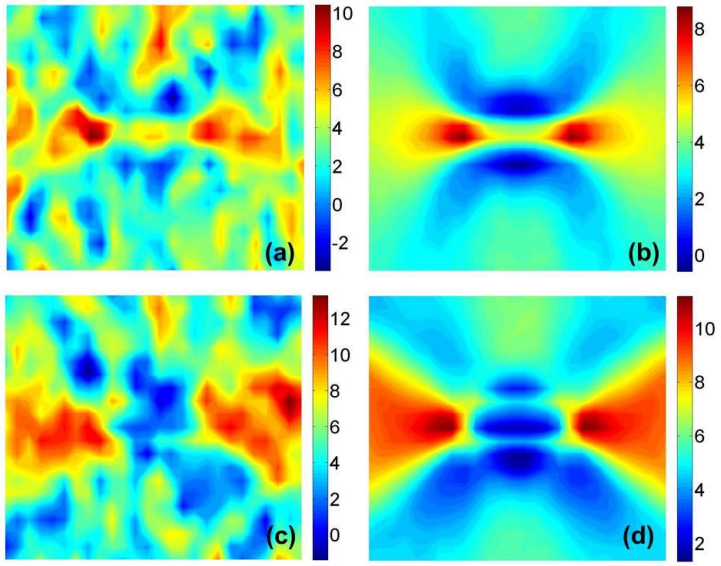

Figure 5.18 σ_{xx} for the center-cracked Fe crystal tensile strained to 3% (a) before and (b) after ensemble averaging, and to 6% (c) before and (d) after ensemble averaging at around 300 K (stress has the unit of GPa)

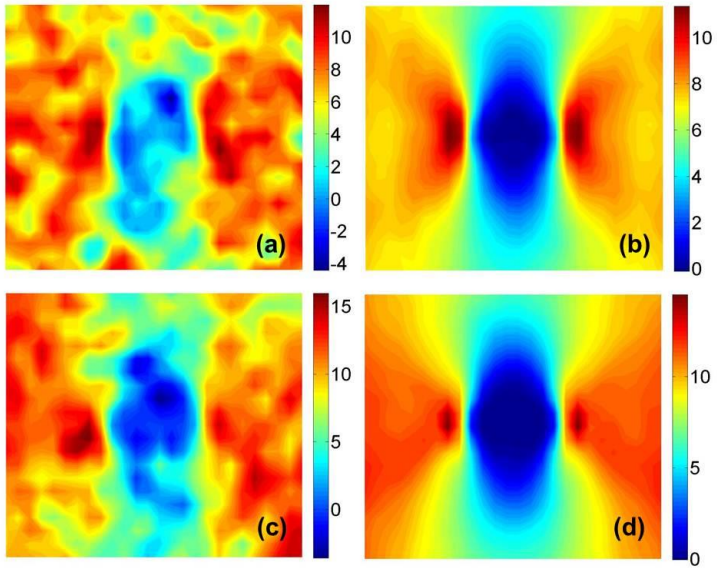

Figure 5.19 σ_{yy} for the center-cracked Fe crystal tensile strained to 3% (a) before and (b) after ensemble averaging, and to 6% (c) before and (d) after ensemble averaging at around 300 K (stress has the unit of GPa)

Similar simulations and analysis are also conducted for the crack systems at 300 K. Contour plots for the crystal under tensile loading before and after ensemble averaging are shown in Figs. 5.18 and 5.19, and those under shear loading before and after ensemble averaging are shown in Figs. 5.20 and 5.21. Comparison between the contour plots before and after ensemble averaging clearly demonstrates the effectiveness of ensemble averaging in removing thermal fluctuations caused by a finite temperature. Before ensemble averaging, the stress gradients are totally covered by noise even with some spatial averaging inherent in Hardy's expression. This noise is mostly removed after averaging, as shown in the clear contour plots (Figs. 5.18-5.21), The averaged stress fields at 300 K resemble those at 0 K at the same strain level (Figs. 5.3, 5.4, 5.8 and 5.9). It is noticeable that at the shear strain level of 6%, the crystal at an initial 300 K does not generate dislocations at the crack tips as it does at 0 K, which can also be observed from the atomistic simulation snapshots. This might be caused by the higher mobility of atoms at elevated temperature so the material can deform in the elastic regime under

higher strain level. It is necessary to take special care if the many-realizations correspond to the same macroscopic ensemble so that the basic assumption of ensemble averaging is not violated. As mentioned before, the crack is able to propagate from either end of the central pre-crack. The slip band behavior at opposite crack tips is completely uncorrelated. With two available equivalent slip systems at each crack tip for the crack front orientation, either one or two slip bands per tip can form. Whether the slip band emission in single-band or fork-shape geometry is partially determined by the pre-crack tip shape and is partially a matter of chance.

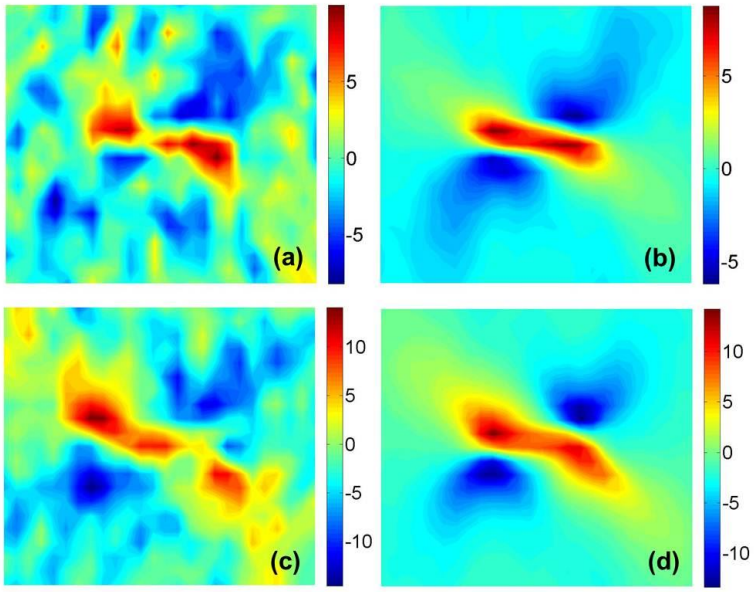

Figure 5.20 σ_{xx} for the center-cracked Fe crystal shear strained to 3% (a) before and (b) after ensemble averaging, and to 6% (c) before and (d) after ensemble averaging at around 300 K (stress has the unit of GPa)

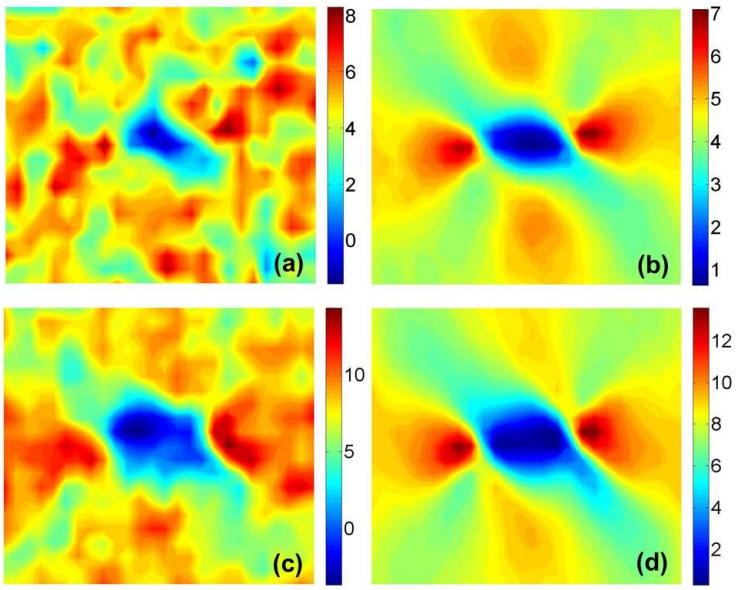

Figure 5.21 σ_{xy} for the center-cracked Fe crystal shear strained to 3% (a) before and (b) after ensemble averaging, and to 6% (c) before and (d) after ensemble averaging at around 300 K (stress has the unit of GPa)

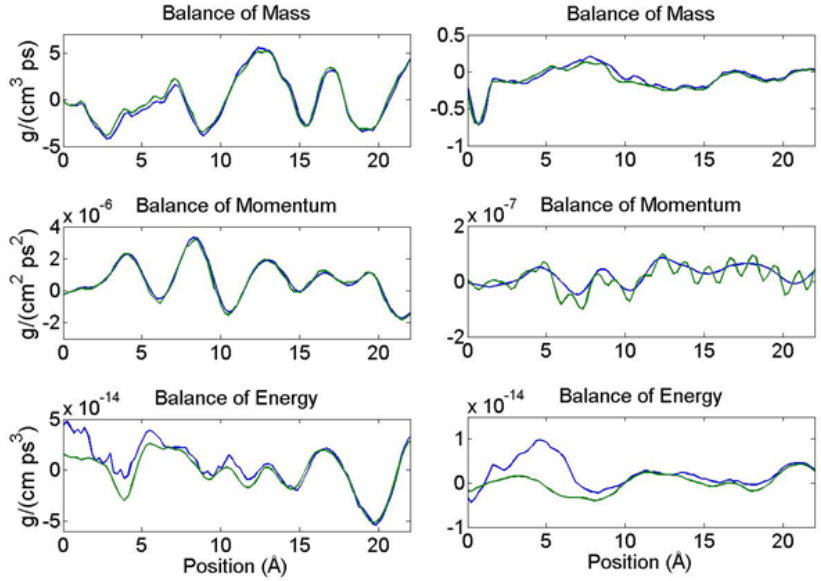

Figure 5.22 Comparison between two sides of the conservation equations before (left column) and after (right column) ensemble averaging in the diagonal directions for the Fe crystal tensile strained to 6% at around 300 K

In our simulation setup and boundary conditions, it is apparent that the pre-crack tip shape tends to generate a single slip band at both crack tips as seen from the contour plot after ensemble averaging (Fig. 5.2). For other simulation setups, ensemble averaging cannot be guaranteed to be a proper approach to remove noise. For example, some realizations may have fork-shape geometry at a single crack tip, some have fork-shape geometry at both crack tips, and some have a single-band at both crack tips. Similar scenarios can happen to dislocation emission or twin formation at crack tips, which ultimately affect the crack propagation process. In these situations, ensemble averaging may lead to erroneous results as those realizations do not correspond to the same macroscopic ensemble. For the processes that are dominated by deterministic boundary conditions rather than random thermal fluctuation factors, ensemble averaging should be a good option, such as rapid tensile and shear loading on the center-cracked body in our studies.

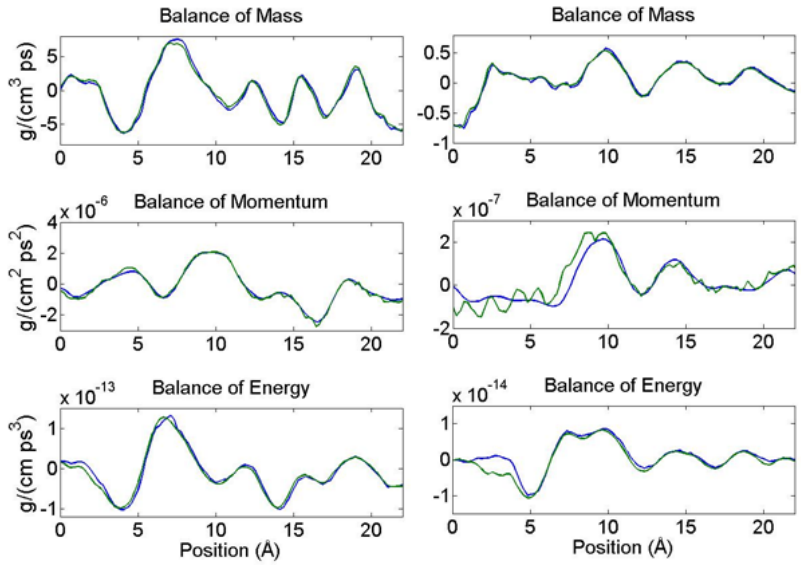

Figure 5.23 Comparison between two sides of the conservation equations before (left column) and after (right column) ensemble averaging in the diagonal directions for the Fe crystal shear strained to 6% at around 300 K

Validation of Hardy's theory at finite temperature is performed by comparing the two sides of conservation equations using thermomechanical quantities computed from a randomly chosen realization and ensemble averaged quantities. Figures 5.22 and 5.23 demonstrate the conservation equations for the Fe crystal at a strain of 6% under tensile and shear loading. At this strain level, slip bands and dislocations already generate around the crack tip region. For individual realizations, the fit between two sides of the balance laws is still pretty good, except for the balance of energy around the crack as in the 0 K case. Ensemble averaged quantities obey well the balance of the mass equation. But the RHS of balance of momentum has many bumps, which show that ensemble averaged quantities are not as good as for individual realization. This may be caused by numerical error since averaged quantities are a magnitude smaller than those before ensemble averaging. The less significant errors for individual realization may become magnified after averaging, which cause the non-smoothness of the RHS of the balance of momentum. A balance of energy still shows more discrepancy between the two sides of the equation around the crack region, for both the individual realization and ensemble averaged case.

5.5 CONCLUSIONS

In this Chapter, validity of Hardy's theory is tested for cracked solids under tensile and shear loading at an initial 0 K and 300 K. The ensemble averaging approach is used to construct the stress fields at 300 K to remove thermal noise. The following conclusions can be drawn:

1. Stress contour plots constructed around the crack under tensile and shear loading at around 0 K demonstrate that stress initially concentrates at the crack tips. The original high stress level at the tips can be relieved through slip band and dislocation emission,

accompanied by the shift of the stress concentration areas to where slip bands and dislocations locate.

2. Validity of the conservation equations using Hardy's quantities can be established at the crack tip where slip bands and other defects exist, but discrepancy between two sides of the balance of energy can be observed at the crack region. The reason is not clear at the present stage.

3. Ensemble averaging can effectively remove the thermal fluctuation and obtain stress fields with high spatial resolution. And the ensemble averaged quantities can still generally obey the conservation equations. While ensemble averaging is a good option for deterministic processes at finite temperature, care needs to be taken when probabilistic processes are investigated.

6.0 CONCLUSIONS

The main objective of this dissertation is to build a high fidelity atomistic-to-continuum link for highly non-equilibrium processes, that is, to accurately compute continuum thermomechanical quantities such as stress, heat flux and temperature from atomic velocities, positions and forces. To achieve this objective, Hardy's thermomechanical theory has been rigorously tested by numerical means and modifications have been proposed to improve the fidelity of the theory. In Chapter 3, ensemble averaging and time averaging have been compared for computing the thermomechanical fields based on Hardy's theory in terms of accuracy, convergence, and efficiency. For this purpose, MD simulations have been performed in fcc metals under thermal equilibrium and non-equilibrium, where the latter was induced by a shock impact to the solid. In Chapter 4, the validity of Hardy's theory for highly non-equilibrium processes, with and without ensemble averaging, has been tested by comparing two sides of the conservation equations based on the computed thermomechanical quantities. For this purpose, wave propagations in fcc metals at zero and finite temperatures have been simulated. A modification to the normalization criterion of the localization function has been proposed to improve the accuracy of Hardy's theory. In Chapter 5, the validity of Hardy's formulas, with and without ensemble averaging, has also been tested for an iron crystal with an embedded crack at zero and finite temperatures. In addition, the constructed stress fields have been corroborated qualitatively with the expected

mechanical response due to the different observed deformation mechanisms. The main contributions of these research works are summarized next.

6.1 MAIN CONTRIBUTIONS

The main contributions of this dissertation include the following:

- Comparison between convergence of ensemble averaging and conventional time averaging on a Ni crystal at equilibrium has shown that time averaging requires selection of a time interval larger than the critical time interval to obtain convergence under equilibrium conditions, where the critical time interval can be estimated using the elastic properties of the material. The reason for this is because of the significant correlations among the computed thermomechanical quantities at different time instants employed in computing their time average. On the other hand, the computed thermomechanical quantities from different realizations in ensemble averaging are statistically independent, and thus convergence is always guaranteed. The computed stress, heat flux, and temperature show noticeable difference in their convergence behavior while their confidence intervals increase with temperature.
- Contrary to equilibrium settings, time averaging is not equivalent to ensemble averaging in the case of shock wave propagation. Time averaging was shown to have poor performance in computing various thermomechanical fields by either oversmoothing the fields or failing to remove noises.
- Thermomechanical fields constructed for a shock impact and crack propagation problem by ensemble averaging has shown its superior performance in high accuracy and

resolution for highly non-equilibrium processes, which is unachievable through conventional time averaging approach. To implement ensemble averaging, it is necessary to have all the realizations correspond to the same macroscopic process.

- Hardy's thermomechanical quantities computed from the atomistic quantities have been shown to obey continuum conservation equations through a series of non-equilibrium simulations including Gaussian pulse and shock impact propagation in 1D Au chains, 3D Au and 3D Ni crystals. The validity of these quantities have been established through these examples regardless of characteristic volume size, atomic potential form and crystal structure.
- The normalization rule for the localization function has been modified to make Hardy's quantities obey balance laws, and for the balance of energy in particular. This new normalization rule can be viewed as the discrete version of the original normalization rule given by Hardy and has been used throughout our calculations.
- At finite temperature, conservation equations are obeyed by Hardy's thermomechanical quantities even when they deviate from the expectation values without ensemble averaging. Ensemble averaged quantities can also conserve mass, momentum and energy well.
- In crack propagation systems, where slip bands and other permanent deformation is involved, Hardy's formulas do not obey the balance of energy, but still conserve mass and momentum. The reason is not clear at the present stage.

6.2 FUTURE WORK

6.2.1 Establish theoretical explanation for the new normalization rule

In Chapter 4, a new normalization rule, $\sum_{\alpha}^{N}\psi(\mathbf{x}_{\alpha}-\mathbf{x})=N/V$ or $\sum_{\alpha}^{N}\psi(\mathbf{x}_{\alpha}-\mathbf{x})\Delta V=1$, ($N$ is the number of atoms within the characteristic volume, V is the characteristic volume, ΔV is the volume per atom in the characteristic volume) is proposed and justified through numerical testing. This new rule can be viewed as the discrete version of the original normalization criterion of $\int\psi(\mathbf{x}_{\alpha}-\mathbf{x})\mathrm{d}\mathbf{x}=1$, which is for conserved properties such as mass, momentum and energy at the continuum as well as atomistic scales for the entire system. Rigorous derivations for the new normalization rule will need to be investigated in future work. Also it has been found that the new normalization rules only make obvious the influence on the energy conservation law but little on the momentum conservation law. It may be possible that there exists some internal cancellations in the evaluation of the mass and momentum conservation equations. To answer this question, the effects of the normalization on each term in the conservation laws will need to be examined.

6.2.2 Study the invalidity of balance of energy at the crack region

In Chapter 5, the validity of Hardy's expressions is tested around the pre-crack under tensile loading and shearing loading. Balance of mass and momentum has been observed to be valid but large discrepancies between two sides of the balance of energy appeared around the crack region under both tensile and shear loading conditions. Since shear loading does not lead to crack propagation, such behavior should not be ascribed to the atom configuration around the crack

cleavage. It is also interesting that the balance of momentum is valid while balance of energy fails in this region, which is worth further investigation.

6.2.3 Study Hardy's heat flux and temperature definitions

In Chapter 4, various size of the characteristic volume can result in significant change in heat flux profile (Fig. 4.5) while the stress profile remains unchanged. Also Hardy's expressions can lead to nonzero heat flux when energy is not supposed to transport in the form of heat. The reason should be ascribed to the changing material velocity, **v**, computed with a different characteristic volume when a significant velocity gradient exists. Increasing characteristic volume results in an over-averaged material velocity at the spatial point rather than the true material velocity, which should be computed only from the adjacent atoms. A similar problem also exists for Hardy's temperature expression because material velocity, **v**, plays a significant role in the computed heat flux and temperature but not in stress and energy. A possible way to alleviate this problem is to choose a small characteristic volume that only contains atoms very close to the spatial point of interest. But this still cannot completely correct the erroneous heat flux and temperature. Therefore, more research needs to be conducted to tackle this issue.

Hardy's temperature definition is given by considering the equipartition theorem and the kinetic energy associated with atomic velocities relative to the velocity of the continuum at a spatial point, instead of rigorously derived like the stress and heat flux. This definition enables us to compute temperature at a spatial point conveniently. However, it is doubtful that this temperature definition is physically meaningful for highly non-equilibrium systems where the definition of temperature is controversial [106-120]. A study of the Hardy's temperature

definition will need to be carried out by considering existing definitions on temperature for highly non-equilibrium systems.

6.2.4 Develop constitutive laws in Hardy's framework

Hardy's stress and heat flux expressions have been developed by defining continuum quantities (mass, momentum and energy) from atomic quantities through the localization function. The essence is to give different weights to atoms that contribute to the quantities computed at the spatial point of interest. Similarly, strain can also be defined by atomic displacement and localization function. Constitutive laws that describe stress-strain relationship at the atomistic scale can be studied through numerical simulations from deformation in the elastic regime to more complex plastic deformation at different strain rates.

A constitutive equation for heat conduction at the atomistic scale can be studied provided that the correct definition for heat flux and temperature can be established first. The Fourier law of heat conduction, which has been widely and successfully used in conventional problems, cannot be used to predict heat conduction in nano/atomistic scale and ultrafast processes [121-125]. The Cattaneo equation [126, 127] was proposed to extend the validity of the Fourier law but its physical ground is still questionable. Significant endeavors have been focused on deriving a nanoscale heat conduction equation from Boltzmann transport equation (BTE) [128-133]. Since the BTE is difficult to solve theoretically [134-136], the heat conduction equation can only be derived through certain approximations. If heat flux and temperature can be computed directly from atomistic modeling of heat transport process, the existing theories in this area can be better evaluated and new theories can possibly be conceived.

6.2.5 Extend Hardy's theory to include many-body potentials

At the present stage, Hardy's theory is restricted to systems modeled by pair potentials and EAM potentials due to the limitations on the atomic force and potential energy (see Chapter 2.4). It is not possible to compute validated thermomechanical fields with high fidelity from many-body potentials such as Tersoff, Able-Tersoff-Brenner or Stillinger-Weber potentials. For example, if one wants to model heat transport processes in semiconductors such as silicon which is commonly described by the Stillinger-Weber potential and compute the heat flux and temperatures accurately, it is necessary to extend Hardy's theory to include many-body potentials. This topic has been partly partially investigated by Y. Chen [67] but still requires more investigations.

BIBLIOGRAPHY

[1] D. Frenkel, B. Smit, Understanding Molecular Simulation, in: Computational Science Series, Academic, New York, 2001.

[2] J.M. Haile, Molecular Dynamics Simulation Elementary Methods, Wiley, New York, 1992.

[3] D.C. Rapaport, The Art of Molecular Dynamics Simulation, Cambridge University Press, London, 2004.

[4] E.B. Zaretsky, X-ray diffraction evidence for the role of stacking faults in plastic deformation of solids under shock loading, Shock Waves 2 (1992) 113-116.

[5] J. Weertman, Plastic deformation behind strong shock waves, Mechanics of Materials 5 (1986) 13-28.

[6] B.L. Holian, P.S. Lomdahl, Plasticity Induced by Shock Waves in Nonequilibrium Molecular-Dynamics Simulations, Science 280 (1998) 2085-2088.

[7] D.L. Tonks, R.S. Hixson, J.N. Johnson, G.T. Gray, III, Dislocation-drag contribution to high-rate plastic deformation in shock-loaded tantalum, in: High-Pressure Science and Technology - 1993. Joint International Association for Research and Advancement of High Pressure Science and Technology and American Physical Society Topical Group on Shock Compression of Condensed Matter Conference, 1994, pp. 997-1000.

[8] C. Hongqiang, J.W. Kysar, Y.L. Yao, Characterization of plastic deformation induced by microscale laser shock peening, Transactions of the ASME. Journal of Applied Mechanics 71 (2004) 713-723.

[9] X. Xinmei, L. Yulong, S. Tao, H. Bing, Shock Enhancement of Aluminum Foam under Impact Loading Using FEM Simulations, Advanced Materials Research 160-162 (2011) 1077-1082.

[10] H. Hongliang, T. Sekine, T. Kobayashi, K. Kimoto, Phase transformation of germanium nitride (Ge3N4) under shock wave compression, Journal of Applied Physics 90 (2001) 4403-4406.

[11] M.R. Manaa, Shear-induced metallization of triamino-trinitrobenzene crystals, Applied Physics Letters 83 (2003) 1352-1354.

[12] E. Cerreta, G.T. Gray, A.C. Lawson, T.A. Mason, C.E. Morris, The influence of oxygen content on the to phase transformation and shock hardening of titanium, Journal of Applied Physics 100 (2006) 13530.

[13] L. Jun, Z. Xianming, Z. Wenjun, L. Jiabo, J. Fuqian, A shock-induced phase transformation in a LiTaO3 crystal, Journal of Applied Physics 102 (2007) 083503.

[14] J. Sharma, R.W. Armstrong, W.L. Elban, C.S. Coffey, H.W. Sandusky, Nanofractography of shocked RDX explosive crystals with atomic force microscopy, Applied Physics Letters 78 (2001) 457-459.

[15] A. Strachan, A.C.T. van Duin, D. Chakraborty, S. Dasgupta, W.A. Goddard, III, Shock Waves in High-Energy Materials: The Initial Chemical Events in Nitramine RDX, Physical Review Letters 91 (2003) 098301.

[16] S.V. Zybin, P. Xu, Q. An, W.A. Goddard, ReaxFF reactive molecular dynamics: Coupling mechanical impact to chemical initiation in energetic materials, in: 2010 DoD High Performance Computing Modernization Program Users Group Conference, Schaumburg, IL, 2010, pp. 273-278.

[17] A. Tokmakoff, M.D. Fayer, D.D. Dlott, Chemical reaction initiation and hot-spot formation in shocked energetic molecular materials, The Journal of Physical Chemistry 97 (1993) 1901-1913.

[18] K.-i. Nomura, R.K. Kalia, A. Nakano, P. Vashishta, A.C.T. van Duin, W.A. Goddard, III, Dynamic Transition in the Structure of an Energetic Crystal during Chemical Reactions at Shock Front Prior to Detonation, Physical Review Letters 99 (2007) 148303.

[19] J.B. Gibson, A.N. Goland, M. Milgram, G.H. Vineyard, Dynamics of Radiation Damage, Physical Review 120 (1960) 1229-1253.

[20] A.I. Kitaigorodskii, Molecular Crystals and Molecules, Academic Press, New York, 1973.

[21] S. Califano, V. Schettino, N. Neto, Lattice Dynamics of Molecular Crystals, Springer-Verlag, Berlin, 1981.

[22] A.J. Pertsin, A.I. Kitaigorodsky, The Atom-Atom Potential Method: Applications to Organic Molecular Solids Springer-Verlag, Berlin, 1987.

[23] J. Kohler, R. Meyer, Explosives, 4th Edition ed., VCH Publishers, New York, 1993.

[24] C.S. Coffey, E.T. Toton, A microscopic theory of compressive wave-induced reactions in solid explosives, The Journal of Chemical Physics 76 (1982) 949-954.

[25] S.F. Trevino, D.H. Tsai, Molecular dynamical studies of the dissociation of a diatomic molecular crystal. II. Equilibrium kinetics, The Journal of Chemical Physics 81 (1984) 248-256.

[26] D.D. Dlott, M.D. Fayer, Shocked molecular solids: Vibrational up pumping, defect hot spot formation, and the onset of chemistry, The Journal of Chemical Physics 92 (1990) 3798-3812.

[27] F.J. Zerilli, E.T. Toton, Shock-induced molecular excitation in solids, Physical Review B 29 (1984) 5891-5902.

[28] F.E. Walker, Physical kinetics, Journal of Applied Physics 63 (1988) 5548-5554.

[29] W. Tai-Guang, R.E. Wyatt, Semiclassical dynamics of shock wave propagation in molecular crystals: application to the Morse lattice, Journal of Physics: Condensed Matter 2 (1990) 9787.

[30] R. Menikoff, Hot spot formation from shock reflections, Shock Waves 21 (2011) 141-148.

[31] F.P. Bowden, A.D. Yoffe, Initiation and Growth of Explosion in Liquids and Solids, Cambridge University Press, Cambridge, 1952.

[32] C.M. Tarver, S.K. Chidester, A.L. Nichols, Critical Conditions for Impact- and Shock-Induced Hot Spots in Solid Explosives†, The Journal of Physical Chemistry 100 (1996) 5794-5799.

[33] A. Qi, S.V. Zybin, W.A. Goddard, III, A. Jaramillo-Botero, M. Blanco, L. Sheng-Nian, Elucidation of the dynamics for hot-spot initiation at nonuniform interfaces of highly shocked materials, Physical Review B (Condensed Matter and Materials Physics) 84 (2011) 220101 (220105 pp.).

[34] G. Yuan, L. Cheng, T. Anh Kiet, Z. Hongtao, Molecular dynamics simulation of crack propagation on different slip planes of BCC iron, in: 2008 International Conference on Nanoscience and Nanotechnology, IEEE, Piscataway, NJ, 2008, pp. 226-229.

[35] V.A. Borodin, P.V. Vladimirov, Molecular dynamics simulations of quasi-brittle crack development in iron, Journal of Nuclear Materials 415 (2011) 320-328.

[36] G. Yuan, L. Cheng, G. Michal, T. Anh Kiet, A study of crack propagation in BCC iron by molecular dynamics method, Key Engineering Materials 385-387 (2008) 453-456.

[37] N. Yanagida, O. Watanabe, Molecular dynamics simulation of effects of lattice orientation on crack propagation in alpha-iron when the primary slip direction is in the plane of tensile stress, JSME International Journal, Series A (Mechanics and Material Engineering) 39 (1996) 321-329.

[38] S. Nishijima, A. Nakahira, T. Okada, K. Niihara, S. Namba, Molecular dynamics simulation of crack propagation in a -iron at cryogenic temperatures, in: Advances in Cryogenic Engineering. Materials Pleunum Press, New York, NY, 1997, pp. 515-520.

[39] A. Latapie, D. Farkas, Molecular dynamics simulations of stress-induced phase transformations and grain nucleation at crack tips in Fe, Modelling and Simulation in Materials Science and Engineering 11 (2003) 745-753.

[40] H.X. Xie, C.Y. Wang, T. Yu, Molecular Dynamics Simulation of Brittle Fracture in Bcc Iron Defect and Diffusion Forum 272 (2008) 41-50.

[41] F. Cleri, S. Yip, D. Wolf, S.R. Phillpot, Atomic-Scale Mechanism of Crack-Tip Plasticity: Dislocation Nucleation and Crack-Tip Shielding, Physical Review Letters 79 (1997) 1309-1312.

[42] H.B. Dhia, G. Rateau, The Arlequin method as a flexible engineering design tool, International Journal for Numerical Methods in Engineering 62 (2005) 1442-1462.

[43] S. Prudhomme, H. Ben Dhia, P.T. Bauman, N. Elkhodja, J.T. Oden, Computational analysis of modeling error for the coupling of particle and continuum models by the Arlequin method, Computer Methods in Applied Mechanics and Engineering 197 (2008) 3399-3409.

[44] S.P. Xiao, T. Belytschko, A bridging domain method for coupling continua with molecular dynamics, Computer Methods in Applied Mechanics and Engineering 193 (2004) 1645-1669.

[45] J. Fish, W. Chen, Discrete-to-continuum bridging based on multigrid principles, Computer Methods in Applied Mechanics and Engineering 193 (2004) 1693-1711.

[46] C. Farhat, I. Harari, U. Hetmaniuk, The discontinuous enrichment method for multiscale analysis, Computer Methods in Applied Mechanics and Engineering 192 (2003) 3195-3209.

[47] S. Zhang, R. Khare, Q. Lu, T. Belytschko, A bridging domain and strain computation method for coupled atomistic–continuum modelling of solids, International Journal for Numerical Methods in Engineering 70 (2007) 913-933.

[48] P.A. Guidault, T. Belytschko, On the L2 and the H1 couplings for an overlapping domain decomposition method using Lagrange multipliers, International Journal for Numerical Methods in Engineering 70 (2007) 322-350.

[49] M. Xu, T. Belytschko, Conservation properties of the bridging domain method for coupled molecular/continuum dynamics, International Journal for Numerical Methods in Engineering 76 (2008) 278-294.

[50] P.A. Guidault, T. Belytschko, Bridging domain methods for coupled atomistic–continuum models with L2 or H1 couplings, International Journal for Numerical Methods in Engineering 77 (2009) 1566-1592.

[51] D.E. Farrell, H.S. Park, W.K. Liu, Implementation aspects of the bridging scale method and application to intersonic crack propagation, International Journal for Numerical Methods in Engineering 71 (2007) 583-605.

[52] P. Aubertin, J. Réthoré, R. de Borst, Energy conservation of atomistic/continuum coupling, International Journal for Numerical Methods in Engineering 78 (2009) 1365-1386.

[53] G.J. Wagner, W.K. Liu, Coupling of atomistic and continuum simulations using a bridging scale decomposition, Journal of Computational Physics 190 (2003) 249-274.

[54] R.J.E. Clausius, On a mechanical theorem applicable to heat, Philosophical Magazine 40 (1870) 122-127.

[55] J.C. Maxwell, On reciprocal figures, frames and diagrams of forces Transactions / the Royal Society of Edinburgh XXVI (1870) 1-43.

[56] J.C. Maxwell, Van der Waals on the continuity of the gaseous and liquid states, Nature (1874) 477-480.

[57] R.W. Smith, D.J. Srolovitz, Void formation during film growth: A molecular dynamics simulation study, Journal of Applied Physics 79 (1996) 1448-1457.

[58] S.Y. Hu, Y.L. Li, K. Watanabe, Calculation of internal stresses around Cu precipitates in the bcc Fe matrix by atomic simulation, Modelling and Simulation in Materials Science and Engineering 7 (1999) 641.

[59] M.F. Horstemeyer, M.I. Baskes, Atomistic Finite Deformation Simulations: A Discussion on Length Scale Effects in Relation to Mechanical Stresses, Journal of Engineering Materials and Technology 121 (1999) 114-119.

[60] G. Marc, W.G. McMillan, The virial theorem, Advances in Chemical Physics 58 (1985) 209-361.

[61] A.K. Subramaniyan, C.T. Sun, Continuum interpretation of virial stress in molecular simulations, International Journal of Solids and Structures 45 (2008) 4340-4346.

[62] J.A. Zimmerman, E.B. WebbIII, J.J. Hoyt, R.E. Jones, P.A. Klein, D.J. Bammann, Calculation of stress in atomistic simulation, Modelling and Simulation in Materials Science and Engineering 12 (2004) S319.

[63] K.S. Cheung, S. Yip, Atomic-level stress in an inhomogeneous system, Journal of Applied Physics 70 (1991) 5688-5690.

[64] D.H. Tsai, The virial theorem and stress calculation in molecular dynamics, The Journal of Chemical Physics 70 (1979) 1375-1382.

[65] M. Zhou, A new look at the atomic level virial stress: on continuum-molecular system equivalence, Proceedings of the Royal Society of London. Series A: Mathematical, Physical and Engineering Sciences 459 (2003) 2347-2392.

[66] M. Zhou, Thermomechanical continuum representation of atomistic deformation at arbitrary size scales, Proceedings of the Royal Society A: Mathematical, Physical and Engineering Science 461 (2005) 3437-3472.

[67] Y. Chen, Local stress and heat flux in atomistic systems involving three-body forces, The Journal of Chemical Physics 124 (2006) 054113.

[68] A. Murdoch, A Critique of Atomistic Definitions of the Stress Tensor, Journal of Elasticity 88 (2007) 113-140.

[69] E.B. Webb, J.A. Zimmerman, S.C. Seel, Reconsideration of Continuum Thermomechanical Quantities in Atomic Scale Simulations, Mathematics and Mechanics of Solids 13 (2008) 221-266.

[70] M. Zhou, D.L. McDowell, Equivalent continuum for dynamically deforming atomistic particle systems, Philosophical Magazine A 82 (2002) 2547-2574.

[71] J.F. Lutsko, Stress and elastic constants in anisotropic solids: Molecular dynamics techniques, Journal of Applied Physics 64 (1988) 1152-1154.

[72] M. Anna, Stress calculations on the atomistic level, Modelling and Simulation in Materials Science and Engineering 9 (2001) 327.

[73] J. Cormier, J.M. Rickman, T.J. Delph, Stress calculation in atomistic simulations of perfect and imperfect solids, Journal of Applied Physics 89 (2001) 99-104.

[74] Z.H. Sun, X.X. Wang, A.K. Soh, H.A. Wu, On stress calculations in atomistic simulations, Modelling and Simulation in Materials Science and Engineering 14 (2006) 423.

[75] J.H. Irving, J.G. Kirkwood, The Statistical Mechanical Theory of Transport Processes. IV. The Equations of Hydrodynamics, The Journal of Chemical Physics 18 (1950) 817-829.

[76] R.J. Hardy, Formulas for determining local properties in molecular-dynamics simulations: Shock waves, The Journal of Chemical Physics 76 (1982) 622-628.

[77] R.J. Hardy, S. Root, D.R. Swanson, Continuum properties from molecular simulations, in: Shock Compression of Condensed Matter - 2001: 12th APS Topical Conference American Institute of Physics, Atlanta, Georgia, 2002, pp. 363–366.

[78] S. Root, R.J. Hardy, D.R. Swanson, Continuum predictions from molecular dynamics simulations: Shock waves, The Journal of Chemical Physics 118 (2003) 3161-3165.

[79] E.B.W. III, J.A. Zimmerman, S.C. Seel, Reconsideration of Continuum Thermomechanical Quantities in Atomic Scale Simulations, Mathematics and Mechanics of Solids 13 (2008) 221-266.

[80] J.A. Zimmerman, R.E. Jones, J.A. Templeton, A material frame approach for evaluating continuum variables in atomistic simulations, Journal of Computational Physics 229 (2010) 2364-2389.

[81] A.C. To, Y. Fu, W. Kam Liu, Denoising methods for thermomechanical decomposition for quasi-equilibrium molecular dynamics simulations, Computer Methods in Applied Mechanics and Engineering 200 (2011) 1979-1992.

[82] M.P. Allen, D.J. Tildesley, Computer Simulation of Liquids, Clarendon, Oxford, 1987.

[83] K. Binder, D.W. Heermann, Monte Carlo Simulation in Statistical Physics. An Introduction (4th edition)., Springer, 2002.

[84] M.S. Daw, M.I. Baskes, Semiempirical, Quantum Mechanical Calculation of Hydrogen Embrittlement in Metals, Physical Review Letters 50 (1983) 1285-1288.

[85] M.S. Daw, M.I. Baskes, Embedded-atom method: Derivation and application to impurities, surfaces, and other defects in metals, Physical Review B 29 (1984) 6443-6453.

[86] S.M. Foiles, Calculation of the surface segregation of Ni-Cu alloys with the use of the embedded-atom method, Physical Review B 32 (1985) 7685-7693.

[87] S.M. Foiles, M.I. Baskes, M.S. Daw, Embedded-atom-method functions for the fcc metals Cu, Ag, Au, Ni, Pd, Pt, and their alloys, Physical Review B 33 (1986) 7983-7991.

[88] W.C. Swope, H.C. Andersen, P.H. Berens, K.R. Wilson, A computer simulation method for the calculation of equilibrium constants for the formation of physical clusters of molecules: Application to small water clusters, The Journal of Chemical Physics 76 (1982) 637-649.

[89] K. Huang, Statistical Mechanics, John Wiley & Sons, New York, 1987.

[90] F.H. Stillinger, T.A. Weber, Computer simulation of local order in condensed phases of silicon, Physical Review B 31 (1985) 5262-5271.

[91] Y. Fu, M. Kirca, A.C. To, On determining the thermal state of individual atoms in molecular dynamics simulations of nonequilibrium processes in solids, Chemical Physics Letters 506 (2011) 290-297.

[92] Y. Fu, A.C. To, On the evaluation of Hardy's thermomechanical quantities using ensemble and time averaging, Modelling and Simulation in Materials Science and Engineering 21 (2013) 055015 @ IOP Publishing. Reproduced with permission of IOP Publishing. All rights reserved.

[93] M.S. Daw, S.M. Foiles, M.I. Baskes, The embedded-atom method: a review of theory and applications, Materials Science Reports 9 (1993) 251-310.

[94] L.E. Malvern, Introduction to the Mechanics of a Continuous Medium, Prentice-Hall, Inc., Englewood Cliffs, New Jersey, 1969.

[95] M.E. Gurtin, An Introduction to Continuum Mechanics, Academic Press, Inc., San Diego, California, 1981.

[96] R.C. Lincoln, K.M. Koliwad, P.B. Ghate, Morse-Potential evaluation of second- and third-order elastic constants of some cubic metals, The Physical Review 157 (1967) 463-466.

[97] É.V. Kozlov, L.E. Popov, M.D. Starostenkov, Calculation of the morse potential for solid gold, Soviet Physics Journal 15 (1972) 395-396.

[98] Reprinted with permission from Y. Fu, A.C. To, A modification to Hardy's thermomechanical theory that conserves fundamental properties more accurately, Journal of Applied Physics 113 (2013) 233505. Copyright 2013, AIP publishing LLC.

[99] A. Machová, G.J. Ackland, Dynamic overshoot in alpha-iron by atomistic simulations, Modelling and Simulation in Materials Science and Engineering 6 (1998) 521.

[100] J. Červ, M. Landa, A. Machová, Transonic twinning from the crack tip, Scripta Materialia 43 (2000) 423-428.

[101] A. Machová, G.E. Beltz, Ductile–brittle behavior of (001)[110] nano-cracks in bcc iron, Materials Science and Engineering: A 387–389 (2004) 414-418.

[102] Y.-F. Guo, D.-L. Zhao, Atomistic simulation of structure evolution at a crack tip in bcc-iron, Materials Science and Engineering: A 448 (2007) 281-286.

[103] A. Spielmannová, A. Machová, P. Hora, Transonic twins in 3D bcc iron crystal, Computational Materials Science 48 (2010) 296-302.

[104] T. Belytschko, T. Black, Elastic crack growth in finite elements with minimal remeshing, International Journal for Numerical Methods in Engineering 45 (1999) 601-620.

[105] S. Jay, L. Jim, W. Haim, L. Phillip, B. Ted, N. Sukumar, L. Yu, X-FEM Toolkit for Automated Crack Onset and Growth Prediction, in: 49th AIAA/ASME/ASCE/AHS/ASC Structures, Structural Dynamics, and Materials Conference, American Institute of Aeronautics and Astronautics, 2008.

[106] A. Baranyai, Temperature of nonequilibrium steady-state systems, Physical Review E 62 (2000) 5989-5997.

[107] A. Barletta, E. Zanchini, Nonequilibrium temperature and hyperbolic heat conduction, Physical Review B 57 (1998) 14228-14234.

[108] J. Casas-Vazquez, D. Jou, Nonequilibrium temperature versus local-equilibrium temperature, Physical Review E 49 (1994) 1040-1048.

[109] J. Fort, D. Jou, J.E. Llebot, Temperature and measurement: comparison between two models of nonequilibrium radiation, Physica A 269 (1999) 439-454.

[110] T. Hatano, D. Jou, Measuring nonequilibrium temperature of forced oscillators, Physical Review E 67 (2003) 26121.

[111] W.G. Hoover, C.G. Hoover, Nonequilibrium temperature and thermometry in heat-conducting 4 models, Physical Review E 77 (2008) 041104.

[112] H.L. Hortensius, A. Ozturk, P. Zeng, E.F.C. Driessen, T.M. Klapwijk, Microwave-induced nonequilibrium temperature in a suspended carbon nanotube, Applied Physics Letters 100 (2012) 223112.

[113] D. Jou, J. Casas-Vazquez, Carnot cycles and a non-equilibrium absolute temperature, Journal of Physics A: Mathematical and General 20 (1987) 5371.

[114] D. Jou, J. Casas-Vazquez, Nonequilibrium absolute temperature, thermal waves and phonon hydrodynamics, Physica A: Statistical Mechanics and its Applications 163 (1990) 47-58.

[115] D. Jou, C. Perez-Garcia, J. Casas-Vazquez, On a non-equilibrium partition function for heat conduction, Journal of Physics A: Mathematical and General 17 (1984) 2799.

[116] J. Keizer, Fluctuations, stability, and generalized state functions at nonequilibrium steady states, The Journal of Chemical Physics 65 (1976) 4431-4444.

[117] J. Keizer, Thermodynamics at nonequilibrium steady states, The Journal of Chemical Physics 69 (1978) 2609-2620.

[118] J. Keizer, Heat, work, and the thermodynamic temperature at nonequilibrium steady states, The Journal of Chemical Physics 82 (1985) 2751-2771.

[119] D.P. Sheehan, J.T. Garamella, D.J. Mallin, W.F. Sheehan, Steady-state nonequilibrium temperature gradients in hydrogen gas-metal systems: Challenging the second law of thermodynamics, Physica Scripta T151 (2012) 014030.

[120] D. Jou, M. Criado-Sancho, J. Casas-Vazquez, Nonequilibrium temperature and fluctuation-dissipation temperature in flowing gases, Physica A 358 (2005) 49-57.

[121] D.D. Joseph, L. Preziosi, Heat waves, Reviews of Modern Physics 61 (1989) 41-73.

[122] D.Y. Tzou, Macro- to Microscale Heat Transfer: The Lagging Behavior, Taylor and Francis, London, 1997.

[123] G. Chen, Ballistic-Diffusive Heat-Conduction Equations, Physical Review Letters 86 (2001) 2297-2300.

[124] G. Chen, Ballistic-Diffusive Equations for Transient Heat Conduction From Nano to Macroscales, Journal of Heat Transfer 124 (2002) 320-328.

[125] D.G. Cahill, W.K. Ford, K.E. Goodson, G.D. Mahan, A. Majumdar, H.J. Maris, R. Merlin, S.R. Phillpot, Nanoscale thermal transport, Journal of Applied Physics 93 (2003) 793-818.

[126] T. Bright, Z. Zhang, Common Misperceptions of the Hyperbolic Heat Equation, Journal of Thermophysics and Heat Transfer 23 (2009) 601-607.

[127] D.D. Joseph, L. Preziosi, Addendum to the paper "Heat waves" [Rev. Mod. Phys. 61, 41 (1989)], Reviews of Modern Physics 62 (1990) 375-391.

[128] G.D. Mahan, F. Claro, Nonlocal theory of thermal conductivity, Physical Review B 38 (1988) 1963-1969.

[129] A.A. Joshi, A. Majumdar, Transient ballistic and diffusive phonon heat transport in thin films, Journal of Applied Physics 74 (1993) 31-39.

[130] J. Callaway, Model for Lattice Thermal Conductivity at Low Temperatures, Physical Review 113 (1959) 1046-1051.

[131] J. Ordonez-Miranda, R. Yang, J.J. Alvarado-Gil, A constitutive equation for nano-to-macro-scale heat conduction based on the Boltzmann transport equation, Journal of Applied Physics 109 (2011) 084319.

[132] X. Mingtian, L. Xuefang, The modeling of nanoscale heat conduction by Boltzmann transport equation, International Journal of Heat and Mass Transfer 55 (2012) 1905-1910.

[133] S.V.J. Narumanchi, J.Y. Murthy, C.H. Amon, Boltzmann transport equation-based thermal modeling approaches for hotspots in microelectronics, Heat and Mass Transfer 42 (2006) 478-491.

[134] M.M. Dignam, A.A. Grinberg, Solution of the Boltzmann transport equation in an arbitrary one-dimensional-potential profile, Physical Review B 50 (1994) 4345-4354.

[135] H.C. Law, K.C. Kao, New Approach to the Solution of the Time-Dependent Boltzmann Transport Equation, Physical Review Letters 29 (1972) 625-628.

[136] J.M. Blatt, A.H. Opie, Nonequilibrium statistical mechanics I. The Boltzmann transport equation, Journal of Physics A: Mathematical and General 8 (1975) 142.